

Indium-impurity pairs in semiconductors  
and the study of the influence of uniaxial  
stress on defect complexes in silicon

Dissertation  
zur  
Erlangung des Doktorgrades (Dr. rer. nat.)  
der  
Mathematisch – Naturwissenschaftlichen Fakultät  
der  
Rheinischen Friedrich – Wilhelms – Universität Bonn

vorgelegt von

Genene Tessema Mola

aus

Arsi, Äthiopien

Bonn 2003

Angefertigt mit Genehmigung  
der Mathematisch - Naturwissenschaftlichen Fakultät  
der Rheinischen Friedrich - Wilhelms - Universität Bonn

Referent: Priv. Doz. Dr. Reiner Vianden

Korreferent: Prof. Dr. Manfred Forker

Tag der Promotion: 06.02.2003

This work is dedicated to my parents

Tessema Mola and Alemaz W/Tensay

# Contents

<b>Introduction</b>	<b>4</b>
<b>Chapter 1</b>	<b>6</b>
<b>1 PROPERTIES of Si and Ge</b>	<b>6</b>
1.1 Production of crystalline silicon and germanium . . . . .	6
1.2 Electrical properties . . . . .	9
<b>Chapter 2</b>	<b>11</b>
<b>2 HYPERFINE INTERACTION and ANGULAR CORRELATION</b>	<b>11</b>
2.1 Hyperfine interaction . . . . .	11
2.1.1 Classical electrostatic hyperfine interaction . . . . .	11
2.1.2 Quantum mechanical treatment of the electrostatic hyperfine interaction . . . . .	13
2.2 Theory of angular correlation . . . . .	17
2.2.1 Introduction . . . . .	17
2.2.2 Directional angular correlation function . . . . .	18
2.2.3 Extranuclear perturbation . . . . .	20
2.3 Perturbation by static interaction . . . . .	23
2.3.1 Perturbation factor for static electric quadrupole interaction	25
<b>Chapter 3</b>	<b>29</b>
<b>3 EXPERIMENTAL METHOD</b>	<b>29</b>
3.1 Perturbed angular correlation (PAC) . . . . .	29
3.1.1 Experimental set up . . . . .	29
3.1.2 Probe nucleus $^{111}\text{In}$ . . . . .	31
3.1.3 The ratio function $[R(t)]$ . . . . .	32
3.2 Solid angle correction for anisotropy coefficient . . . . .	39
3.3 Ion implantation . . . . .	41
3.3.1 The ion implanter . . . . .	41
3.3.2 Recovery of damage after $^{111}\text{In}$ implantation . . . . .	45
3.3.2.1 Silicon . . . . .	46
3.3.2.2 Germanium . . . . .	47

<i>Contents</i>	2
<b>Chapter 4</b>	<b>49</b>
<b>4 INDIUM IMPURITY PAIRS in Si and Ge.</b>	<b>49</b>
4.1 Introduction . . . . .	49
4.2 Formation and thermal stability of Indium-Donor pairs in silicon . .	50
4.3 Indium-group V donor pairs . . . . .	50
4.3.1 In-P pair . . . . .	50
4.3.2 Reversibility test of In-P pair at high temperature . . . . .	53
4.3.3 In-As pairs . . . . .	54
4.3.4 Discussion . . . . .	56
4.4 Indium-group VI donor pair . . . . .	58
4.4.1 In-Te pair . . . . .	58
4.4.2 Results . . . . .	58
4.4.3 Discussion of the results . . . . .	63
4.4.4 Temperature dependence of the EFG at the In-Te pair . . .	66
4.4.5 Selenium implanted silicon . . . . .	69
4.5 Indium-Carbon pair in Germanium . . . . .	70
4.5.1 Introduction . . . . .	70
4.5.2 Formation and thermal stability of the In-C pair in Ge . . .	71
4.5.3 Discussion of the results . . . . .	73
4.5.4 Comparison with results of ion channelling and infrared ab- sorption measurements . . . . .	78
<b>Chapter 5</b>	<b>81</b>
<b>5 EFFECT OF UNIAXIAL STRESS on In-IMPURITY PAIRS in Si</b>	<b>81</b>
5.1 Introduction . . . . .	81
5.2 Method of creating uniaxial stress . . . . .	84
5.3 Intrinsic silicon under tensile stress along the $\langle 110 \rangle$ direction. . .	86
5.4 In-Sb pair under tensile stress . . . . .	87
5.5 In-As pair under compressional uniaxial stress . . . . .	90
5.6 Uniaxial compressional stress on In-Te pair . . . . .	93
5.7 Uniaxial stress on In-P pair . . . . .	96
5.8 Discussion of the results . . . . .	98
<b>Conclusions</b>	<b>104</b>
<b>Appendix</b>	<b>106</b>
<b>A In-Te pair in silicon</b>	<b>106</b>
A.1 Dissociation energy for an irreversible process . . . . .	106
A.2 Fourier transform of the interaction frequency of In-Te pair . . . . .	108
A.3 Uniaxial stress on In-Te pair in silicon. . . . .	109

<b>B In-Sb pair in silicon.</b>	<b>110</b>
B.1 Uniaxial stress on In-Sb pair at low temperature in silicon. . . . .	110
B.2 Uniaxial stress on In-Sb pair in silicon. . . . .	111
<b>C <math>s_n^{eff}</math>-Coefficients</b>	<b>112</b>
C.1 polycrystalline source . . . . .	112
C.2 $s_n^{eff}$ -Coefficients for single crystal source. . . . .	113
<b>D Inhomogeneous lattice structure</b>	<b>114</b>
<b>List of Tables</b>	<b>115</b>
<b>List of Figures</b>	<b>115</b>
<b>Bibliography</b>	<b>121</b>
<b>Acknowledgment</b>	<b>128</b>
<b>Curriculum vitae</b>	<b>129</b>

# Introduction

Had it not been for the existence of semiconductor technology, much of today's civilization would not have been possible. It has contributed tremendously to the progress in the areas of communication, information technology and computing, solar energy conversion and many other fields. In general, it has made possible rapid changes in today's life style. Silicon and germanium play a primary role in the present semiconductor technology. Especially, without silicon many of the technologies would't have become reality. Today, silicon is the building block of many transistors and computer chips etc. Germanium is used principally in fiber optics, infrared optics and in polymerization catalyts. Moreover, many other materials have been found containing elemental silicon and germanium which have an indispensable role in several areas of application. For example, silicon carbide (SiC) is an important compound semiconductor for fabrication of high temperature devices. SiGe is increasingly important in cellular handsets and wireless communication devices.

As the result of their importance for commercial purposes, silicon and germanium are thoroughly studied by industry as well as academic institutions. However, there are still open questions that need to be addressed. It is common practice today to alter the properties of semiconductors by doping them with different impurities. Ion implantation is an effective method of introducing impurities in a well defined region of the target material. Information about the properties of the impurities in the host is absolutely necessary in the design of semiconductor devices. In fact, not only the knowledge of deliberately incorporated ions but also of the residual defects is equally important to understand and control the behavior of the materials.

Different experimental methods have been employed for characterization and investigation of defects in silicon and germanium. Based on these experimental results, theories have been tested and improved. The perturbed  $\gamma - \gamma$  angular correlation (PAC) is one of the methods which makes possible the extraction of information of the defects on an atomic scale. In this method point defects are trapped using radioactive probe atoms and the resulting interaction carries information about the nature of the defect. Point defects which occur commonly in semiconductors influence the property of the material in undesired ways. For example, the existence of hydrogen in silicon is known for the deactivation of electrically active centers [PEAR87]. It is also a natural phenomena that compensation of charge carriers

will occur when oppositely charged ions simultaneously exist in a semiconductor. Therefore, the knowledge of the nature of such defects enables one to reduce their negative contribution to the property of the materials.

In the past, group-V donors have been studied in silicon and germanium using  $^{111}\text{In}$  as a PAC probe [WICH89], [FORK92]. The In-donor pairs are detected and characterized by the measured unique interaction frequencies in the host lattice. The frequencies are associated with the existence of different defect clusters at nearest neighbor distance to the probe atom. In an attempt to fully understand the local electronic structure that results in the measured electric field gradients (EFG), theoretical calculations have been made using the Korringa-Kohn-Rostoker (KKR) Green's function method [SETT99]. The result of the theoretical calculations in silicon and germanium are in good agreement with the experiments. The current work is partly carried out to make available new values of the EFG for further tests of the theory and at the same time information are collected about the incorporation of the impurities in the host lattice.

In the first chapter a brief description of the properties of silicon and germanium are given. Chapters 2 and 3 contain the theoretical background of the method used and an introduction to the ion implantation. The experimental results of the indium-group V and VI donor pairs in silicon are presented in chapter 4. In the same chapter the temperature dependence of the interaction frequency of the In-Te pair in silicon is discussed. Indium-carbon pairs in germanium have also been included in chapter 4 whose thermal equilibrium concentration of pairs and orientation measurements are discussed in detail. The study of the indium-donor pairs under the influence of uniaxial stress in silicon is presented in chapter 5.



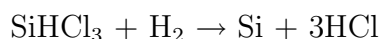
# Chapter 1

## PROPERTIES of Si and Ge

### 1.1 Production of crystalline silicon and germanium

The materials used in this work are crystalline silicon and germanium, which often serve as the basis of most electronic devices today. These semiconductors have greatly improved the daily life of mankind. Because of its abundance in nature and suitable electrical properties, silicon is predominantly used in today's applications compared to all other semiconductors. Silicon is the second most abundant element next to oxygen in the Earth's crust. According to chemical analysis of the solid matter of the Earth, it constitutes 46% Oxygen followed by Si (28%), Al(8%), Fe(6%) and all other elements at lower levels [NEWM82].

In nature, silicon and germanium are found in an impure and oxidized form. Germanium is mostly found in a compound in zinc ore, coal and other minerals, whereas, silicon exists abundantly as silicon dioxide ( $\text{SiO}_2$ ). To obtain elemental silicon, quartzite ( $\text{SiO}_2$ ) is reacted with carbon in an electric arc furnace at a temperature close to  $1800^\circ\text{C}$ . About 90% of the resulting material, termed metallurgical-grade silicon, with a purity of about 99% is used in the manufacture of steel. The remaining 10% is reacted with hydrogen chloride to form a wide spectrum of compounds which are then subjected to fractional distillation. Most of this material is used in the manufacture of silicon rubber, silicone, waxes, paint etc. The most pure fraction of trichlorosilane ( $\text{SiHCl}_3$ ) with boiling point near  $31^\circ\text{C}$  and with metallic contamination reduced to a minimum is subsequently decomposed by the a reaction with hydrogen gas at temperatures in the region of  $1200^\circ\text{C}$  to produce semiconductor-grade polycrystalline silicon.



This reaction takes place in a reactor containing a resistance - heated silicon rod, which serves as the nucleation point for the deposition of silicon. In many applications silicon is used in crystalline form. The final test of the quality of the

polycrystalline silicon can only be made once it has been converted into a single-crystal. Polycrystalline silicon is converted into single crystal ingots by either the crucible pulling Czochralski (CZ) technique or the crucible-free, floating-zone (FZ) technique. About 90% of the world's production is crucible-pulled [SZE81] and is preferred in the manufacture of integrated circuits although FZ material is more pure.

**Czochralski (CZ) technique :** This method is widely used to attain single crystal silicon for many industrial purposes. The crystallization process starts using pure polycrystalline silicon in the form of nuggets, or a one-piece crucible charge, is placed in high-purity silica ( $\text{SiO}_2$ ) crucible which in turn is placed into a graphite susceptor (see Figure 1.1). The charge is then heated to the melting point  $1420^\circ\text{C}$  by a radio-frequency heater. The furnace atmosphere is high-purity argon at either 1 atm pressure or lower. A rotating seed of the desired crystallographic orientation is dipped into the melt which is rotated in the opposite direction to the seed. When suitably wetted by the melt the seed is withdrawn and allowed to grow outward to the desired diameter by adjusting the pull rate and melt temperature. A typical

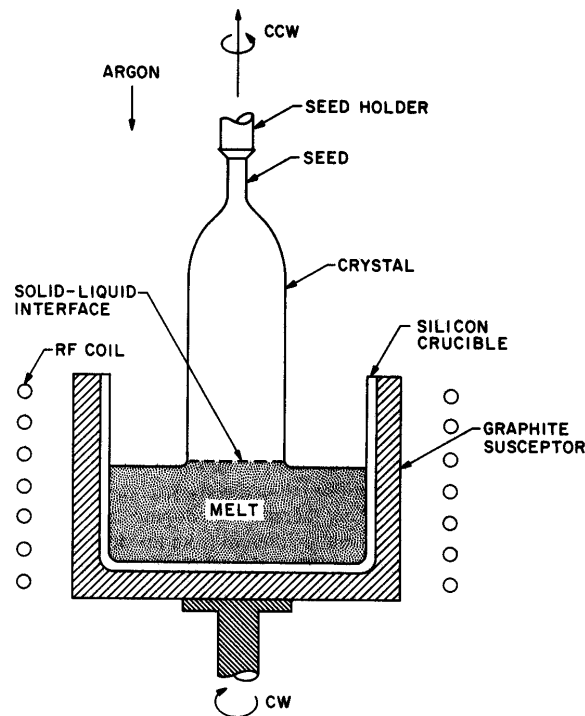


**Figure 1.1:** Schematic diagram of Czochralski (CZ) technique.

pull rate is a few millimeters per minutes. This technique is also applied to grow other materials such as Ge, GaAs and etc at a suitable environments.

Usually, the crystals so produced are contaminated with impurity atoms coming from the surroundings where the crystal growth takes place, facilitated by the nec-

essary high temperature which allows fast movement of the impurities during the process. Commonly occurring impurities are oxygen, carbon and hydrogen. The oxygen and carbon concentrations are substantially higher in Czochralski (CZ) crystal than in float zone crystals due to the dissolution of the silica crucible (for oxygen) and transport to the melt from the graphite susceptor (for carbon) during crystallization. Typical carbon concentrations range from  $10^{16}$  to about  $10^{17}$  atoms/cm<sup>3</sup>. Oxygen is commonly found in silicon at concentration from  $10^{17}$  to  $10^{18}$  atoms/cm<sup>3</sup>. However, its presence has both detrimental as well as beneficial effects. It acts as a donor at the substitutional site, but, oxygen in an interstitial lattice site can increase the yield strength of silicon by introducing undesired dislocations.

Single crystal silicon and germanium have the same diamond lattice structure (Figure 1.2). Each atom in this structure is surrounded by four equidistant nearest neighbors that lie at the corner of a tetrahedron.

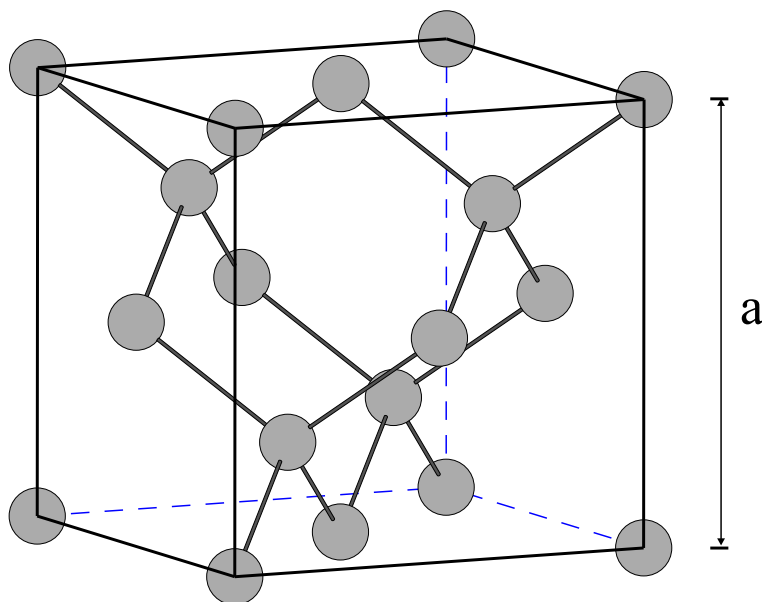


**Figure 1.2:** A unit cell of the diamond lattice structure.

Physical data	Germanium	Silicon
Atomic number	32	14
Average atomic weight	72.59	28.08
Density at 298.15K	5.326g/cm <sup>3</sup>	2.329g/cm <sup>3</sup>
Lattice constant 298.15K	5.65Å	5.43Å
Melting point	937°C	1412°C
Space group	Fd3m(O <sub>h</sub> <sup>7</sup> )	Fd3m(O <sub>h</sub> <sup>7</sup> )

**Table 1.1:** Physical constants of Ge and Si.

## 1.2 Electrical properties

The electrical properties of silicon and germanium are similar to nonmetals at low temperature because of their low electrical conductivity in this temperature range. However, they act like metals at high temperature by improving their ability to conduct electricity. Figure 1.3 shows an increase in the electrical conductivity of Ge and

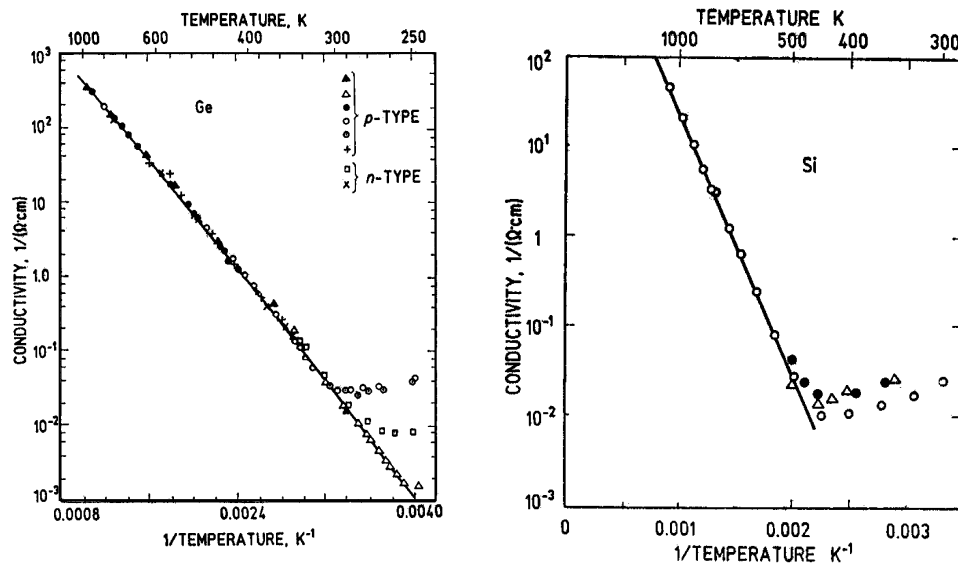


**Figure 1.3:** The electrical conductivity of Ge and Si versus temperature in the intrinsic region [DARG94].

Si as the result of a rise in the sample temperatures. Thermal excitation of charge carriers from the valence to the conduction band is responsible for the improvement of electric conductivity at high temperatures in intrinsic semiconductors. Silicon and germanium have an energy band gap of 1.12 eV and 0.66 eV, respectively, which determines the electrical properties of both materials for industrial applications. Germanium proved unsuitable in many applications because germanium devices exhibited high leakage currents at only moderately elevated temperature. On the other hand, silicon devices exhibit much lower leakage currents and high-quality silicon dioxide can be grown thermally. Silicon dioxide is a very good insulator and plays a vital role in the construction of integrated circuits. Moreover, germanium oxide is water soluble and unsuited for device fabrication. Nevertheless, germanium and germanium oxides are transparent to infrared radiation and are used in infrared spectrometers and other applications like optical fibers.

In many cases, the electrical properties of the material can be altered by doping with different impurity atoms. This can be achieved by either implantation or diffusion of the impurity atoms in the material. When a semiconductor is doped with impurities,

the material becomes extrinsic and new impurity energy levels are introduced in the energy band gap. For example, when an atom from group-V replaces a host atom in a silicon crystal, there will be an extra electron left after forming the covalent

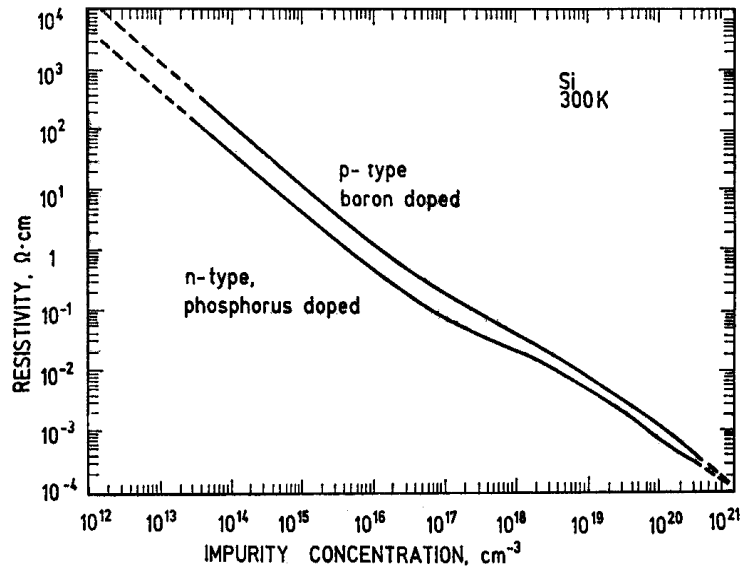


**Figure 1.4:** *The resistivity of Si as a function of impurity concentration [SZE81].*

bonds with the surrounding atoms. This extra electron can move about freely and thus increases the charge carrier concentration in the conduction band, making the material n-type silicon. The group-III acceptor atoms in silicon leave behind an extra hole in the valence band resulting in a p-type semiconductor. The same is true for germanium. The electrical measurements show a significant reduction on the resistivity of silicon by doping it with phosphorous and boron (Figure 1.4).

# Chapter 2

## HYPERFINE INTERACTION and ANGULAR CORRELATION

### 2.1 Hyperfine interaction

The observation of the microscopic environment in a solid is possible using nuclear methods whose working principles are based on the interaction between the nuclear moments of the probe nucleus and the surrounding electromagnetic fields. The fields are usually caused by the charges from atoms in the vicinity of the nucleus or by the external sources. The interaction of moments (magnetic or electric) of the nucleus with electromagnetic fields is called *Hyperfine Interaction*. This interaction was discovered in atomic spectroscopy and its effects on atomic spectra have been extensively investigated. However, the hyperfine field also affects the nucleus and makes possible the determination of internal fields in solids through the measurements of nuclear properties. The following sections discuss the basic theory that is used to describe the electrical interactions, i.e. the interaction between the quadrupole moment of the nucleus and electric fields.

#### 2.1.1 Classical electrostatic hyperfine interaction

In a solid, a nucleus is surrounded by electrical charges which produce a potential  $\phi(\vec{r})$  at the site of the nucleus. Classically, the electrostatic interaction energy of a nuclear charge distribution  $\rho(\vec{r})$  in an external potential  $\phi(\vec{r})$  is given by

$$E_{elec} = \int \rho(\vec{r})\phi(\vec{r})d\tau^3 \quad \text{where } \int \rho(\vec{r})d\tau^3 = Ze \quad (2.1)$$

is the total nuclear charge. Assuming the potential  $\phi(\vec{r})$  to range slowly over the region of the nuclear charge distribution, where  $\rho(\vec{r})$  is non-negligible, the potential can be expanded in a Taylor series around  $\vec{r} = 0$  near the center of the nucleus as

$$\phi(r) = \phi(0) + \sum_{\alpha=1}^3 \left( \frac{\partial\phi}{\partial x_{\alpha}} \right)_0 x_{\alpha} + \frac{1}{2} \sum_{\alpha} \sum_{\beta} \left( \frac{\partial^2\phi}{\partial x_{\alpha}\partial x_{\beta}} \right)_0 x_{\alpha}x_{\beta} + \dots \quad (2.2)$$

When equation (2.2) and the expression for the nuclear charge is inserted into (2.1), the energy takes the form

$$E_{elec} = \phi(0)Ze + \sum_{\alpha=1}^3 \left( \frac{\partial \phi}{\partial x_{\alpha}} \right)_0 \int \rho(r) x_{\alpha} d^3r + \frac{1}{2} \sum_{\alpha} \sum_{\beta} \left( \frac{\partial^2 \phi}{\partial x_{\alpha} \partial x_{\beta}} \right)_0 \cdot \int \rho(r) x_{\alpha} x_{\beta} d^3r + \dots \quad (2.3)$$

The first term is the Coulomb energy of point charges, which only contributes to the potential energy of the crystal lattice and is therefore of no interest in the discussion of hyperfine interactions. The second term is the electric dipole interaction, which vanishes because atomic nuclei possess no electric dipole moment (parity conservation). The third term  $E^{(2)}$  contains the isomeric shift and the quadrupole interaction. It can be written as follows by introducing  $r^2 = \sum_{\alpha} x_{\alpha}^2$

$$E^{(2)} = \frac{1}{6} \sum_{\alpha} \sum_{\beta} \phi_{\alpha\beta} \int \rho(r) r^2 d^3r + \frac{1}{6} \sum_{\alpha} \sum_{\beta} \phi_{\alpha\beta} \int \rho(r) \left( 3x_{\alpha} x_{\beta} - r^2 \delta_{\alpha\beta} \right) d^3r \quad (2.4)$$

where the quantity  $\phi_{\alpha\beta}$  is

$$\phi_{\alpha\beta} = : \left( \frac{\partial^2 \phi}{\partial x_{\alpha} \partial x_{\beta}} \right) \quad (2.5)$$

a symmetric (3x3)-matrix, which can be diagonalized by a rotation of the coordinate system. Since the electrostatic potential  $\phi(r)$  satisfies Poisson's equation  $\Delta\phi = -4\pi\rho_e(\vec{r})$ , which holds true especially near  $\vec{r} = 0$ . Hence, the gradient of  $\phi$  at  $\vec{r} = 0$  is

$$(\Delta\phi)_0 = \sum_{\alpha} \phi_{\alpha\alpha} = 4\pi e |\psi(0)|^2 \quad (2.6)$$

where  $-e \cdot |\psi(0)|^2$  is the charge density of the atomic electrons at the nucleus. Applying suitable choice of rotation of the coordinate axes to equation (2.4), the electrostatic hyperfine interaction would be

$$E^{(2)} = \underbrace{\frac{1}{6} \sum_{\alpha} \phi_{\alpha\alpha} \cdot \int \rho(r) r^2 d^3r}_{E_S} + \underbrace{\frac{1}{6} \sum_{\alpha} \sum_{\beta} \phi_{\alpha\beta} \int \rho(r) \left( 3x_{\alpha} x_{\beta} - r^2 \delta_{\alpha\beta} \right) d^3r}_{E_Q} \quad (2.7)$$

$$E^{(2)} = E_S + E_Q$$

The first term, the isomeric shift  $E_S$ , reflects the interaction between the extended charge of the nucleus and the charge density of the electrons at the nucleus. Substituting equation 2.1 into the expression  $E_S$  and performing the integration over the nuclear charge distribution, one obtains

$$E_S = \frac{4\pi}{3} Ze |\psi(0)|^2 \langle r \rangle^2 \quad (2.8)$$

Therefore, the isomeric shift ( $E_S$ ) does not explicitly depend on the angular momentum of the nucleus. Instead, it depends on the mean square radius of the nucleus. Thus, this only leads to a shift of the nuclear energy levels but not to a splitting of the degenerate  $m$  sub-states.

The quadrupole term  $E_Q$  describes the interaction between the electric field gradient and the non-spherical part of the nuclear charge distribution, i.e. the quadrupole moment tensor.

### 2.1.2 Quantum mechanical treatment of the electrostatic hyperfine interaction

The interaction between quadrupole moment of the nucleus and the local electric field gradient results in a splitting of the energy levels of the different states of the nucleus. Since the energy levels or states of a nucleus are described by the quantum number of the local angular momentum  $I$  and its projection  $m$  along the  $z$ -axis, it is useful to calculate the electrostatic interaction in the framework of the nuclear wave function. The interaction energy is defined as the matrix element of the electrostatic Hamiltonian ( $H_{el}$ )

$$E_m = \langle Im | H_{el} | Im' \rangle \quad (2.9)$$

The Hamiltonian that describes the interaction of a fixed electrostatic field gradient with the electric quadrupole moment of a nuclear state is given by [MATT62]

$$H_Q = \frac{4\pi}{5} T^{(2)} V^{(2)} = \frac{4\pi}{5} \sum_q (-1)^q T_q^{(2)} V_{-q}^{(2)} \quad (2.10)$$

where  $T^{(2)}$  is the second rank tensor operator of the nuclear quadrupole moment and  $V^{(2)}$  is the tensor operator of the classical external field gradient. By writing the field tensor  $V_q^{(2)}$  in a cartesian coordinate system, and choosing a principal axes system such that the mixed derivatives of the potential  $V$  disappear, hence, the field tensors become

$$\begin{aligned} V_0^{(2)} &= \frac{1}{4} \sqrt{\frac{5}{\pi}} V_{zz} \\ V_{\pm 1}^{(2)} &= 0 \\ V_{\pm 2}^{(2)} &= \frac{1}{4} \sqrt{\frac{5}{6\pi}} (V_{xx} - V_{yy}) = \frac{1}{4} \sqrt{\frac{5}{6\pi}} \eta V_{zz}. \end{aligned} \quad (2.11)$$

A parameter  $\eta = \frac{V_{xx} - V_{yy}}{V_{zz}}$  is introduced in equation (2.11), which measures the symmetry of the field with respect to quantization axis  $z$ . For axially symmetric fields ( $\eta = 0$ ), the field tensor operator reduces to the form

$$V_0^{(2)} = \frac{1}{4} \sqrt{\frac{5}{\pi}} V_{zz} \quad (2.12)$$



Therefore, from equations (2.10) and (2.12) the Hamiltonian of axially symmetric quadrupole interaction can be obtained as

$$H_Q = \sqrt{\frac{\pi}{5}} \cdot T_0^{(2)} V_{zz} \quad (2.13)$$

and the energy eigenvalues of the interaction are obtained by applying  $H_Q$  to the states that describe the interactions. It can be written here in terms of the eigenvectors  $|Im\rangle$  as

$$E_m = \langle Im | H_Q | Im' \rangle = \sqrt{\frac{\pi}{5}} V_{zz} \cdot \langle Im | T_0^{(2)} | Im' \rangle \quad (2.14)$$

The quadrupole moment of a nucleus is usually defined as the  $I = m$  component of the tensor [RECH80]

$$eQ = \langle II | \sum_p \rho_p (3z_p - r_p) | II \rangle = 4\sqrt{\frac{5}{\pi}} \langle II | T_0^{(2)} | II \rangle \quad (2.15)$$

Applying the Wigner-Eckart theorem to (2.14) and (2.15), one gets

$$E_m = (-1)^{I-m} \sqrt{\frac{5}{\pi}} V_{zz} \begin{pmatrix} I & 2 & I \\ -m & 0 & m \end{pmatrix} \cdot \langle I || T^{(2)} || I \rangle \quad (2.16)$$

and

$$eQ = 4\sqrt{\frac{\pi}{5}} \begin{pmatrix} I & 2 & I \\ -I & 0 & I \end{pmatrix} \langle I || T^{(2)} || I \rangle \quad (2.17)$$

Inserting (2.17) into (2.16) and evaluating the 3-j symbols leads to the energy eigenvalues of the quadrupole interaction

$$E_m = \frac{3m^2 - I(I+1)}{4I(2I-1)} \cdot eQ V_{zz} \quad (2.18)$$

Due to the  $m^2$ -dependence of the quadrupole interaction energy, there is still a twofold degeneracy of each energy levels. The term  $Q$  is the quadrupole moment of the nucleus that is subject to the external field. The energy difference between two the substates  $m$  and  $m'$  is then given by

$$E_m - E_{m'} = \frac{3 \cdot eQ V_{zz}}{4I(2I-1)} |m^2 - m'^2| \quad (2.19)$$

The difference  $|m^2 - m'^2|$  are integral numbers. Unlike the case of magnetic interaction, the splitting of levels is not equidistant in the electrostatic interaction (see Figure 2.1). The fundamental frequency of the interaction ( $\omega_Q$ ) is now defined as

$$\omega_Q = \frac{eQ V_{zz}}{4I(2I-1)\hbar} \quad (2.20)$$

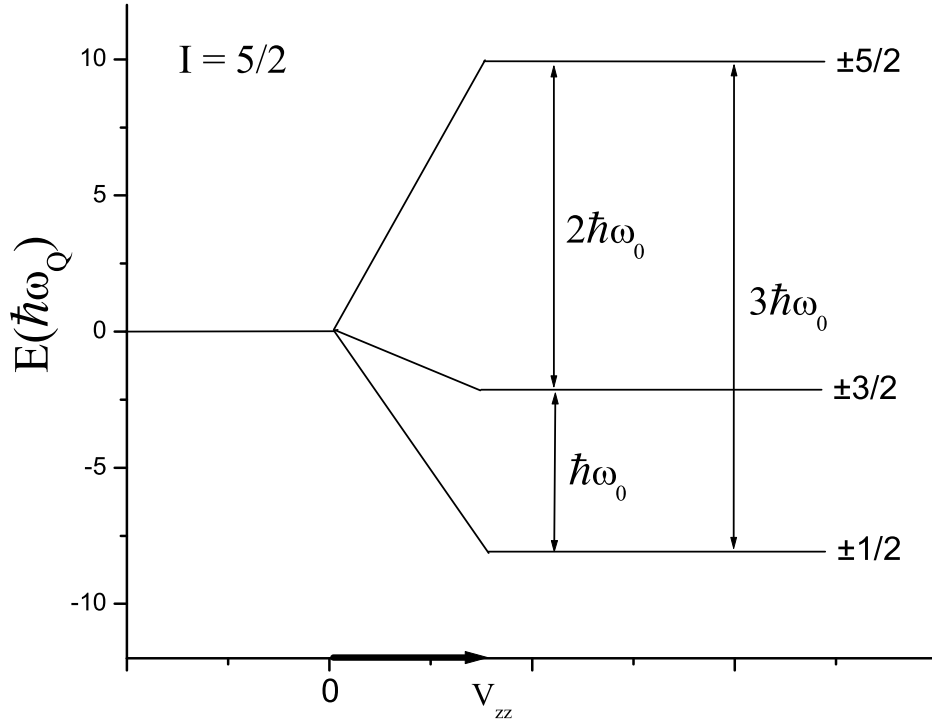


**Figure 2.1:** The splitting of the intermediate energy level for the spin  $I=5/2$  and  $\eta=0$ .

in terms of which equation 2.19 follows

$$E_m - E_{m'} = 3\hbar\omega_Q |m^2 - m'^2| \quad (2.21)$$

The frequency ( $\omega_0$ ) corresponding to the smallest non-vanishing energy difference is

$$\omega_0 = \begin{cases} 6\omega_Q & \text{for half integer nuclear spin } I \\ 3\omega_Q & \text{for integer nuclear spin } I \end{cases} \quad (2.22)$$

Figure 2.1 shows the splitting of energy level of the intermediate state of a nucleus with spin  $I = 5/2$ , as the result of static electric quadrupole interaction. For  $\eta = 0$  the ratio of the transition frequencies are  $\omega_1 : \omega_2 : \omega_3 = 1 : 2 : 3$ ; the smallest transition frequency in this case would be  $\omega_1 = \omega_0$ , the remaining components can be obtained by the relation  $\omega_n = n\omega_0$  ( $n = 1, 2, 3$ ).

In the case of a non-axially symmetric field ( $\eta \neq 0$ ), the Hamiltonian describing pure electrostatic quadrupole interaction is written in a form [GERD69]

$$H_Q = \{3I_z^2 - I(I+1) + \frac{\eta}{2}(I_+^2 + I_-^2)\}\hbar\omega_Q \quad (2.23)$$

where  $I_z$ ,  $I_+$  and  $I_-$  are designate angular momentum operators. The quantities  $\omega_Q$  and  $\eta$  are defined as

$$\omega_Q = \frac{eQV_{zz}}{4I(2I-1)\hbar} \quad \text{and} \quad \eta = \frac{V_{xx} - V_{yy}}{V_{zz}} \quad (2.24)$$

In order to calculate the energy eigenvalues, the interaction matrix  $\langle Im|H_Q|Im' \rangle$  has to be diagonalized. This can be achieved by the unitary transformation of the Hamiltonian ( $H_Q$ ) [PUTZ89]. For the spin  $I = \frac{5}{2}$ , which is of interest to the discussion of this work, the resulting energy eigenvalues are

$$\begin{aligned} E_{\pm 5/2} &= E_0 + 2\alpha\hbar\omega_Q \cos(1/3 \arccos\beta) \\ E_{\pm 3/2} &= E_0 - 2\alpha\hbar\omega_Q \cos(1/3(\pi + \arccos\beta)) \\ E_{\pm 3/2} &= E_0 - 2\alpha\hbar\omega_Q \cos(1/3(\pi - \arccos\beta)) \end{aligned} \quad (2.25)$$

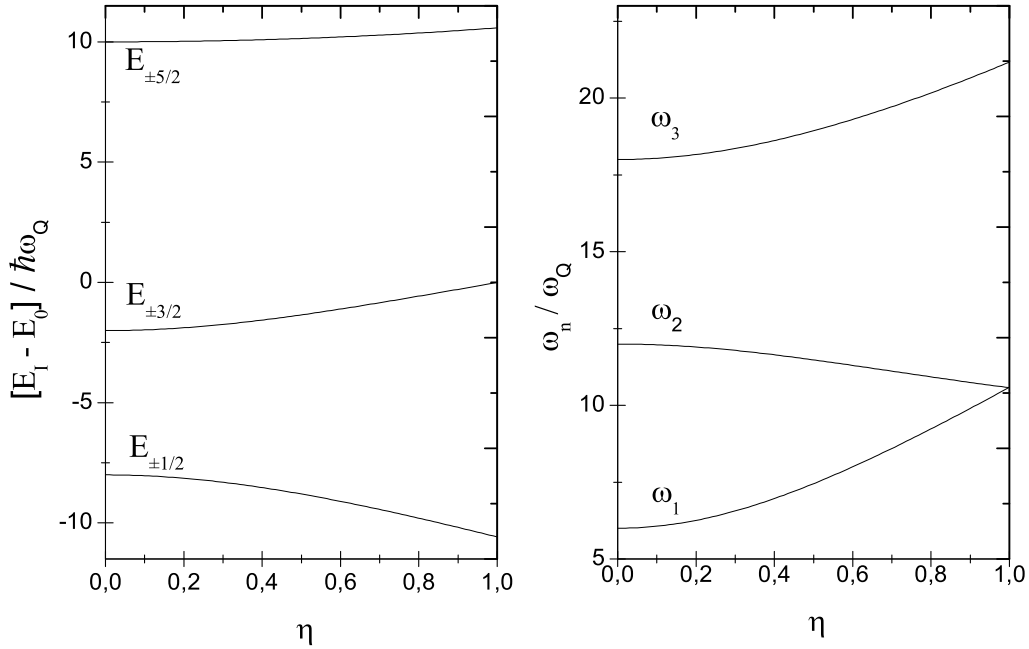


**Figure 2.2:** The splitting of the intermediate energy levels of spin  $I = 5/2$  and associated transition frequencies as a function of the asymmetry parameter ( $\eta$ ) according to eq. 2.25 and 2.27

$$\text{where } \alpha \text{ and } \beta \text{ are } \alpha = \sqrt{28(1 + \eta^2/3)} \quad \text{and} \quad \beta = \frac{80(1 - \eta^2)}{\alpha^3} \quad (2.26)$$

The corresponding expressions of the spin precession frequencies are

$$\begin{aligned} \omega_1 &= 2\sqrt{3}\alpha\omega_Q \sin(1/3 \arccos\beta) \\ \omega_2 &= 2\sqrt{3}\alpha\omega_Q \sin(1/3(\pi - \arccos\beta)) \\ \omega_3 &= \omega_1 + \omega_2 = 2\sqrt{3}\alpha\omega_Q \sin(1/3(\pi + \arccos\beta)) \end{aligned} \quad (2.27)$$

Figure 2.2 shows the splitting of an energy level as a function of the asymmetry parameter ( $\eta$ ), according to equations (2.25) and (2.26). It also reveals the  $\eta$  dependence of the associated transition frequencies as given in equation 2.27.

The value of the asymmetric parameter defined by equation 2.24, in the principal axes system with the convention  $|V_{xx}| \leq |V_{yy}| \leq |V_{zz}|$ , is restricted to  $0 \leq \eta \leq 1$ . Therefore, the electric field gradient tensor can be described for most applications by two parameters i.e.  $V_{zz}$  and  $\eta$ . In literature, the quadrupole coupling constant ( $\nu_Q$ ) is often used instead of  $V_{zz}$ , which is now defined as

$$\nu_Q = g(\eta) \cdot \frac{eQV_{zz}}{h} = g(\eta) \cdot \frac{10}{3\pi}\omega_1 \quad (2.28)$$

when  $\eta = 0$  the value of  $g = 1$  [WICH89].

## 2.2 Theory of angular correlation

### 2.2.1 Introduction

Angular correlation is a method widely used to study the property of unstable nuclei through the interaction of the nuclear moments with the surrounding electromagnetic fields. The basic idea of angular correlation stems from the fact that the probability of emission of a particle or quantum by a radioactive nucleus depends in general on the angle between the nuclear spin axis and the direction of emission. Under ordinary circumstances, the total radiation from a radioactive sample is isotropic because the nuclear spins are randomly oriented in space. An anisotropic radiation pattern can be observed only from nuclei that have a specific spacial orientation. In a radioactive source containing a nucleus that decays by two  $\gamma$ -transitions (see Figure 2.3), for example, detecting the first emission  $\gamma_1$  by a detector situated at a certain direction, one will preferentially select an ensemble of nuclei whose spins lie on the same direction. The emission probability of  $\gamma_2$  with respect to the first will then be anisotropic.

In angular correlation measurements the decaying nucleus has to satisfy certain criteria: large nuclear magnetic or electric quadrupole moment and anisotropic coefficient ( $A_{kk}$ ) are always an advantage. It should have sufficient mean life time for the intermediate state of the cascade. The mean life time  $\tau$  of the intermediate state should be long enough to cause an appreciable change in the orientation of the nuclear ensemble by virtue of the interaction of the static electromagnetic moments of the individual nuclei with electromagnetic fields. On the other hand, such an interaction would also lead to the perturbation of the correlation.

Perturbations of the angular correlation by extranuclear fields can be categorized into three different classes according to the time behavior of the fields at the site of the nucleus

a) **Static** interactions are caused by the coupling of the nuclear moments with static extranuclear fields, i.e. fields that are constant in magnitude and direction during the life time of the intermediate state.

- b) **Periodic** interaction occurs if the interacting fields vary periodically in time.
- c) **Time-dependent (relaxation)** interactions are caused by fluctuating fields, such as the fields experienced by nuclei in a liquid environment or in spin-relaxation phenomena.

In the following subsections, brief discussions about the theory of perturbed  $\gamma$ - $\gamma$  angular correlation method are given. A comprehensive presentation of the theory is found in [FRAU65] and [STEF75]. Here, it is only intended to discuss the correlation function of the interaction between the nuclear quadrupole moment and electrostatic field gradient. The term angular correlation can be applied to both directional correlations (if only the directions of the two photons are detected) and polarization correlation (if only the polarization of  $\gamma$ -ray is determined). The latter will not be discussed here since it has no relevance to the current measurements.

### 2.2.2 Directional angular correlation function

In the last subsection, it is indicated that an anisotropic radiation pattern is observed only when the spins of the decaying nuclei have a preferred spatial orientation. Quantum mechanical description of this phenomena states that: nuclei that have their spins aligned along a certain direction have non-uniformly populated magnetic sub-levels, characterized by the quantum number  $m$  and  $m'$ . Hence, only an ensemble of nuclei with an unequal population of  $m$  sub-states can produce a spatially anisotropic distribution radiation of  $\gamma$ -ray.

Uneven population of  $m$  sub-states can be achieved by selecting an ensemble of nuclei whose spin happen to lie in the same direction. This preferential selection can be accomplished by the detection of one of the photons in a cascade (see Figure 2.3). When the first  $\gamma$ -ray is detected in a certain direction, a group of nuclei with particular spin orientation are populated on the intermediate level. The distribution pattern of the succeeding (depopulation) radiation,  $\gamma_2$ , is anisotropic and reflects the unequal sub-levels of population of the intermediate spin  $I$ . As this anisotropic pattern can only be observed with respect to the first populating  $\gamma$ -ray, the spatial distribution of the second quantum is called *angular correlation*. In the absence of any electromagnetic fields at the site of the nucleus, the population of the  $m$  sub-state does not change until the emission of  $\gamma_2$ , resulting in a time independent distribution pattern. This process is therefore also referred to as the unperturbed  $\gamma$ - $\gamma$  angular correlation. This anisotropic distribution of radiation will depend on time if the nuclei are subject to extranuclear fields [WICH95].

In the directional correlation one observes the emission of two radiations,  $\gamma_1$  and  $\gamma_2$ . Hence, the directional angular correlation is described by the correlation function  $W(\vec{k}_1, \vec{k}_2)$ . The function  $W(\vec{k}_1, \vec{k}_2)$  is defined as the probability that a nucleus

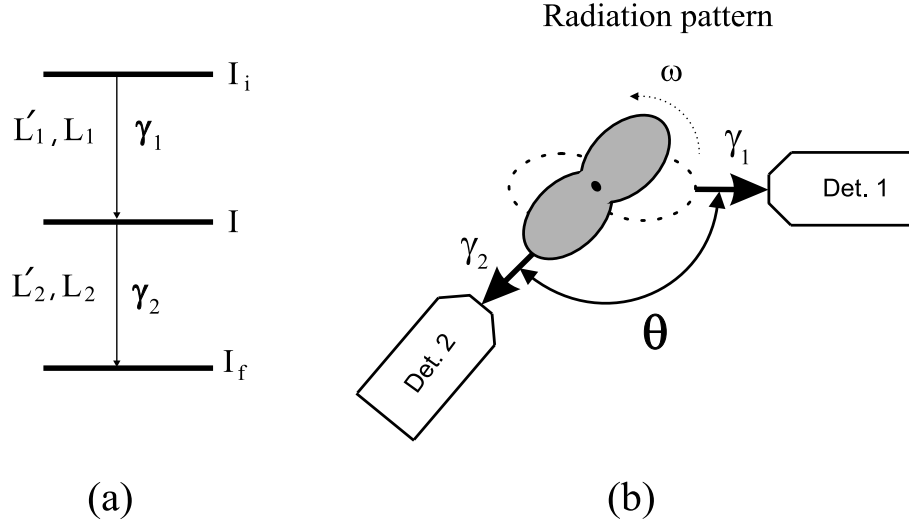


**Figure 2.3:** (a) Decay scheme of a  $\gamma - \gamma$  transition. (b) Schematic diagram of spatial distribution of radiation from ensemble of nuclei which have emitted  $\gamma_1$  into detector 1 and its evolution with time in the presence of an extranuclear field.

decaying through the cascade  $I_i \rightarrow I \rightarrow I_f$  emits the two radiations  $\gamma_1$  and  $\gamma_2$  in the directions  $\vec{k}_1$  and  $\vec{k}_2$  respectively into the solid angles  $d\Omega_1 d\Omega_2$  [FRAU65] as

$$W(\vec{k}_1, \vec{k}_2) = W(\theta) = \sum_k A_{kk} P_k(\cos\theta) \quad (2.29)$$

where  $\theta$  is the angle between  $\vec{k}_1$  and  $\vec{k}_2$ , and  $P_k$  are the Legendre polynomials. The coefficient  $A_{kk}$  is called anisotropy coefficient which depends on the properties of the decaying nucleus. It can be written as

$$A_{kk} = A_k(\gamma_1) A_k(\gamma_2) \quad (2.30)$$

where each component is given in terms of the so called  $F_k$  functions as [PUTZ89]

$$A_k(\gamma_1) = \frac{\{F_{k_1}(L_1, L_1; I_i, I) + (-1)^{L_1-L_1'} 2\delta_1 F_{k_1}(L_1, L_1'; I_i, I)\} + \delta_1^2 F_{k_1}(L_1', L_1'; I_i, I)}{(1 + \delta_1^2)} \quad (2.31)$$

$$A_k(\gamma_2) = \frac{\{F_{k_2}(L_2, L_2; I_f, I) + 2\delta_2 F_{k_2}(L_2, L_2'; I_f, I)\} + \delta_2^2 F_{k_2}(L_2', L_2'; I_f, I)}{(1 + \delta_2^2)} \quad (2.32)$$

The  $\delta_1$  and  $\delta_2$  are called the mixing ratios, which measure the mixing of the different angular momenta during emission of the radiations. The  $F_k$  coefficients are given in terms of the Wigner 3-j and 6-j symbols for combinations of angular momenta as

$$F_k(L, L'; I', I) = (-1)^{I+I'-1} [(2L+1)(2L'+1)(2k+1)(2I+1)]^{1/2} \cdot \begin{pmatrix} L & L' & k \\ 1 & -1 & 0 \end{pmatrix} \begin{Bmatrix} I & I & k \\ L' & L & I' \end{Bmatrix} \quad (2.33)$$

The sum runs over even values of  $k_1$  and  $k_2$  only as a consequence of parity conservation of the electromagnetic interaction which is responsible for the  $\gamma$ -emission.

The  $\gamma$ - $\gamma$  directional correlation of the cascade  $I_i \rightarrow I \rightarrow I_f$  in which both  $\gamma$  - rays of multipole order  $L_1$  and  $L_2$ , respectively are pure, the most convenient form of describing such directional correlation  $W(\theta)$  between  $\gamma_1$  and  $\gamma_2$  is

$$W(\vec{k}_1, \vec{k}_2) = W(\theta) = 1 + \sum_k A_{kk} P_k(\cos\theta) \quad (2.34)$$

The summation index  $k$  is an even integer as long as the correlation is directional. The highest term in the expression is determined by selection rule

$$0 < k < \text{Min}(2I, 2L_1, 2L_2) \quad (2.35)$$

where  $k_{max} = \text{Min}(2I, 2L_1, 2L_2)$ .

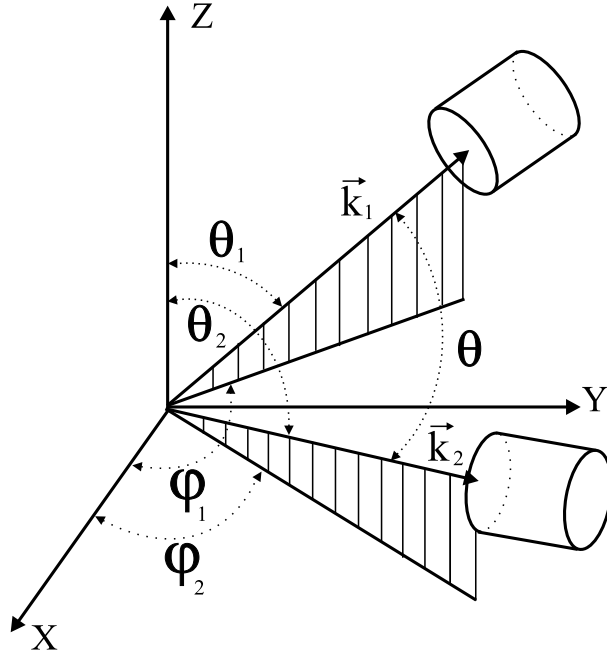


**Figure 2.4:** Emission direction of the gamma-rays in the laboratory system.

### 2.2.3 Extranuclear perturbation

The presence of extranuclear fields (electromagnetic fields) at the site of the decaying nucleus allows interaction between the fields and the nuclear moments, causing the degeneracy of the energy level, i.e. the sub-levels corresponding to different magnetic quantum numbers  $m$ . The strength of the local field is proportional to the width of the splitting of the level. Moreover, the interaction induces transitions between the different  $m$  states, resulting in a changed spatial orientation of the

nuclear spin. Consequently, the depopulating  $\gamma$ -quantum is emitted in a direction other than it would have been in the absence the external nuclear fields. Hence, the angular correlation will become time dependant as a result of interactions between the moments of the intermediate level and the local fields, reflecting the dynamic changes in the sub-level population. These change are contained in a perturbation function  $G_{kk}(t)$  that now enters the expression for the angular correlation. In a polycrystalline source the correlation function would be

$$W(\theta) = \sum_k A_{kk} G_{kk}(t) P_k(\cos\theta) \quad (2.36)$$

In the density matrix formalism of the decay through the cascade ( $I_i \rightarrow I \rightarrow I_f$ ), the density matrix  $\rho_a(\vec{k}_1)$ , describing the end product of the transition  $\gamma_1$ , is no longer identical with the density matrix  $\rho_b(\vec{k}_1)$  for the initial state of the second transition. The extranuclear fields cause transitions between the different m states of I and thus cause a change of the density matrix  $\rho_a(\vec{k}_1) \xrightarrow{\text{extranuclear interaction}} \rho_b(\vec{k}_1)$  during the time the intermediate state is exposed to the extranuclear interaction. The change of  $\rho_a(\vec{k}_1)$  can be described by a unitary transformation which depends on the interaction.

In other words, the interaction of the nucleus intermediate state I with some extranuclear fields can be described by the Hamiltonian (H), which is assumed to act from the time the first radiation is emitted ( $t = 0$ ) until the time t at which the second radiation is emitted. During this time interval the states  $|m_a\rangle$  change to different states  $|m_b\rangle$  under the influence of the extranuclear fields. This change can be represented by an unitary operator  $\Lambda(t)$  that describes the evolution of the state vectors  $|m_b\rangle$ , and thus the perturbed angular correlation can be expressed as

$$W(\vec{k}_1, \vec{k}_2, t) = \sum_{m_i m_f m_a m'_a} \langle m_f | H_2 \Lambda(t) | m_a \rangle \langle m_a | H_1 | m_i \rangle \langle m_f | H_2 \Lambda(t) | m'_a \rangle^* \cdot \langle m'_a | H_1 | m_i \rangle^* \quad (2.37)$$

where  $H_1$  and  $H_2$  represent the interaction between nucleus and radiation field only. The states  $|m\rangle$  form a complete set and the state vector  $\Lambda(t)|m\rangle$  can be expressed as

$$\Lambda(t)|m_a\rangle = \sum_{m_b} |m_b\rangle \langle m_b | \Lambda(t) | m_a \rangle \quad (2.38)$$

and similar for  $\Lambda(t)|m'_a\rangle$ . The expansion coefficients are the matrix elements of the time - evolution operator  $\Lambda(t)$  in the m representation. The time evolution operator satisfies the Schrödinger equation

$$\frac{\partial}{\partial t} \Lambda(t) = -\frac{i}{\hbar} H \Lambda(t) \quad (2.39)$$

If H does not depend on the time t the solution of this equation is simply

$$\Lambda(t) = \exp(-iHt/\hbar) \quad (2.40)$$



Based on the unitary matrix representation, which can be written in terms of spherical harmonics  $Y_k^N(\theta, \varphi)$ , and the special choice of the quantization axis z as shown in Figure 2.4, the time dependent correlation function after some necessary mathematical steps would be

$$W(\vec{k}_1, \vec{k}_2, t) = \sum_{k_1 k_2, N_1 N_2} A_{k_1}(\gamma_1) \cdot A_{k_2}(\gamma_2) G_{k_1, k_2}^{N_1, N_2}(t) \cdot [(2k_1 + 1) \cdot (2k_2 + 1)]^{-1/2} \cdot Y_{k_1}^{N_1*}(\theta_1, \varphi_1) Y_{k_2}^{N_2}(\theta_2, \varphi_2) \quad (2.41)$$

The angles  $\theta$  and  $\varphi$  are the same as given in the Figure 2.4. The general form of perturbation function is defined as

$$G_{k_1 k_2}^{N_1, N_2}(t) = \sum_{m_a m_b} (-1)^{2I+m_a+m_b} \cdot [(2k_1 + 1) \cdot (2k_2 + 1)]^{-1/2} \langle m_b | \Lambda(t) | m_a \rangle \cdot \langle m'_b | \Lambda(t) | m'_a \rangle \begin{pmatrix} I & I & k_1 \\ m'_a & -m_a & N_1 \end{pmatrix} \begin{pmatrix} I & I & k_2 \\ m'_b & -m_b & N_2 \end{pmatrix} \quad (2.42)$$

Hence, the influence of the external perturbation is completely described by the perturbation function  $G_{k_1, k_2}^{N_1, N_2}(t)$ . The expression (2.42) represents the time-differential perturbed angular correlation, i.e., the correlation measured if the second radiation is observed within the time t and t+dt after the emission of the first radiation.

In real measurement, the second radiation is accepted at a time t after the emission of the first radiation with the probability  $f(t - T)$ . Here T is a delay at which the signal of the first radiation is suspended until the arrival of the second in the coincidence analyzer system. Therefore, the measured delayed correlation function is then given by the weighted average as [FRAU65]

$$\overline{W(\vec{k}_1, \vec{k}_2, T)} = \frac{\int_0^\infty f(t - T) e^{-t/\tau} W(\vec{k}_1, \vec{k}_2, t) dt}{\int_0^\infty f(t - T) e^{-t/\tau} dt} \quad (2.43)$$

The time-response function of the experimental apparatus is often approximated by the step function as

$$f(t - T) = \begin{cases} 1 & \text{for } T - \tau_o \leq t \leq T + \tau_o \\ 0 & \text{for } t > T + \tau_o \text{ and } t < T - \tau_o \end{cases} \quad (2.44)$$

where  $\tau_o$  is the time resolution of the apparatus, which is half of the full width at half maximum (FWHM) of the prompt curve at the time zero point. In this approximation, the observed angular correlation is given by

$$\overline{W(\vec{k}_1, \vec{k}_2, T)} = \frac{\int_{T-\tau_o}^{T+\tau_o} e^{-t/\tau} W(\vec{k}_1, \vec{k}_2, t) dt}{\int_{T-\tau_o}^{T+\tau_o} e^{-t/\tau} dt} \quad (2.45)$$

When the mean life time ( $\tau$ ) of the intermediate state is much shorter than the time resolution  $\tau_o$  of the coincidence measuring apparatus ( $\tau \ll \tau_o$ ), one observes the *time integrated correlation function* given by

$$\overline{W(\vec{k}_1, \vec{k}_2, \infty)} = \frac{1}{\tau} \int_0^\infty e^{-t/\tau} W(\vec{k}_1, \vec{k}_2, t) dt \quad (2.46)$$

Analogous definition can also be made for the time integrated perturbation coefficient, because only the perturbation factor depends on time in the correlation function.

$$\overline{G_{k_1 k_2}^{N_1 N_2}(\infty)} = \frac{1}{\tau} \int_0^\infty e^{-t/\tau} G_{k_1 k_2}^{N_1 N_2}(t) dt \quad (2.47)$$

## 2.3 Perturbation by static interaction

If the perturbation of the angular correlation is caused by the interaction of the nuclear moments (magnetic or electric) with a stationary external field that can be described classically, e.g., an externally applied magnetic field or a crystalline electric field gradient, the matrix elements of  $\Lambda(t)$  can easily be expressed in the m-representation. We designate the unitary matrix which diagonalizes the interaction Hamiltonian H by U

$$UHU^{-1} = E \quad (2.48)$$

where E is the diagonal energy matrix with the diagonal element  $E_n$  (energy eigenvalues). By expanding the exponential function, the following relation can be obtained

$$Ue^{-(i/\hbar)Ht}U^{-1} = e^{-(i/\hbar)Et} \quad (2.49)$$

Using equation (2.40), the time evolution operator is

$$\Lambda(t) = U^{-1}e^{-(i/\hbar)Et}U \quad (2.50)$$

Therefore, the matrix elements of  $\Lambda(t)$  in the m-representation are

$$\langle m_b | \Lambda(t) | m_a \rangle = \sum_n \langle n | m_b \rangle^* e^{-(i/\hbar)E_n t} \langle n | \Lambda(t) | m_a \rangle \quad (2.51)$$

where the  $\langle m | n \rangle$  are the matrix elements of the unitary matrix U that is obtained by solving the eigenvalue equation (2.48). The perturbation factor is then

$$\begin{aligned} G_{k_1 k_2}^{N_1 N_2}(t) &= \sum_{m_a m_b n n'} (-1)^{2I+m_a+m_b} \cdot [(2k_1+1)(2k_2+1)]^{-1/2} \\ &\cdot \exp(-i/\hbar) \cdot ((E_n - E_{n'}) \cdot t) \langle n | m_b \rangle^* \langle n | m_a \rangle \langle n' | m'_b \rangle \\ &\cdot \langle n' | m'_a \rangle^* \begin{pmatrix} I & I & k_1 \\ m'_a & -m_a & N_1 \end{pmatrix} \begin{pmatrix} I & I & k_2 \\ m'_b & -m_b & N_2 \end{pmatrix} \end{aligned} \quad (2.52)$$

In a situation where the perturbing field is axially symmetric guarantees  $N_1 = N_2 = N$ , but  $k_1$  need not be identical to  $k_2$ . The symmetry axis of the interaction can be chosen parallel to z and as the quantization axis for the eigenfunctions of the

Hamiltonian  $H$ . The eigenfunctions  $|m\rangle$  and the evolution matrix  $\Lambda(t)$  are then diagonal in this representation ( $U = 1$ )

$$\langle m_b | \Lambda(t) | m_a \rangle = \exp[-(i/\hbar)E_m t] \delta_{mm_a} \delta_{mm_b} \quad (2.53)$$

The perturbation factor (2.42) now reduces to

$$G_{k_1 k_2}^{NN}(t) = \sum_m [(2k_1 + 1)(2k_2 + 1)]^{-1/2} \begin{pmatrix} I & I & k_1 \\ m' & -m & N \end{pmatrix} \begin{pmatrix} I & I & k_2 \\ m' & -m & N \end{pmatrix} \cdot \exp(-i/\hbar) \cdot ((E_m - E_{m'}) \cdot t) \quad (2.54)$$

Important information can be derived from this choice of axis. If the axially symmetric field is parallel to the propagation direction of one of the two radiations e.g.,  $\gamma_1$ , then  $Y_{k_1}^N(0, \varphi) = \delta_{N,0} [(2k_1 + 1)/4\pi]^{1/2}$ , and only the terms  $m = m'$ , i.e.,  $E_m - E_{m'} = 0$  occur. The orthogonality relation of the 3-j symbols can be used in equation (2.54) and we obtain  $G_{k_1, k_2}^{N,N}(t) = \delta_{k_1 k_2}$ . Therefore, the angular correlation is not influenced by such a field.

This fact can be understood on the basis of a semiclassical picture. If we chose  $\vec{k}_1$  as the quantization axis and the axially symmetric field is parallel to  $\vec{k}_1$ , then the influence of this field can be interpreted as a precession of the intermediate nuclear state about  $\vec{k}_1$ . The projection of  $I$  on  $\vec{k}_1$  does not change, and the population of the  $m$ -states with respect to  $\vec{k}_1$  remains the same. Thus, the angular distribution of the second radiation with respect to  $\vec{k}_1$  is not disturbed. This phenomena is often seen experimentally as an unperturbed time spectra, i.e. the perturbing field points toward the detectors. Good examples are given in the works of G. Marx [MARX95] in a strained diamond lattice and K. Lorenz [LORE02] in the hexagonal lattice structure.

In most cases, angular correlations are observed by using a radioactive source that consists of an ensemble of randomly oriented microcrystals. The observed angular correlation is obtained by averaging over the random directions of the symmetry axes of the microcrystals. Therefore, the perturbation factor of the powder source is

$$G_{kk}(t) = \overline{G_{k_1 k_2}^{N_1 N_2}(t)} \quad (2.55)$$

The perturbation factor  $G_{kk}(t)$  of the sources that as a whole display no privileged direction is therefore called *attenuation factor*.

The time-integrated attenuation factor of the static interaction of the powder source has finite lower limits or “hard core”. The hard core values are independent of the interaction written as

$$\overline{G_{kk}(\infty)}_{lim} = \frac{1}{2k + 1} \quad (2.56)$$

For the second order perturbation  $k = 2$  the hard core would be  $1/5$ . The meaning of this lower limit of the static interaction is that the anisotropic distribution of the second  $\gamma$ -ray never lost completely regardless of the field strength.

### 2.3.1 Perturbation factor for static electric quadrupole interaction

The name electric quadrupole interaction is derived from the interaction between the nuclear quadrupole moment and the electric field gradient (EFG) at the site of the nucleus. As has been discussed in the previous sections this interaction leads to the splitting of the intermediate level of the decaying nucleus, which in turn perturbs the angular correlation function. The Hamiltonian describing the axially symmetric electric quadrupole interaction (according to equ. 2.13) is given by

$$H_Q = \sqrt{\frac{\pi}{5}} \cdot T_0^{(2)} V_{zz} \quad (2.57)$$

Based on the discussion given in section 2.1.2 the resulting energy difference of the degenerate m-states is

$$E_m - E_{m'} = 3 \cdot \frac{eQV_{zz}}{4I(2I-1)} |m^2 - m'^2| = 3|m^2 - m'^2| \hbar\omega_Q \quad (2.58)$$

Substituting equation (2.58) into the energy term of (2.54), one obtains the perturbation factor for axially symmetric quadrupole interaction. In general, the perturbation factor can also be written in more instructive form as

$$G_{k_1, k_2}^{NN}(t) = \sum_n S_{nN}^{k_1 k_2} \cos(n\omega_Q t), \quad (2.59)$$

where the summation index n assumes all the positive integer values (including 0)

$$\begin{aligned} n &= |m^2 - m'^2| \quad \text{for integer } I \\ n &= 2|m^2 - m'^2| \quad \text{for half-integer } I \end{aligned} \quad (2.60)$$

The coefficient  $S_{nN}^{k_1 k_2}$  is given by

$$S_{nN}^{k_1 k_2} = \sum'_{mm'} \begin{pmatrix} I & I & k_1 \\ m'_a & -m_a & N \end{pmatrix} \begin{pmatrix} I & I & k_2 \\ m'_b & -m_b & N \end{pmatrix} [(2k_1 + 1) \cdot (2k_2 + 1)]^{-1/2} \quad (2.61)$$

where the prime on the  $\sum$  sign means that the summation over m and m' should only include those terms where m and m' satisfy the condition (2.60).

### POLYCRYSTAL SOURCE

The correlation function of the polycrystalline source is given in general according to the relation (2.36). In axially symmetric ( $\eta = 0$ ) quadrupole interaction the time dependent perturbation term is represented by the attenuation coefficient  $G_{kk}(t)$  [FRAU65]

$$G_{kk}(t) = \sum'_{m, m'} \left( \begin{matrix} I & I & k \\ m' & -m & p \end{matrix} \right)^2 \exp(-3i(m^2 - m'^2)\omega_Q \cdot t) \quad (2.62)$$

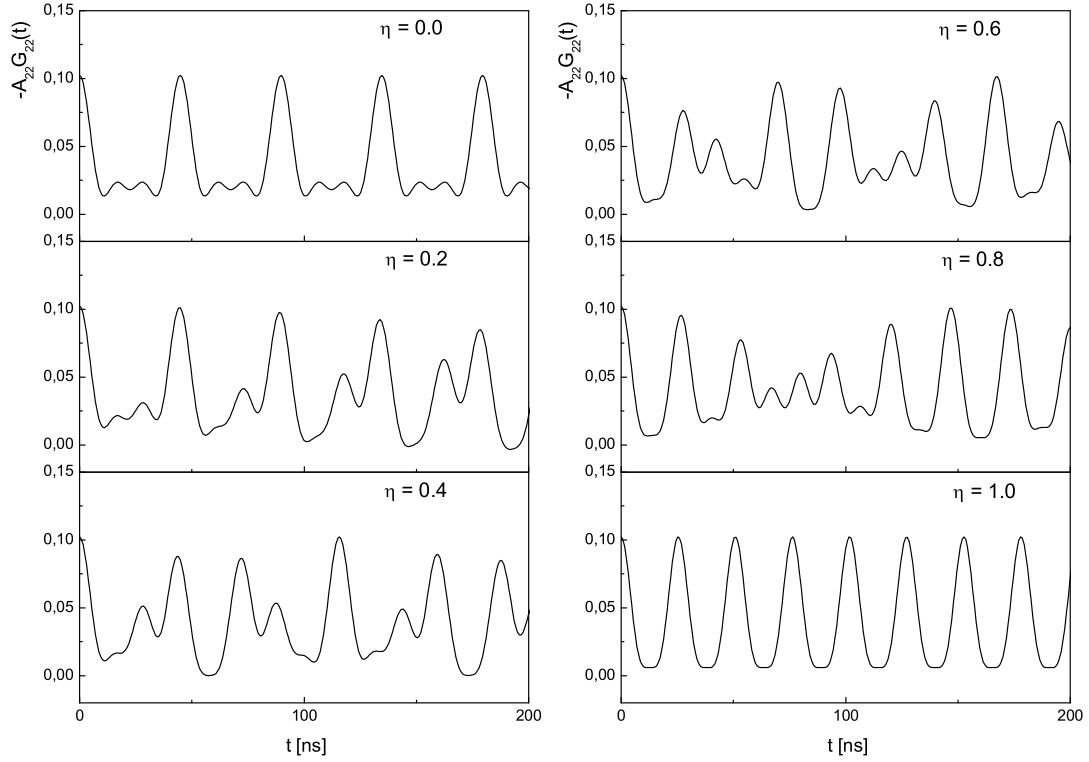


**Figure 2.5:** The figure shows a frequency pattern that varies with different values of the asymmetry parameter.

The quadrupole frequency  $\omega_Q$  is taken as defined by equation (2.24) and  $p = -m' + m$ . This expression can also be written in a form as

$$G_{k,k}(t) = \sum_n s_{kn} \cos(n\omega_0 t), \quad (2.63)$$

with

$$s_{kn} = \sum_{m,m'} \begin{pmatrix} I & I & k \\ m' & -m & -m' + m \end{pmatrix} \quad (2.64)$$

Again  $n$  satisfies the condition stated in equation (2.60). The  $s_{kn}$  can be determined to all allowed  $m$ -levels of the intermediate state,  $m$  and  $m'$ . The time integrated attenuation coefficients for polycrystalline sample can be obtained from equation (2.63) as

$$\overline{G_{kk}(\infty)} = \sum_n s_{kn} \frac{1}{1 + (n\omega_0\tau)^2} \quad (2.65)$$

For  $k = 2$  and spin  $I = 5/2$  the  $s_{2n}$  coefficients are

$$s_{20} = 0.2000 \quad s_{21} = 0.3714 \quad s_{22} = 0.2857 \quad s_{23} = 0.1429 \quad (2.66)$$

The limiting values for infinitely strong axially symmetric static quadrupole interaction are determined by the value of the hard core, which is given here in terms of the coefficient  $s_{kn}$  as

$$\overline{G_{kk}(\infty)} = s_{k0} \quad (2.67)$$

In a non-axially symmetric field the  $s_{kn}$  are polynomial functions of  $\eta$  (see Appendix C). Moreover, the existence of a non-zero asymmetry parameter ( $\eta$ ) in the perturbation function induces various modulation patterns of the interaction frequency. Figure 2.5 shows the various forms of the modulation pattern for different values of the asymmetry parameter. The simulated EFG was assigned to 80% of the population of the probe atoms (with spin  $I = 5/2$ ) in a polycrystalline sample.

### SINGLE CRYSTAL SOURCE

The solution of the angular correlation function for a crystalline source is even more difficult than for a polycrystal, because it takes into account the orientation of the field with respect to the host crystal. It uses the general form of time dependent correlation function defined by equation 2.41, which is thoroughly discussed by R. M. Steffen et al. in [STEF75] and given by

$$W(\vec{k}_1, \vec{k}_2, t) = \sum_{k_1 k_2, N_1 N_2} A_{k_1}(\gamma_1) \cdot A_{k_2}(\gamma_2) G_{k_1, k_2}^{N_1, N_2}(t) \cdot [(2k_1 + 1) \cdot (2k_2 + 1)]^{-1/2} \cdot Y_{k_1}^{N_1*}(\theta_1, \varphi_1) Y_{k_2}^{N_2}(\theta_2, \varphi_2) \quad (2.68)$$

where the  $A_k$ -coefficients are as defined by equations 2.31 and 2.32 and  $N = -m' + m$  for all combinations of the magnetic quantum numbers  $m'$  and  $m$ . The correlation function of axially symmetric field of the single crystalline source of spin  $I = 5/2$  is defined analog to the definition of the powder source as

$$W(\theta_1, \varphi_1, \theta_2, \varphi_2, t) = 1 + A_{22}G(\theta_1, \varphi_1, \theta_2, \varphi_2, t) \quad (2.69)$$

where the angles are as defined in Figure 2.4. Consequently, the perturbation function can be written as

$$G(\theta_1, \varphi_1, \theta_2, \varphi_2, t) = \sum_{n=0}^3 s_n^{eff}(\theta_1, \varphi_1, \theta_2, \varphi_2) \cos(n\omega t) \quad (2.70)$$

The  $s_n(\theta_1, \varphi_1, \theta_2, \varphi_2)$ -coefficients are derived by U. Pütz [PUTZ82], using the function  $Y_k^N(\theta, \varphi)$  and ratios that involve the various components of the anisotropy coefficients (see Appendix C). The spherical harmonic term ( $Y_k^N(\theta, \varphi)$ ) of the correlation function determines the modulation pattern of the interaction frequency depending on the orientation of the EFG with respect to the detectors. Figure 2.6 shows the shape of the perturbation functions in a diamond crystal in which the EFG lies along the  $\langle 100 \rangle$  crystal axis and the detectors are alternatively pointed toward one of the major axes as indicated on the panels. Unlike in polycrystal, the Fourier

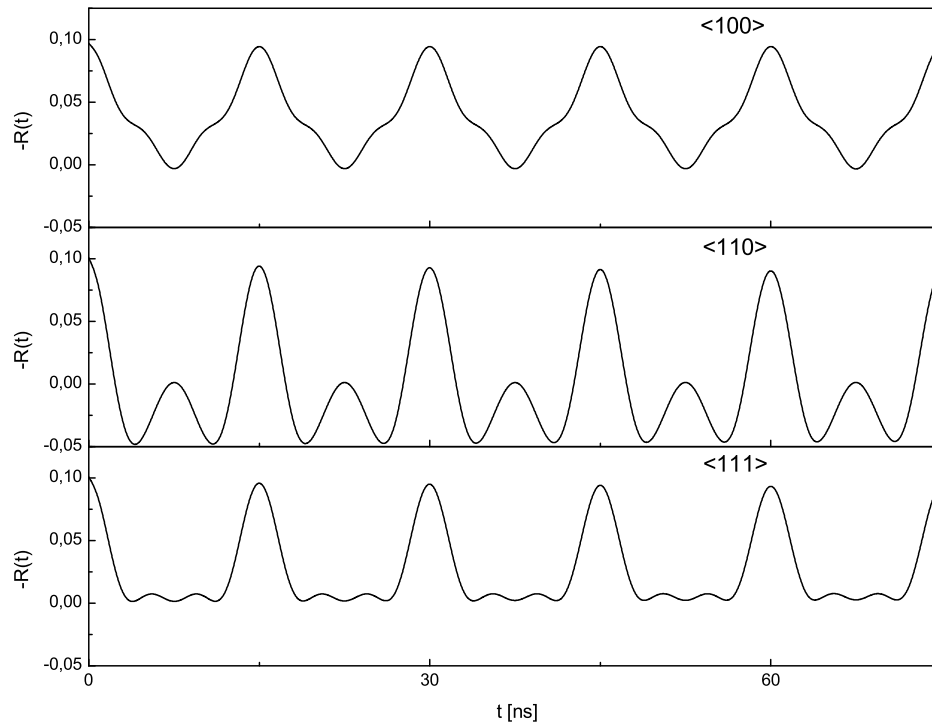


**Figure 2.6:** Various patterns of an interaction frequency whose EFG lies along the  $\langle 100 \rangle$  crystal axis in a diamond lattice. The detectors are pointed alternatively toward major axes as indicated in the panel.

transform of the time spectra also depends on the position of the crystal axes relative to the position of the detectors (see Appendix A.2). Additional information is provided in the next chapter which discusses the data reduction method and treatment of perturbation functions for single crystals.

# Chapter 3

## EXPERIMENTAL METHOD

### 3.1 Perturbed angular correlation (PAC)

The perturbed  $\gamma$ - $\gamma$  angular correlation(PAC) method is a nuclear technique which uses radioactive nucleus that decays by emitting two  $\gamma$ -rays in cascade. The observation of the microscopic environment of the probe atom is possible if the nuclear moment of the intermediate state of the cascade interacts with an electromagnetic field at the site of the probe nucleus. The fields are usually a result of the asymmetric charge distributions around the probe atoms and/or localized charges caused by a defect. The PAC is widely used for investigation of point defects in metals and semiconductors.

#### 3.1.1 Experimental set up

In the current experiments, a PAC set up was utilized which employed the so called fast-slow delayed coincidence technique. This PAC spectrometer consists of four BaF<sub>2</sub> scintillation detectors together with photomultiplier tubes and other necessary electronics (see Figure 3.1). There are two types of signals (time and energy) that must be extracted from the photomultipliers of the BaF<sub>2</sub> detectors for further processing in a coincidence unit. The time signals are fast in this time scale and carry information about the time, whereas the energy signals are slow and contains information about the energy of the emitted  $\gamma$ -rays. The fast and slow signals are independently transported using low-loss coaxial cables towards the TAC (Time-to-Amplitude Converter) and a Routing unit respectively, where they are measured in coincidence. The energy signals are amplified and shaped by a Double Delay Line (DDL)[1411A, CI] amplifier before they are taken to the single channel analyzer (SCA)[2037A, CI]. The SCA sets a window that filters the energies of the  $\gamma$ -rays. Based on the decay schema of the probe nucleus, each of the SCAs are adjusted in order to pass only a single  $\gamma$ -ray energy that would serve either as a START or a



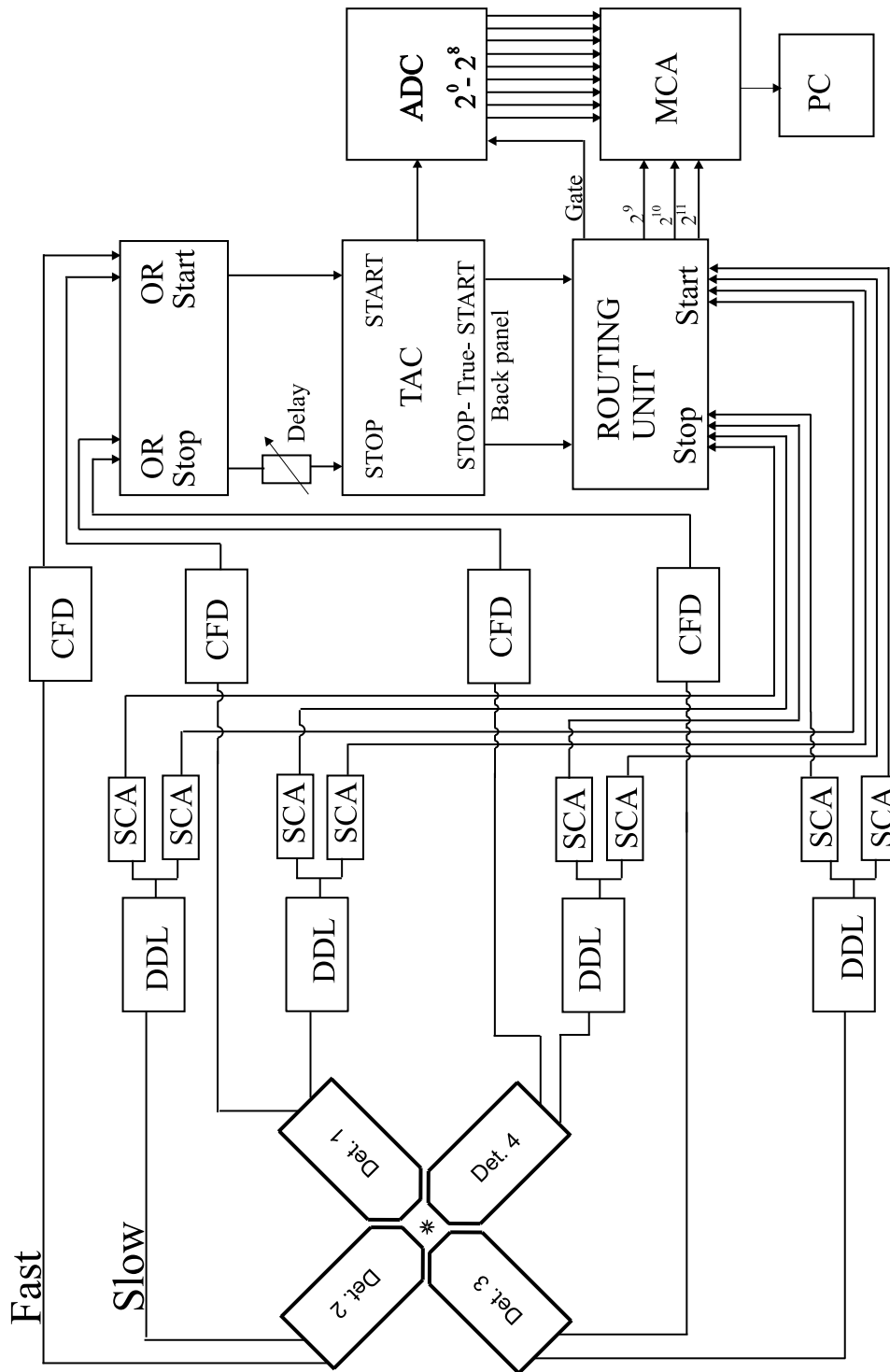


**Figure 3.1:** Schematic diagram of the PAC set up.

STOP signal. The time signals are fed from the anode of the photomultiplier of the BaF<sub>2</sub> detector to the Constant Fraction differential Discriminator (CFD)[583, CI], which generates accurate timing output signals. The clock starts at the occurrence of the first gamma-ray ( $\gamma_1$ ) of the transition in TAC, which would be the START

signal, and stops at the arrival of the second gamma-ray ( $\gamma_2$ ), which is the STOP signal. The signal which is intended to stop the clock is delayed by fixed delay time (x)ns before it is fed to the TAC [567, CI]. There are two outputs from the TAC for the different purposes: the first TAC output is the time difference between START and STOP converted into a voltage amplitude (analog form) and goes to the ADC (Analog to Digital Converter), and at the same time from the same START and STOP signals the second output goes to the Routing unit, which are called TRUE START and STOP. In the Routing unit the TRUE START and STOP time signals from the TAC and the energy signals from the slow branch are measured in coincidence and generate a gate to the ADC. Hence, only valid time signals are allowed to pass the gate. The digitalized valid time signals from the ADC will be stored in a Multichannel Analyzer (MCA) as a coincidence count rate to the addresses assigned by the Routing unit. The primary task of the Routing unit is to differentiate the valid or invalid coincidences and generate gates to the ADC, as well as addresses in the MCA. Finally, the data will be further analyzed by reducing it to the so called ratio function ( $R(t)$ ), which will be discussed in section 3.1.3.

### 3.1.2 Probe nucleus $^{111}\text{In}$

The suitability of a probe nucleus depends on the feasibility of its preparation, the doping of the materials to be investigated, and its chemical properties. The most common PAC probe nucleus ( $^{111}\text{In}$ ) is used for all PAC measurements presented in this work. The parent nucleus  $^{111}\text{In}$  decays by the electron capture (EC) process to an excited state of the daughter nucleus  $^{111}\text{Cd}$ , which in turn decays to the ground state by emitting two  $\gamma$ -rays in succession. Figure 3.2 shows the partial decay

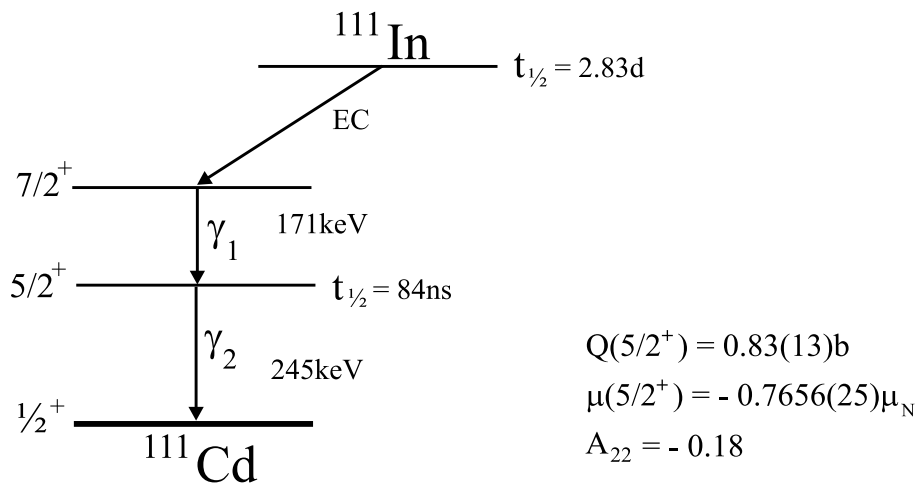


**Figure 3.2:** The partial decay scheme of  $^{111}\text{In}$ .

scheme of  $^{111}\text{In}$  that populated into  $^{111}\text{Cd}$  through the  $\gamma - \gamma$  cascade. Following

the EC decay  $\gamma_1$  is emitted with  $E_{\gamma_1} = 171$  keV and the nucleus remains in the intermediate state to a half life of  $t_{1/2} = 84$  ns before emitting  $\gamma_2$  with  $E_{\gamma_2} = 245$  keV. After the emission of the second  $\gamma$ -ray it transforms to stable daughter nucleus  $^{111}\text{Cd}$ . One of the advantages of this probe nucleus over the other is that it has

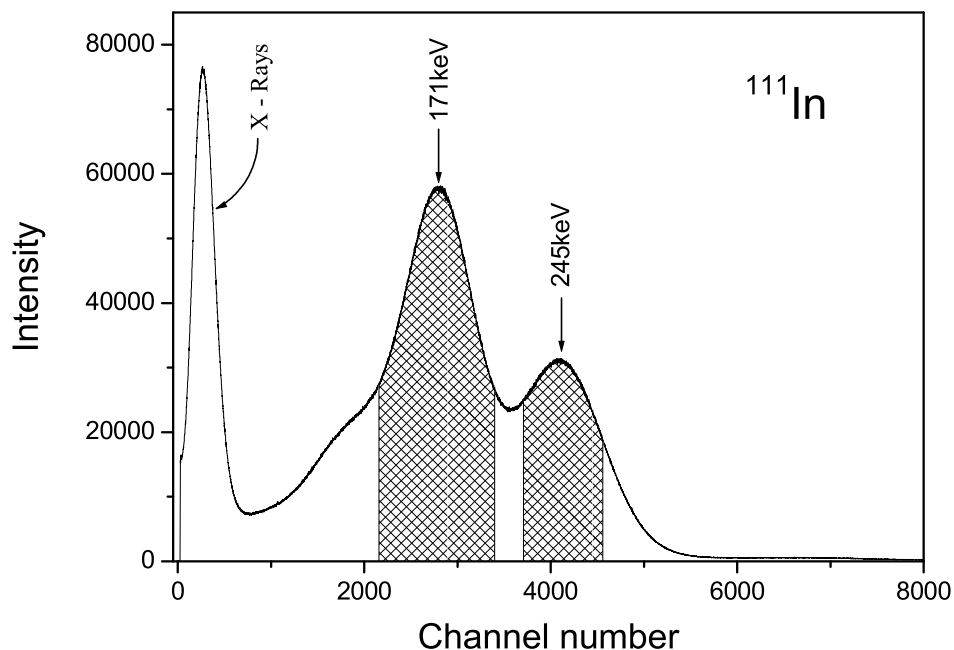


**Figure 3.3:** Energy spectrum of  $^{111}\text{In}$  measured with a  $\text{BaF}_2$  detector. The shaded areas indicate typical setting of the SCA windows.

a long intermediate half life (84 ns) which allows enough time for observation of the interaction between its intermediate spin and extranuclear fields. This half life is large compared to the time resolution of the PAC apparatus, which is less than 1ns. The values of the intermediate state's ( $5/2^+$ ) electric quadrupole moment  $Q$  and the magnetic moment  $\mu$  are also given in Figure 3.2.  $A_{22}$  is the anisotropy coefficient of the  $\gamma - \gamma$  cascade. Figure 3.3 shows a typical energy spectrum of the  $^{111}\text{In}$  radioactive source taken with a  $\text{BaF}_2$  scintillation detector. The two  $\gamma$ -rays energy peaks are clearly visible over the background counts. The shaded areas are typical energy windows settings for the SCA.

### 3.1.3 The ratio function $[R(t)]$

The objective of evaluation of the ratio function ( $R(t)$ ) is to remove the contribution of irrelevant variables and factors from the measured coincidences spectra, and to arrange the data in a form that can be easily compared with the theoretical correlation functions. A detailed discussion and comparison of the different detectors

geometries is given in the literature [AREN80].

In a four detectors PAC setup like the one used here (section 3.1.1), the coincidence count rates are measured between any two detectors situated at angles of  $\theta = 90^\circ$  and  $180^\circ$ . There are 12 spectra that can be collected from this geometry four at an angle of  $180^\circ$  and eight at  $90^\circ$ . Due to the limited memory of the MCA used here, only four  $90^\circ$  spectra are taken in the current measurements together with the other four  $180^\circ$  spectra. The PAC coincidence count rate carries information about the interaction of the probe nuclei through the perturbation function, which modulates the entire spectrum. In general, the coincidence count rate is a function of the efficiency of the detectors  $\epsilon_i$ , the solid angle  $\Omega_i$  and the activity of the source  $N_0$  given by

$$N(\theta, t) = N_0 \epsilon_1 \epsilon_2 \Omega_1 \Omega_2 \exp(-t/\tau) W(\theta, t) + C \quad (3.1)$$

where  $\tau$  is the mean life of the intermediate state of the  $\gamma - \gamma$  cascade and  $C$  is a constant that will be subtracted on the basis of accidental coincidences. Possible sources of these random coincidences are coincidence counts taken from two different nuclei. The number of random coincidences between two detectors is proportional to the square of the activity of the source [SCHA92]

$$C = \epsilon_1 \epsilon_2 \Omega_1 \Omega_2 N_0^2 \quad (3.2)$$

The time spectra taken at  $180^\circ$  and  $\theta$  are separately combined and geometrically averaged by the relation

$$\overline{N(180^\circ, t)} = \left( \prod_{i=1}^4 (N_i(180^\circ, t) - C_i) \right)^{\frac{1}{4}} \quad (3.3)$$

and

$$\overline{N(\theta, t)} = \left( \prod_{i=1}^4 (N_i(\theta, t) - C_i) \right)^{\frac{1}{4}} \quad (3.4)$$

In most cases  $\theta = 90^\circ$ , but for measurements along the  $\langle 111 \rangle$  crystal axis of a diamond lattice structure, the angle would be  $\theta = 70^\circ(110^\circ)$ .

The subtraction of the background count is adjusted by a function  $A_0 = N_0 \exp(-t/\tau)$  curve, which should lie parallel to the life time curve of the PAC data.  $A_0$  correspond to the relation

$$A_0(t) = \frac{N(180^\circ, t) + 2 \cdot N(90^\circ, t)}{3} \quad (3.5)$$

Equation 3.5 stands for the exponential component of the coincidence count rate, and is independent of the interaction frequency. Using the averaged data, the so-called ratio function ( $R(t)$ ) is formed by the expression

$$R(t) = 2 \cdot \frac{\overline{N(180^\circ, t)} - \overline{N(90^\circ, t)}}{\overline{N(180^\circ, t)} + 2 \cdot \overline{N(90^\circ, t)}} \quad (3.6)$$

Substituting equations 3.1, 3.2, 3.3 and 3.4 into 3.6, it can be seen that the efficiencies  $\epsilon_i$ , the solid angle  $\Omega_i$  of the individual detectors, and the exponential decay term will cancel exactly. For probes with an intermediate spin  $I = 5/2$  and negligible  $A_{44}$  (example  $^{111}\text{In}$ ) anisotropy coefficient, the correlation function of the polycrystalline sample, where atoms are randomly orientated, is given by [FRAU65]

$$W(\theta, t) = 1 + A_{22}G_{22}(t)P_2(\cos\theta) \quad (3.7)$$

As the values of the Legendere polynomials are  $P_2(180^\circ) = 1$  and  $P_2(90^\circ) = -1/2$ , the ratio function  $R(t)$  is well approximated by the product of the effective anisotropy coefficient and perturbation function as

$$R(t) = A_{22}^{eff} \cdot G_{22}(t) \quad \text{where } A_{22}^{eff} = Q_{22}A_{22} \quad (3.8)$$

The ( $Q_{22}$ ) is the solid angle correction factor, which will be discussed in section 3.2. By fitting the theoretical perturbation function to the experimental  $R(t)$  data, information about the transition frequencies  $\omega_n$  and the main component of the EFG ( $V_{zz}$ ), as well as its symmetry ( $\eta$ ) can be measured. For a probe nucleus whose anisotropy  $A_{44}$  term can not be neglected, the correlation function should include an additional term given by the expression

$$W(\theta, t) = 1 + A_{22} \cdot G_{22}(t)P_2(\cos\theta) + A_{44}G_{44}(t)P_4(\cos\theta) \quad (3.9)$$

However, from the time spectra taken only at angles of  $\theta = 90^\circ$  and  $180^\circ$ , it is impossible to independently verify the contribution of each term. Therefore, by combining both terms into one, the perturbation function  $G(\theta, t)$  is defined as

$$G(\theta, t) = \sum_{n=0}^3 s_n^{eff}(\theta, \eta) \cos(\omega_n t) \quad (3.10)$$

where the  $s_n^{eff}$  is given by the relation

$$s_n^{eff}(\theta, \eta) = s_{2n}(\eta)P_2(\cos\theta) + \frac{A_{44}}{A_{22}}s_{4n}(\eta)P_4(\cos\theta) \quad (3.11)$$

In general, for many applications the angular correlation function of a polycrystalline source is written as

$$W(\theta, t) = 1 + A_{22}G(\theta, t) \quad (3.12)$$

## SINGLE CRYSTAL

In a single crystal PAC measurement, the detectors can be aligned towards one of the major crystal axes. In a diamond crystal like the structure of silicon and germanium, the detectors can be positioned on one of the axes  $\langle 100 \rangle$ ,  $\langle 110 \rangle$  or  $\langle 111 \rangle$ . The collected coincidence time spectra are treated in the same way as

polycrystals. Hence, based on the discussion in chapter 2, the correlation function of the single crystal source is also defined analog to equation 3.12 as

$$W(\vec{k}_1, \vec{k}_2, t) = 1 + A_{22}G(\theta_1, \varphi_1, \theta_2, \varphi_2, \theta, \eta, t) \quad (3.13)$$

The definition of  $\theta_i$  and  $\varphi_i$  are the same as in Figure 2.4, and  $\theta$  is the angle between the detectors. Similarly, the perturbation function takes the form [WEGN85]

$$G(\theta, t) = \sum_{n=0}^3 s_n^{eff}(\theta_1, \varphi_1, \theta_2, \varphi_2, \theta, \eta) \cos(g(\eta)\omega_0 \cdot t) \quad (3.14)$$

According to this definition of  $G(\theta, t)$ ,  $\omega_0$  is identical to  $\omega_Q$  in equation 2.24. In an effort to simplify the theoretical ratio function, D. Wegner [WEGN85] has introduced the following definition for  $s_n^{eff}$  coefficients in the general correlation function, where the  $s_n^{eff}$  depend not only on the angle between detectors, but also the direction of the emission of the  $\gamma$  quanta in the principal axis system. Here, the  $s_n^{eff}$  are

$$s_n^{eff}(\theta_1, \varphi_1, \theta_2, \varphi_2, \theta, \eta) = s_{2n}^{eff} + \left( \frac{A_4^{eff}(2)}{A_2^{eff}(2)} \right) s_{4n}^{eff} \quad (n = 0, 2, 4) \quad (3.15)$$

where each of the  $s_{kn}^{eff}$  coefficients is an average value over all equivalent crystal orientations of the EFG according to the relation

$$s_{kn}^{eff} = \frac{1}{p} \sum_{i=1}^p s_{kn}(h_i k_i l_i) \quad (k = 2, 4) \quad (3.16)$$

where  $h_i k_i l_i$  are the Miller indices of  $p$  equivalent crystallographic directions. According to the definition (equ. 3.15), the ratio  $(A_4^{eff}(2)/A_2^{eff}(2))$  involves only the coefficients for the second gamma transition ( $\gamma_2$ ). The  $s_{kn}$  are obtained by appropriate reduction of equation 2.61.

Moreover, the ratio function is formed exactly the same way using equation 3.6. Hence, the theoretical fit function is simplified as follows

$$R(t)_{theory} = 2 \cdot \frac{W(180^\circ, t) - W(\theta, t)}{W(180^\circ, t) + 2W(\theta, t)} \quad (3.17)$$

$$= 2 \cdot \frac{A_{22}[G(180^\circ, t) - G(\theta, t)]}{3 + A_{22}[G(180^\circ, t) + 2G(\theta, t)]} \quad (3.18)$$

$$\approx \frac{2}{3} \cdot A_{22}^{eff} [G(180^\circ, t) - G(\theta, t)] \quad (3.19)$$

The coefficient  $2/3$  has no contribution to the perturbation function since it only shifts the value of the anisotropy. Therefore, with less than 1% relative error, the perturbation function is approximated as

$$\tilde{G}(t) = \frac{2}{3} \cdot [G(180^\circ, t) - G(\theta, t)] \quad (3.20)$$

or

$$\tilde{G}(t) = \frac{2}{3} \cdot \sum_{n=0}^3 [s_n^{eff}(180^\circ) - s_n^{eff}(\theta)] \cos(g(\eta)\omega_0 \cdot t) \quad (3.21)$$

The  $s_n^{eff}$  coefficients contain all information about the orientation of the EFG in the crystal relative to the position of the detectors. A similar definition of  $s_n^{eff}$  was also used by U. Pütz (see Appendix C). For  $90^\circ$  and  $180^\circ$  detector arrangements, the  $s_n^{eff}$  coefficients are written as

$$s_n^{eff}(180^\circ) - s_n^{eff}(\theta) = s_n^{eff}(180^\circ) - s_n^{eff}(90^\circ) \quad (3.22)$$

This method requires the evaluation of  $s_n^{eff}(\theta)$  for coincidences measured at angles of  $90^\circ$  and  $180^\circ$ . Finally, the perturbation function would be

$$R(t) = A_{22}^{eff} \cdot \tilde{G}(t) \quad (3.23)$$

## MULTIPLE PERTURBATIONS

Often, the probe nuclei in the host material reside in different but unique lattice environments, leading to the observation of more than one interaction frequency. If there are several interaction frequencies in the sample with distinct fractional populations  $f_i$  of the probe nuclei, the total perturbation function is the sum over all perturbation functions of the various interactions existed, i.e.

$$G(t) = \sum_i f_i G_i(t) \quad \sum_i f_i = 1 \quad (3.24)$$

where the summation index  $i$  refers to the different environments of the probe. The perturbation function of a given interaction is then written as follows in line with the definition of equation 3.14 for a single crystal.

$$G_i(t) = \sum_{n=0}^3 s_n^{eff} \cos(g(\eta)\omega_0^i \cdot t) \quad (3.25)$$

In PAC, measurements of the interaction frequencies in most cases lead to statistical distributions around a mean value. Such a frequency distribution is the result of inhomogeneous lattice structure near the probes of the same environment causing slight variations in the EFG. This frequency distribution can be described by either a normal Gaussian or Lorentzian distribution function. Using a Lorentzian distribution, the perturbation function for a static electric interaction is given by

$$G_i(t) = \sum_{n=0}^3 s_n^{eff} \cos(g(\eta)\omega_0^i \cdot t) \cdot \exp[-(g(\eta)\omega_0^i \cdot \delta^i \cdot t)] \quad (3.26)$$

The exponential factor  $\delta^i$  measures the width of the frequency distribution at FWHM centered around the mean value. The PAC spectrum may not only be affected by the static frequency damping  $\delta^i$ , but also by dynamic processes that may

take place near the probe at the time of the measurement, resulting in dynamic damping  $\lambda^i$ . The effect of the two types of frequency damping may be combined in the form

$$G_i(t) = \sum_{n=0}^3 s_n^{eff} \cos(g(\eta)\omega_n^i \cdot t) \cdot \exp[-(g(\eta)\omega_0^i \cdot \delta^i + \lambda^i) \cdot t] \quad (3.27)$$

When no dynamic process exists in the interaction, the parameter  $\lambda^i$  will be kept to zero and equation 3.27 will reduce to the form 3.26. The same holds true in the absence of static damping [SKUD92].

### TYPICAL EXAMPLES

There are typical situations that often occur in PAC time spectra. Only one or a combination of the many interactions may exist simultaneously in a given measurement. In order to simplify matters, consider a static electric interaction which can be described by equation 3.26.

1) When a fractional population is subject to undamped and axially symmetric interaction (i.e.  $\eta = 0$  and  $\delta_1 = 0$ ), the perturbation function is given by

$$G_1(t) = \sum_{n=0}^3 s_n^{eff} \cos(n\omega_1 \cdot t) \quad (3.28)$$

2) Another fraction of the probe atoms may also be subject to a damped unique interaction frequency as described by

$$G_2(t) = \sum_{n=0}^3 s_n^{eff} \cos(g(\eta)\omega_0 \cdot t) \cdot \exp(-g(\eta)\omega_0 \cdot \delta_2 \cdot t) \quad (3.29)$$

3) There are also cases where the EFG is weak and not unique. In such cases the perturbation function is written as [PUTZ82]

$$G_3(t) = \sum_{n=0}^3 s_n^{eff} \exp[-n\delta_3 \cdot t] \quad (3.30)$$

4) A fraction of probe nuclei may take sites with extremely high EFG, which can not be resolved by the present electronics. Such a fractional population takes 1/5 of the total anisotropy. The corresponding perturbation is

$$G_4(t) = 1/5 \quad (3.31)$$

5) Probe nuclei at lattice sites where there exists symmetric charge distribution experience zero EFG. This fraction of probe atoms contribute a constant value to the total perturbation function.

$$G_5(t) = 1 \quad (3.32)$$



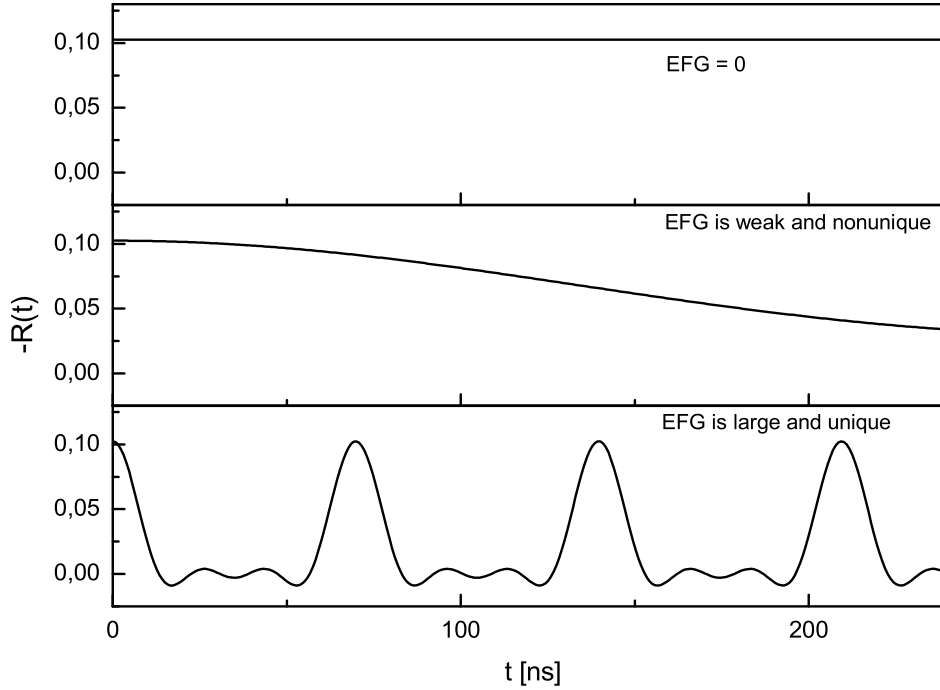


**Figure 3.4:** Typical pattern of the PAC time spectra for probe atoms at different environments.

If the amplitude of modulation is equal to the value of the anisotropic coefficient  $A_{22}$  (example:  $^{111}\text{In}$ ), it then corresponds to 100% of the probe atoms in an undisturbed environment (see top panel Figure 3.4).

The experimental  $R(t)$  values are fitted with the program NFit [BARR92], which has several possibilities to fit PAC data of the electric, magnetic or both interactions at the same time during the process. The program calculates

$$R(t) = 2 \cdot \frac{W(180^\circ, t) - W(\theta, t)}{W(180^\circ, t) + 2W(\theta, t)} + C \quad (3.33)$$

An additive constant  $C$  allows for the minor shift of  $R(t)$ , compensating for the error caused by any off-central positioning of the samples or self absorption of the  $\gamma$ -rays in the sample. The calculated ratio function is compared to the experimental one. The standard least squares minimization routines are used to obtain the best fit to the data. Initial estimates of  $\omega_i^i$ ,  $\delta^i$  and  $\eta^i$  for all fractions are required by the program. These estimates can be obtained from Fourier transformation of the  $R(t)$  data.

## 3.2 Solid angle correction for anisotropy coefficient

The correlation function discussed in the last chapter is based on the assumption of a point like source. In real measurements the sources and detectors are generally different from a point-like shape. Therefore, the measured anisotropy coefficient needs geometrical correction. The form of the correlation function (equation 2.36) necessary to describe the result of angular correlation measurements is unchanged by this correction, but the coefficient of each term becomes multiplied by an attenuation factor. Generally, calculations of the geometrical correction factor are difficult, but for cylindrically symmetric detectors simple expressions are derived by [YATE65] for the attenuation factor.

Therefore, the finite detector size corrections are made by correcting the theoretical anisotropy coefficient  $A_{kk}$ . If the size of the source can be neglected, then the experimental (effective) anisotropy coefficient can be written as

$$A_{kk}^{eff} = Q_{kk} A_{kk} \quad (3.34)$$

where each factor is given by

$$A_{kk} = A_k(\gamma_1) A_k(\gamma_2) \quad (3.35)$$

$$Q_{kk} = Q_k(\gamma_1) Q_k(\gamma_2) \quad (3.36)$$

where the  $Q_{kk}$  coefficients are the solid angle correction factor. For cylindrically symmetric detectors, the  $Q_{kk}$  is the product of the correction factors for each detector involved in the measurement of  $\gamma_1$  and  $\gamma_2$ . Therefore, the attenuation factor is defined as

$$Q_k(\gamma_i) = \frac{J_k(\gamma_i)}{J_0(\gamma_i)} \quad \text{where } i = 1, 2 \quad (3.37)$$

the function  $J_k$  ( $k = 0, 2, 4 \dots$ ) is given by

$$J_k = \int_0^\varphi P_k(\cos\beta) (\epsilon(\beta)) \sin\beta d\beta \quad (3.38)$$

where  $P_k(\cos\beta)$  are Legendre polynomial function, and  $\epsilon(\beta)$  is the angle dependent efficiency of the detectors. The  $\beta$  runs from zero to half of the maximum solid angle subtended by the detector (see Figure 3.5). For the  $\gamma - \gamma$  cascade of  $^{111}\text{In}/^{111}\text{Cd}$ , the  $A_k(i)$  values are  $A_2(\gamma_1) = 0.3299$ ,  $A_2(\gamma_2) = -0.5345$ ,  $A_4(\gamma_1) = 0.0023$  and  $A_4(\gamma_2) = -0.6172$  [WEGN85]. Therefore, geometrically corrected anisotropy coefficients can be calculated using the values from Table 3.1 and equations 3.35, 3.36 and 3.37. Since the efficiency  $\epsilon(\beta)$  is not constant in equation 3.38 due to the extended size

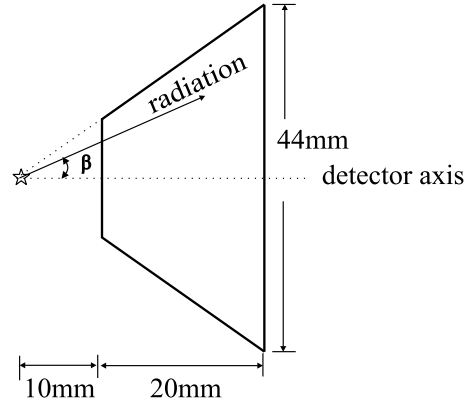


**Figure 3.5:** Two dimensional view of the cone like geometry of the  $BaF_2$  detector.

E[keV]	d	1cm	1.5cm	2cm	2.5cm	3.0cm
173	Q <sub>2</sub>	.72483(95)	.81315(56)	.85960(53)	.88779(39)	.90910(31)
( $\gamma_1$ )	Q <sub>4</sub>	.2750(24)	.4691(18)	.5861(18)	.6615(13)	.7216(10)
243	Q <sub>2</sub>	.72232(92)	.8167(59)	.86651(56)	.89522(52)	.91639(43)
	Q <sub>4</sub>	.2693(25)	.4762(18)	.6041(18)	.6821(18)	.7420(14)
248	Q <sub>2</sub>	.72214(89)	.81675(64)	.8665(54)	.89501(49)	.91506(42)
( $\gamma_2$ )	Q <sub>4</sub>	.2674(24)	.4765(19)	.6039(18)	.6818(16)	.7374(14)

**Table 3.1:** Results of the Monte-Carlo simulation calculation of the absorption coefficient for varies  $\gamma$ -energies for different source-detector distance [MARX95].

of the detector used (Figure 3.5), hence, the  $Q_k$  values in Table 3.1 are evaluated by numerical methods using the so called Monte Carlo calculation. The anisotropy coefficient  $A_{22}^{eff}$  for  $^{111}\text{In}$  was also measured experimentally on the 4-detector PAC setup. The source was prepared by  $\alpha$ -irradiation of 0.1 mm thick silver target with (33 MeV, 20 min), from the reaction  $^{109}\text{Ag}(\alpha, 2n)^{111}\text{In}$  the desired indium isotope is produced. After irradiation the source was cut to the shape similar to a point source, then, it was annealed at 500°C for 120 s. At the chosen annealing temperature all  $^{111}\text{In}$  so produced occupy lattice site where there exists a symmetric charge distribution and hence experience no EFG. The silver target used was not crystal, hence, the source is regarded as polycrystalline source where atoms are randomly oriented. Therefore, one determines experimentally the  $A_{22}^{eff}$  term of the anisotropy coefficients, which can also be used to calculate the remaining components [WEGN85].

d[cm]	1cm	1.5cm	2cm	2.5cm	3.0cm
A <sub>22</sub>	-0.0942(2)	-0.1195(2)	-0.1341(2)	-0.1430(1)	-0.1497(1)
A <sub>24</sub>	-0.0395(4)	-0.0790(4)	-0.1059(4)	-0.1235(3)	-0.1368(3)

**Table 3.2:** Geometrically corrected anisotropy coefficient of  $^{111}\text{In}/^{111}\text{Cd}$   $\gamma - \gamma$  cascade

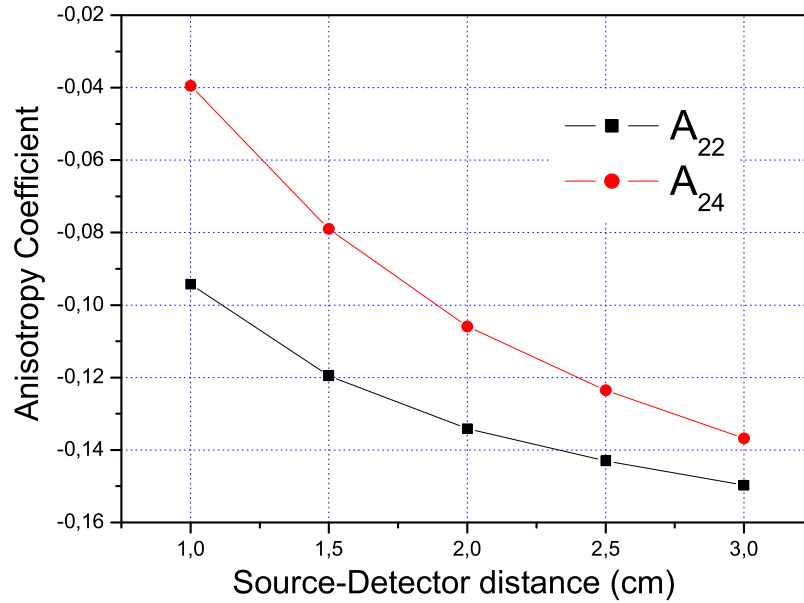


**Figure 3.6:** Geometrically corrected anisotropy coefficients using Monte-Carlo simulation for  $\gamma - \gamma$  transition in  $^{111}\text{In}$

d[cm]	1.1cm	1.6cm	2.1cm	2.6cm	3.1cm
$A_{22}$	-0.0948(3)	-0.1175(2)	-0.1300(3)	-0.1369(2)	-0.1389(5)

**Table 3.3:** Measured anisotropy coefficient of  $^{111}\text{In}/^{111}\text{Cd}$   $\gamma - \gamma$  cascade

By extrapolating the measured anisotropy to 1.0 cm source-detector distance, it is found that  $A_{22}^{eff} = -0.0906(4)$ . This value deviates by 3.8% from the calculated in Table 3.2. The deviation most probably due to the error during locating the source to the geometrical center of the detectors and, the source extended size compared to an ideal point source.

## 3.3 Ion implantation

### 3.3.1 The ion implanter

Ion implantation is a convenient method for altering the near surface properties of materials. It uses the acceleration of ions in well defined energy towards the surface of a material. Ion implantation is a mature and very versatile technique. Therefore, this section is intended to give only an overview of the basic principles of the ion implanter and discuss the expected radiation damage caused by ion implantation.

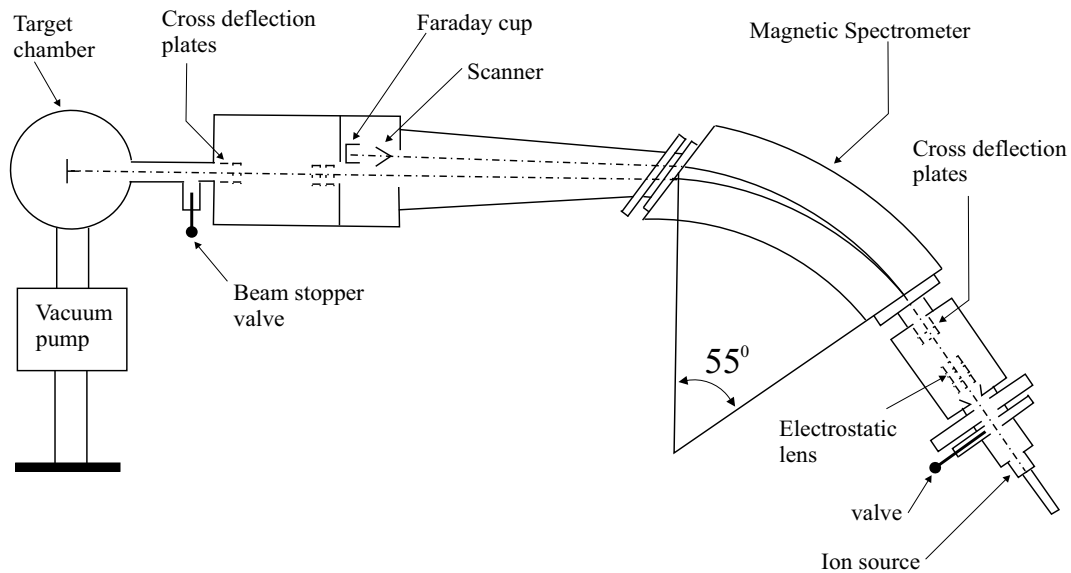


**Figure 3.7:** Schematic diagram of the Bonn mass separator showing the main components of the accelerator system

The most basic components of ion accelerator are the ion source, the beam analysis, the beam manipulation and target assembly. The ultimate performance of any experimental ion-beam facility is largely a measure of the successful matching of the various components. It is possible to arrange the different elements of the accelerator in a variety of ways. Figure 3.7 shows the schematic diagram of the Bonn ion implanter. It served as a conventional form of accelerator up to beam energy 80 keV, whose ion source is at high voltage whereas the analyzer and the target chamber are at ground potential. The advantage of such a system is that the source and the power supplies are electrically and physically isolated from the rest of the system, hence, there is unrestricted access to the target chamber. This facility has also an additional working mode for accelerating ions above 80 keV, by applying high voltage in the region of the target chamber. In this case there is no access to the target during the implantation.

**ION SOURCE:** The main purpose of the ion source is to generate ions which can be transported to the target as ion beam. The most common method of creating ions is by subjecting the vapor of the element to be ionized, or a compound of it, to impact by energetic electrons. These are normally supplied from a heated filament and at the pressures used a plasma containing ions and electrons will be formed. From the boundary of this conducting, space-charge neutralized zone ions will have to be extracted by an appropriate electric field. There are different kinds of ion source. Figure 3.8 shows the design due to Freeman, sometimes known as the Harwell ion source, in which an oven supplies vapor to the cylindrical arc chamber. This source provides an exceptionally stable plasma, and for this reason a very high quality beam for isotope separation and precise ion implantation work.

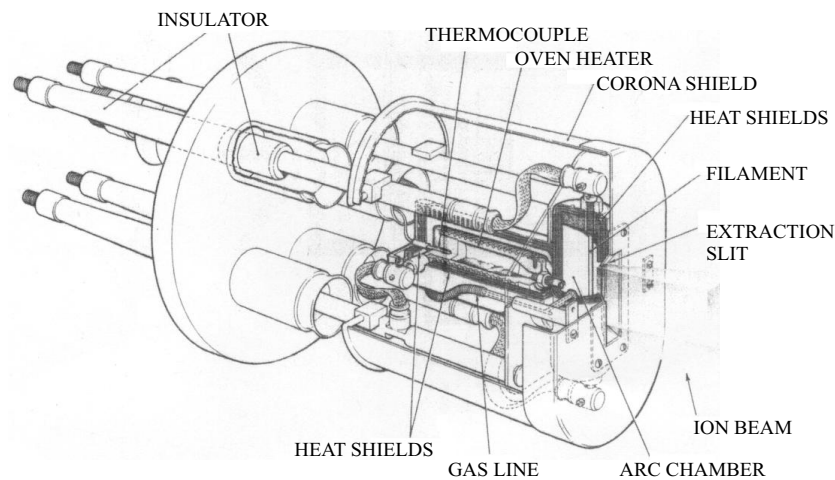


**Figure 3.8:** Schematic diagram of the Freeman type ion source [THOM78]

The first stage in the injection of ions into the acceleration system involves their extraction from the plasma in which they are created. The surface ionization source differs in that the ions are released from a well-defined surface, but a plasma will take up a configuration which is affected by the flux of ions from the plasma boundary. Figure 3.9 shows some of the processes that could occur at plasma boundary. The

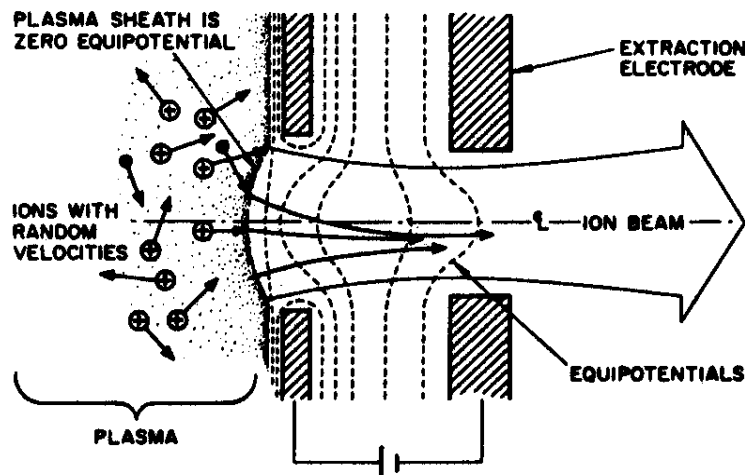


**Figure 3.9:** Example of ion extraction from a plasma [WILS73]

behavior under increasing value of ion acceleration potential that a curvature or “meniscus” is created in the plasma boundary. Since ions are extracted normal to this surface one may have a virtual focus from which ions appear to emerge. It is clear that an unstable plasma boundary causes a severe aberration. Often the extracted beam is composed of different impurity species and isotopes of the different elements. The next stage in the implanter system is usually to perform mass discrimination of the extracted ions, which normally takes place in a magnetic

spectrometer, and accelerate the desired element towards the target.

### IMPLANTATION OF THE PROBE ATOM( $^{111}\text{In}$ )

The radioactive probe nuclei are obtained from commercially available sources as diluted  $^{111}\text{InCl}_3$ . During preparation the liquid  $^{111}\text{InCl}_3$  is mixed with small amount of natural  $\text{InCl}_3$  powder in the oven of the ion source in order to get a stable plasma. The mixture will then be exposed to heat in order to evaporate the water and allow  $^{111}\text{In}$  to diffuse to the mixture. Then after the oven will be mounted in the ion source and to the accelerator system. The ionized indium atoms are extracted from ion source and first accelerated by 80 keV and then ions are selected according to their mass in the  $55^\circ$  bended magnetic spectrometer. The selected isotope is again accelerated by another 80 keV to attain the implantation energy of 160 keV.

For some of the implantations carried out here, the isotope  $^{111}\text{In}$  is produced in Bonn Cyclotron facility by  $\alpha$ -irradiation (Energy = 33 MeV, 80 hrs) using an Ag-target. The stable donor atoms are obtained commercially in a powder from with very high purity.

Samples	Stable isotopes			$^{111}\text{In}$	
	Ion	Energy(keV)	Dose(ions/cm <sup>2</sup> )	Energy(keV)	Dose(ions/cm <sup>2</sup> )
Smp-Nr4	$^{75}\text{As}$	120	$4 \times 10^{14}$	160	$6.1 \times 10^{12}$
Smp-Nr7	$^{75}\text{As}$	120	$5 \times 10^{14}$	160	$< 10^{13}$
Smp-B3	$^{121}\text{Sb}$	80	$2 \times 10^{14}$	80	$7.6 \times 10^{12}$
Smp-B4	$^{123}\text{Sb}$	120	$5 \times 10^{14}$	160	$< 10^{13}$
Smp-C1	$^{31}\text{P}$	60	$1.6 \times 10^{14}$	160	$6 \times 10^{12}$
Smp-C3	$^{31}\text{P}$	60	$1.6 \times 10^{14}$	160	$8 \times 10^{12}$
Smp-d6	$^{80}\text{Se}$	120	$0.5 \times 10^{15}$	160	$5.8 \times 10^{12}$
Smp-4	$^{128}\text{Te}$	50	$2 \times 10^{15}$	160	$< 10^{13}$
Smp-8	$^{130}\text{Te}$	50	$2.5 \times 10^{15}$	160	$< 10^{13}$
<b>Germanium</b>					
Smp-a7	$^{12}\text{C}$	30	$4.5 \times 10^{15}$	160	$3.7 \times 10^{12}$
Smp-a13	$^{12}\text{C}$	40	$2.5 \times 10^{15}$	160	$2.4 \times 10^{12}$

**Table 3.4:** *Ion implantation data*

**RADIATION DAMAGE:** When ions penetrate into a crystalline solid, it undergoes a number of collisions with the target atoms. In these collisions, sufficient energy may be transferred from the ion to the target atom causing it to leave its lattice location. Energetic displaced atoms can in turn displace other atoms and so on, thus creating a cascade of atomic collisions. This leads to a distribution of vacancies, interstitial atoms and other types of lattice disorder in the region around the ion track. As the number of ions incident on the crystal increases, the individual disordered regions begin to overlap. At some point an amorphous layer is formed, mostly in materials like insulator and semiconductor. In metals, the defects are quickly annealed by the temperature created during implantation. The total

amount of disorder and distribution in depth depends on ion species, temperature, energy, total dose and channelling effects. Dispersed microcrystallized phases or precipitates can also be formed depending on the nature of the material and on the experimental conditions. In general, the target material undergoes a physical, chemical or electrical change. For instance, the creation of numerous defects associated with the presence of new chemical phases leads often to the formation of stresses (generally compressive stress). They notably influence the mechanical properties of the implanted layers. Most of the defects can be annealed as a consequence of rise on sample temperature during implantation, which allows movement and interactions of defects. The rest of the defects can be removed by thermal treatment after implantation. Some possible defect interactions are shown schematically in Figure 3.10. Most of the samples in this work are annealed by rapid thermal annealing

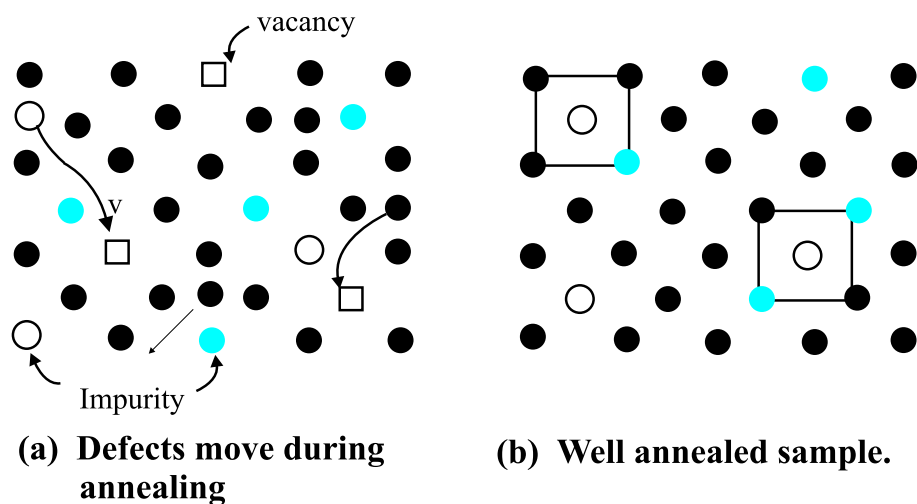


**Figure 3.10:** Two dimensional schematic representation of a disordered atomic arrangement caused by ion implantation(a) and recrystallization after annealing(b).

(RTA) in vacuum, which allows vacuum quenching of equilibrium concentration of defects at each annealing temperatures. The recovery of the radiation damage can be studied in several ways. The following section presents two examples of recovery of damage after  $^{111}\text{In}$  implantation in Si and Ge crystal targets using the perturbed angular correlation method.

### 3.3.2 Recovery of damage after $^{111}\text{In}$ implantation

In section 3.1.2, the properties of the probe atom ( $^{111}\text{In}$ ) commonly used in perturbed  $\gamma - \gamma$  angular correlation method are discussed. By implanting this radioactive probe atom into the samples, substantial amount of unavoidable contamination of other isotopes will be incorporated creating more damage than expected. According to U. Pütz [PUTZ82] in a typical  $^{111}\text{In}$  implantation of dose between  $10^{13}$



and  $10^{14}$  atoms/cm<sup>2</sup> only (5-6)% shall be the desired isotope, the rest are different isotopes of indium and stable  $^{111}\text{Cd}$ . By reducing the dose, it is possible to reach a tolerable damage limit, which can be removed by keeping the sample at high temperature for a period of time. The dose typically chosen for PAC measurements ranges between ( $10^{12}$  -  $10^{13}$ ) atoms/cm<sup>2</sup> of which a dose of the order of  $10^{11}$  atoms/cm<sup>2</sup> is expected to be  $^{111}\text{In}$ . The following are examples of tolerable dose of indium implantation in silicon and germanium. Discussions are also given on the associated recovery of damage by heat treatment.

### 3.3.2.1 Silicon

A  $5 \times 6 \text{ mm}^2$  size of silicon crystal with  $\langle 110 \rangle$  surface was implanted with indium (Dose of  $2.4 \times 10^{12}$  atoms/cm<sup>2</sup> and Energy = 160 keV). The PAC time spectrum

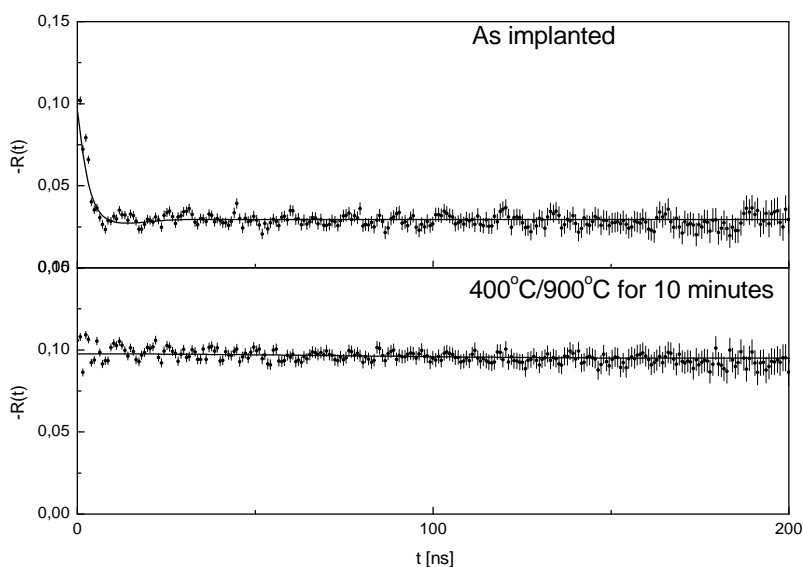


**Figure 3.11:** PAC time spectra from indium implanted silicon sample showing an increase in anisotropy by annealing the sample. The solid line is fit of the appropriate perturbation function.

taken right after implantation was fitted according to equation 3.8 (Figure 3.11). The fit result showed 85(3)% of the probe atoms possess a highly disturbed lattice environment, while the remaining 15(3)% are still on undisturbed substitutional lattice site. This indicates that the silicon sample was not completely amorphised by the indium implantation. The sample was then annealed at 400°C and 900°C for 600s successively. The measured anisotropy coefficient after annealing was  $A_{22}^{eff} = -0.0965(2)$ , which differs by 3.5% from the calculated anisotropy coefficient (Figure

3.6). This may be due to an extended size of the source and deviation of the sample from the geometrical center of the detectors. Such close value of the measured anisotropy coefficient suggest that almost all indium takes substitutional lattice sites after the heat treatment. After fitting the data, about 97(3)% of the implanted indium is found in an undisturbed lattice environment. The remaining fraction of 3(2)% accounts for probe atoms at imperfect cubic lattice site experiencing non-unique and very small EFGs. This may be caused by far sited defect whose presence in the vicinity of the probe disturbs the cubic symmetry of the substitutional indium.

### 3.3.2.2 Germanium

Indium was implanted with a dose of  $2.4 \times 10^{12}$  atoms/cm<sup>2</sup> and an energy of 160 keV in a sample which was prepared from a  $\langle 100 \rangle$  germanium wafer. Because of the low melting point of germanium compared to silicon, the recovery of the radiation damage takes place at a much lower annealing temperature. Annealing

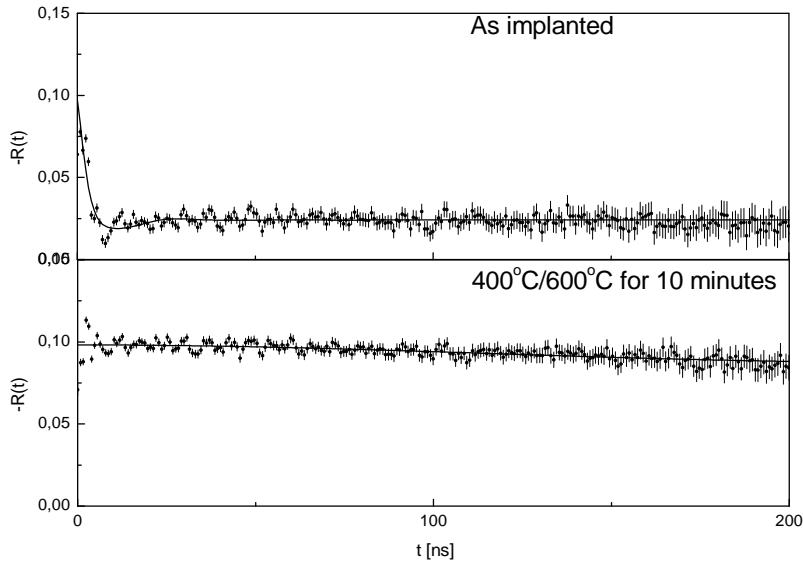


**Figure 3.12:** PAC time spectra from indium implanted Germanium sample

the germanium sample at 400°C and 600°C for 600s successively showed  $A_{22}^{eff} = -0.0955(6)$ . Like in the case of silicon, this value deviates by a similar percentage from the calculated anisotropy coefficient. The fit to the time spectrum showed, right after implantation nearly 89(2)% of the probe atoms in disturbed environments while the remaining 11(2)% are on substitutional lattice sites. After annealing the sample the substitutional fraction grows to 96(2)%. In general, annealing both Si and Ge samples after indium implantation showed a sharp rise in the value of

$^{111}\text{In}$ implantation in		$\nu_Q$ [MHz]	$f_p$ [%]	$f_s$ [%]	$\eta$	$\delta$ [%]	$A_{22}$
Silicon	as implanted	158(1)	85(3)	15(3)	0.0	71(8)	0.10
	annealed	0.0(1)	–	97(3)	–	0.0	0.10
Germanium	as implanted	215(8)	89(2)	11(2)	0.34(1)	76(6)	0.10
	annealed	0.0	–	96(2)	–	0.00	0.10

**Table 3.5:** *Fit results of indium implanted silicon and germanium samples*

anisotropy coefficients (see Figure 3.11 and 3.12). These indicate the existence of no observable interaction frequency at the site of the probe nuclei. This is only possible when the probe atoms possess substitutional lattice site in the diamond lattice surrounded by the host atoms. Such a lattice position in Si and Ge diamond structure has a cubic symmetry leading to zero electric field gradient at the probe sites.

Comparing germanium and silicon directly after implantation show that germanium has sustained higher implantation damage than silicon, despite the fact that the same energy and comparable dose are used. This can be seen by the various substitutional fraction of  $^{111}\text{In}$  (Table 3.5) after implantation, and the corresponding difference in the lower limit (see Figure 3.11 and 3.12) of the time spectra.

# Chapter 4

## INDIUM IMPURITY PAIRS in Si and Ge.

### 4.1 Introduction

The passivation of electrically active centers is a common problem in semiconductors. It has been studied in the past using electrical measurements at p-n junctions, infrared spectroscopy, EPR and other methods [PEAR87, THEW85]. The deactivation of these centers in silicon and germanium can be a result of the presence of a different kind of impurity atoms, which sometimes create undesired effects on the properties of the materials. Most foreign impurity atoms are incorporated into semiconductors by implantation, diffusion or undesirably during material processing. The structural site of such deliberately incorporated impurity atoms have been successfully studied using Rutherford back scattering (RBS), ion Channelling, and perturbed angular correlation (PAC) methods. Infrared absorption, based on the local vibrational modes, is able to produce important evidence to the existence of unfamiliar bonding between different solute atoms in the host lattice. A nuclear method such as perturbed angular correlation technique has the ability to detect the microscopic environment around the probe nucleus through the measured electric field gradient (EFG). The existence and structure of the different ion pairs in silicon have been clearly demonstrated by the combined results from PAC and RBS experiments [WICH89]. In these measurements agreement has been reached that group III-V compensation in semiconductor is due to localized atomic bonding rather than the carrier recombination in the band model.

The mechanism of impurity pairs formation is either columbic attraction of oppositely charged solute atoms or the difference in atomic size of the elements involved. In order to study indium-donor pairs under the influence of uniaxial stress, it was necessary first to carry out test measurements on their thermal stability. Under this objective new measurements have been taken at different annealing temperatures

for group V donors (section 4.3). Besides, results and discussion will be given in section 4.4 and 4.5 on the new pairs found in silicon and germanium using group VI donors and carbon respectively.

## 4.2 Formation and thermal stability of Indium-Donor pairs in silicon

There are two subsections which are intended to serve two different purposes. In section 4.3 the In-group V pairs are discussed briefly, together with new measurements whose results are compared to the data published by Wichert and et al. [WICH86] [WICH89]. In this section, the measurements are intended to reproduce the results in our system, and extract information about the temperature at which maximum fractional population of pairs can be attained by annealing the samples in vacuum ( $\sim 10^{-5}$ mbar). These information are used later in Chapter 5 for the interpretation of the measurements of pairs under uniaxial stress. In a phosphorous implanted sample the reversibility of the In-P pair has been tested, which to my knowledge has not been reported in any previous work. Section 4.4 is devoted to the new results and discussions of the In-group VI pair in silicon.

## 4.3 Indium-group V donor pairs

### 4.3.1 In-P pair

The silicon sample was implanted with phosphorous (Energy = 60 keV; dose =  $4 \times 10^{14}$  ions/cm<sup>2</sup>) at room temperature. The implantation profile was selected in such a way that it would overlap with the indium profile. The sample was annealed in an isochronal annealing program that uses 600 s holding time at each annealing steps. After annealing the sample at 600°C already a small fraction of the indium phosphorous pair was observed. Which can be seen in the first panel of Figure 4.1 by the small amplitude of modulation of the PAC time spectrum. The same spectrum shows a slowly varying frequency as the result of imperfect substitutional lattice sites of the probe atoms indicating an incomplete recovery of the radiation damage. At 627°C, a well defined interaction frequency of the In-P pair is observed whose quadrupole coupling constant is  $\nu_Q = 179(1)$  MHz ( $\eta = 0$ ). Depending on the symmetry of the measured EFG and the dose dependence of the fraction, this frequency was assigned to substitutional In-P pair. In this sample only one frequency is observed because phosphorous was incorporated by implantation. According to results of [WICH89] more phosphorous cluster can be observed when phosphorous is doped during crystal growth. The fraction  $f_1$  (see equ. 3.24) of the pair increases

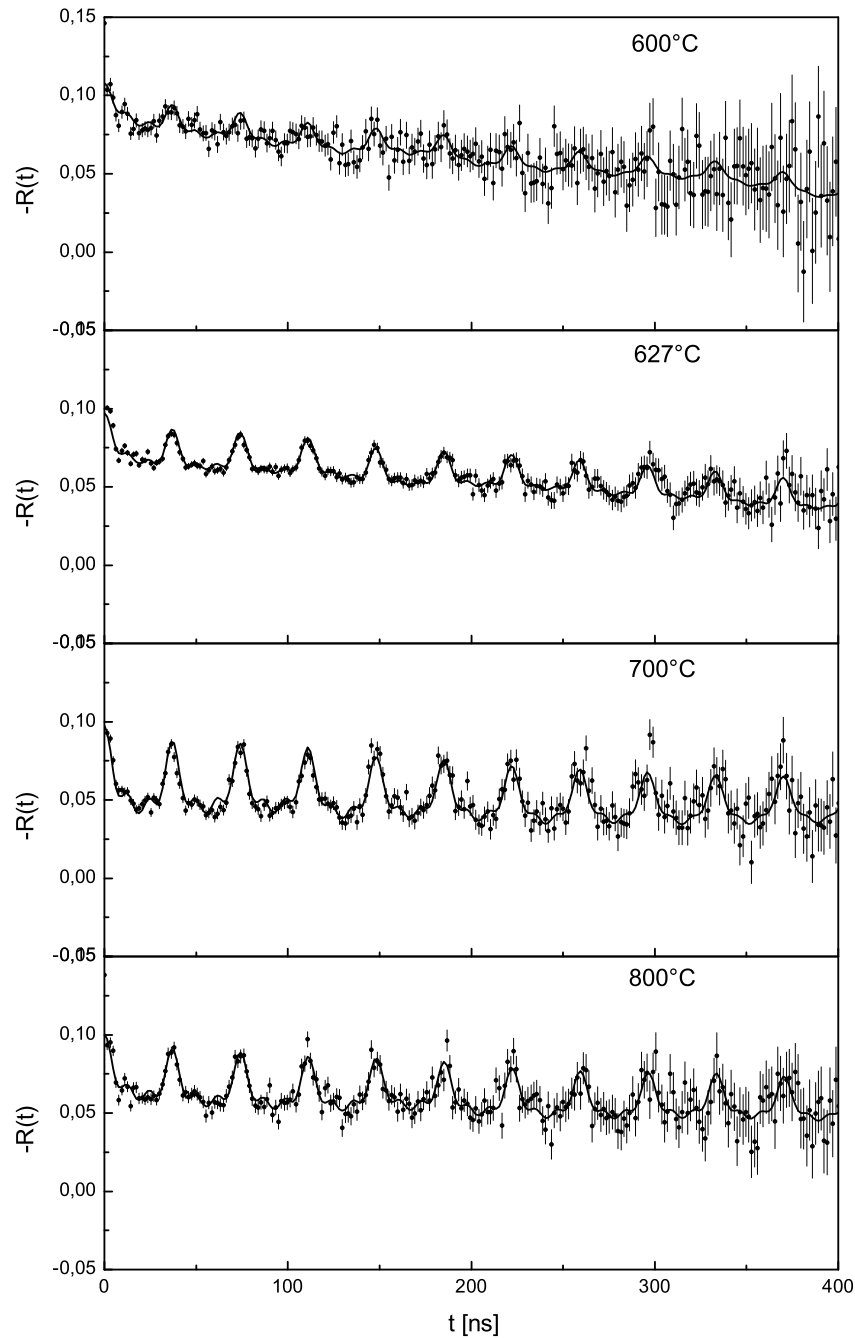


**Figure 4.1:** PAC time spectra modulated by interaction frequency of In-P pair in silicon. The solid line is the theoretical fit according to equation 3.23, measurements are taken along  $\langle 100 \rangle$  crystal axis.

at higher temperatures, which is clearly seen by the growth of the amplitudes of modulation in the time spectra. A maximum fraction of 31(3)% was measured at 700°C. The fraction of the pairs decreases after annealing the sample at 800°C and then the frequency eventually disappears above 1000°C.

Figure 4.2 shows the fractional population of probe nuclei in different lattice environments. The population of the In-P pair grows monotonically up to 700°C

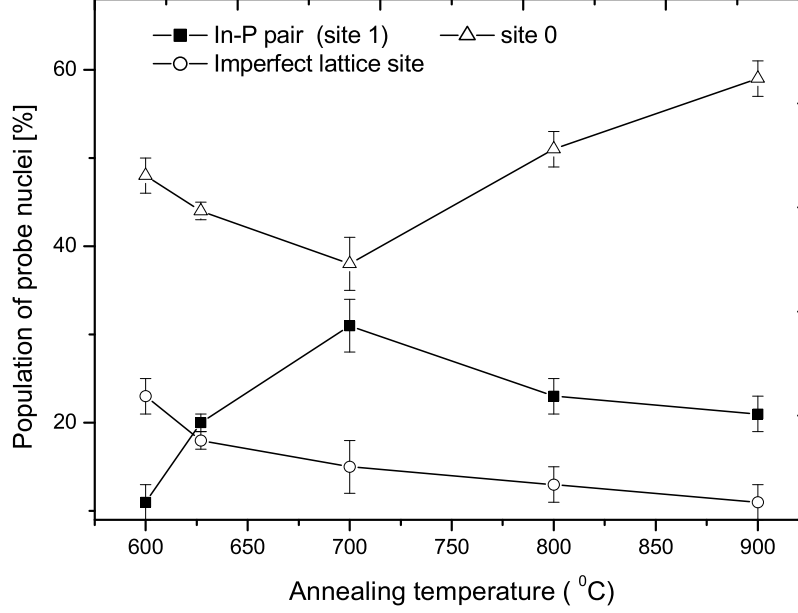


**Figure 4.2:** *The fractional population of indium at different environments.*

and then decreases at high temperatures, whereas, the fractional population of the tetrahedrally symmetric substitutional site of indium grows to nearly 59(2)% at 900°C at the expense of the dissociation of the In-P pair. The best fit to the data

Different complexes	Annealing temperature				
	600°C	627°C	700°C	800°C	900°C
$\nu_{Q1}(\text{InP}_1)[\text{MHz}](\text{site1})$	179(1)	179(1)	179(1)	179(1)	179(1)
$\delta_1$	0.15(.1)	0.20(.1)	0.18(.01)	0.18(.1)	0.18(.1)
$\eta_1$	0.0	0.0	0.0	0.0	0.0
$f_1[\%]$	12(2)	20(1)	31(3)	23(3)	21(2)
substitutional site(site 0)					
$\delta_0$	0.02	0.02	0.02	0.02	0.02
$f_0[\%]$	48(2)	44(2)	38(2)	51(3)	59(2)
imperfect subs. site $\nu_Q[\text{MHz}]$	6.60(5)	5.20(4)	10.6(9)	4.01(5)	4.25(3)
$\delta_{01}$	6.0(2)	21(2)	25(10)	22(3)	0.002
$\eta_{01}$	0.0	0.0	0.0	0.0	0.0
$f_{01}[\%]$	23(2)	19(2)	16(2)	13(1)	11(2)
Polycrystalline fraction					
$f_p[\%]$	17(2)	17(1)	15(1)	13(1)	9(2)
Additive constant (C)	-0.0092(2)	-0.013(6)	-0.007(5)	-0.017(4)	-0.007

**Table 4.1:** *Fit results of In-P pairs in silicon*

are obtained by taking into account  $f_{01}$  fraction of the probe nuclei at imperfect substitutional sites, which cause a low frequency modulation of the entire spectra. These imperfections can be due to far sited defects near the probe nuclei disturbing the symmetry of the charge distribution around the probe atom. The population of these sites decreases with annealing temperature but never disappears. This suggests that their exists still some unrecovered radiation damage in the sample. The effect of such small fraction  $f_{01}$  can be seen in the Figure 4.1 by very low frequency modulation ( $\Delta V_{zz} \sim 0$ ) of the time spectra.

### 4.3.2 Reversibility test of In-P pair at high temperature

In an effort to reduce the remaining radiation induced damage (internal strain) due to phosphorous implantation, it was necessary annealing the sample at higher temperatures before subjecting it to an external uniaxial stress. In fact, this leads to dissociation of the formed pairs because the thermal energy attained by the complex at high temperatures exceeds the binding energy that keeps them together. In order to maintain the population of the pairs, reversibility test measurement were carried

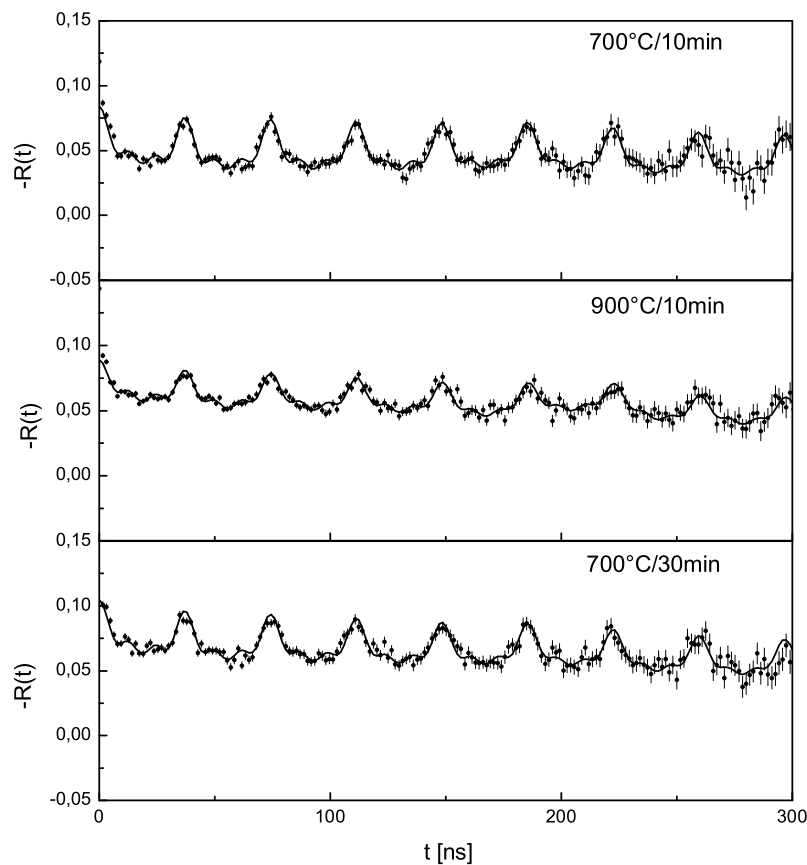


**Figure 4.3:** PAC time spectra showing the retrapping of In-P pair in silicon.



out at the equilibrium concentration of indium phosphorous pair in silicon. Such kind of test has been successfully demonstrated for In-As pairs in Si [WICH89], where a complete re-trapping of pairs has been achieved at 627°C after dissociation by annealing the sample at 900°C. The objective of the test here is to avoid excessive loss of the formed pairs, and at the same time reduce the internal strain of the sample by high temperature annealing. The phosphorous doped sample was annealed first at 700°C for 600 s, the analysis of the time spectrum showed that 31% of the probe atoms form In-P pair (panel 1 Figure 4.3). After annealing the sample at 900°C for 600 s, the fraction of the pairs decreases by nearly 1/3. The sample was then annealed again at 700°C for 30 minutes, now, the PAC data showed an increase in the pair fractional population to 26%. This change of fractional population can be seen in Figure 4.3 by the corresponding change of amplitude of the modulation in the PAC time spectra. Therefore, this result suggests that re-trapping of phosphorous after dissociation at 900°C is possible but difficult to regain completely. However, the fraction of pairs retained by this process is quite enough to observe any effect of uniaxial stress.

### 4.3.3 In-As pairs

The spectra shown in Figure 4.4 are taken from arsenic implanted sample (Energy = 120 keV dose =  $4 \times 10^{14}$  ions/cm<sup>2</sup>). The radiation damage is annealed much quicker than in phosphorous implanted silicon samples, despite the smaller atomic size and lower implantation energy used for phosphorous. All probe nuclei occupy unique lattice sites after annealing the sample at 627°C. At 550°C annealing temperature, already two interaction frequencies are detected which are associated with two dif-

Different In-As complexes	Annealing temperature		
	550°C	627°C	900°C
$\nu_{Q1}(\text{InAs}_1)[\text{MHz}](\text{site1})$	229(1)	229(1)	229(1)
$\eta_1$	0.0	0.0	0.0
$\delta_1$	0.00	0.00	0.00
$f_1[\%]$	46(2)	54(1)	56(2)
$\nu_{Q2}(\text{InAs}_2)[\text{MHz}](\text{site2})$	239(1)	239(1)	239(1)
$\delta_2$	6	5.5	6.25
$\eta_2$	0.65	0.65	0.65
$f_2[\%]$	19(2)	35(1)	14(3)
undisturbed fraction			
$\delta_0$	0.02	0.02	0.02
$f_0[\%]$	20(2)	11(1)	23(2)
Polycrystalline fraction			
$f_p[\%]$	15(2)	0	7(1)
Additive constant (C)	0.009(2)	0.003(4)	0.008(9)

**Table 4.2:** Fit results of In-As pairs in silicon

ferent In-As clusters in silicon. The first complex corresponding to a quadrupole interaction frequency of  $\nu_{Q1} = 229(1)$  MHz ( $\eta = 0$ ) and the second with an interaction frequency of  $\nu_{Q2} = 239(1)$  MHz ( $\eta = 0.65$ ) are measured. Depending on the symmetry of the EFG and dependence of the fractional population of the pairs on the concentration of donors, the measured frequencies were assigned to different indium environments in the substrate lattice, site 1 and site 2 respectively ( see Figure 4.5). The EFG, associated with the QIF of  $\nu_{Q1}$  is symmetric along  $\langle 111 \rangle$  crystal axis, and its fractional population increases with the concentration of the donor atoms. Therefore, this complex was assigned to an indium single arsenic pair  $\text{InAs}_1$  (site 1). On the other hand, the interaction frequency  $\nu_{Q2}$  is assigned to an indium and two nearest substitutional arsenic atoms  $\text{InAs}_2$  (site 2), due to the appearance of the asymmetry parameter  $\eta = 0.65$  and the absence of this complex

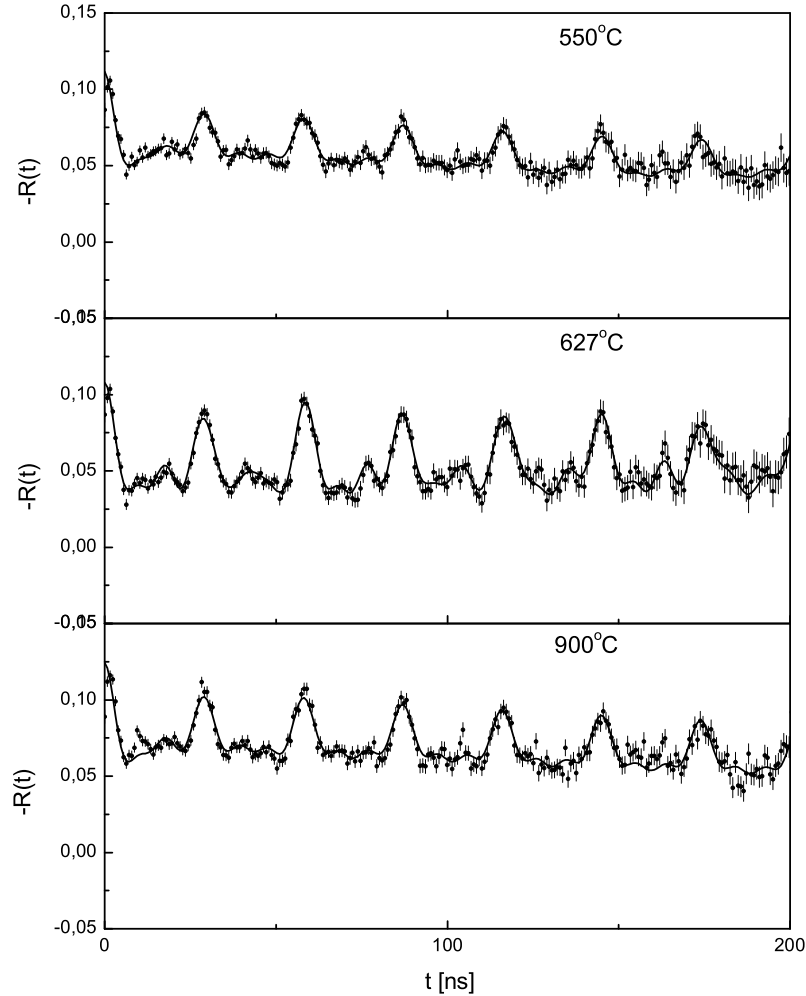


**Figure 4.4:** PAC time spectra from In-As pairs in silicon showing well defined interaction frequencies associated with different indium environments in As doped silicon. The solid line is computer fit according to equation 3.23

for low concentration of donor atoms in the sample (see Figure 4.5). The fraction of the  $\text{InAs}_1$  grows to 54(1)% at 627°C and further increases at high annealing temperatures. On the other hand, the fractional population of  $\text{InAs}_2$  decreases rapidly from maximum population 35(1)% at 627°C to only 14(3)% at 900°C, this indicates weaker binding energy of the latter than to the complex containing one arsenic atom. The fractional population of tetrahedrally symmetric substitutional site of indium rises to 23(2)% at 900°C, and the remaining 7(1)% of the probe atom are in an undefined lattice sites.

### 4.3.4 Discussion

The measured EFGs are the result of an asymmetric charge distributions caused by either the presence of nearby defects and/or unpaired localized charge at the site of the probe atom. In general, the magnitude of the EFGs vary with the type of impurities, if we look only to the tendency of group V donors in silicon, it increases with the size of the atoms (Table 4.3). When an impurity is placed next to a substitutional indium probe atom in Si and Ge crystal, usually it brings about the distortion of the lattice geometry around the complex, which leads to a change in the symmetry of the charge distribution. Therefore, large atomic size would mean strong distortions and large EFGs. Moreover, the EFG varies according to  $r^{-3}$ , the size and the lattice location of an impurity plays a significant role to the magnitude of the EFG. Consequently, since the PAC method is highly sensitive to the defects placed next to the probe atom, it allows one to assign the measured electric field gradients to the different defect complexes in the host lattice. Therefore, the following models (Figure 4.5) are proposed to represent different environments of indium in the diamond structure [WICH89]. These environments of indium result

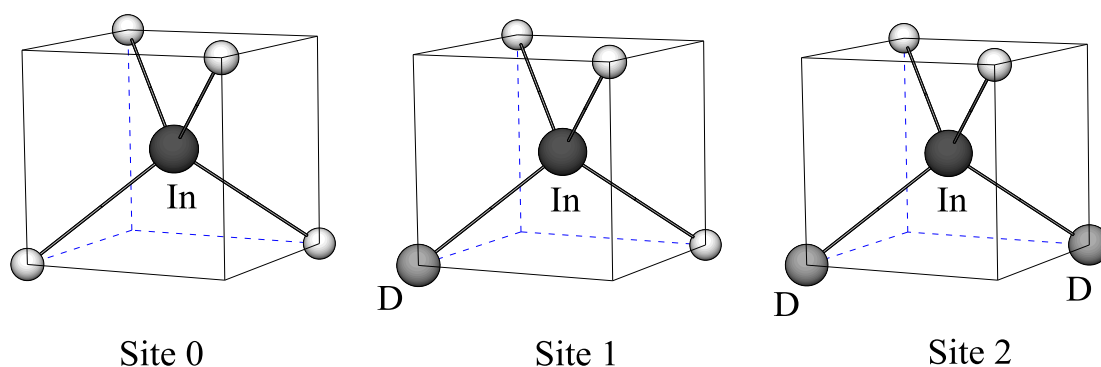


**Figure 4.5:** Models representing possible substitutional indium environment in Si and Ge, where D stands for donor atoms and the white balls are host atoms [WICH89]

in three different electric field gradients in Si and Ge respectively. Site 0 stands for an indium surrounded by four identical host atoms and form cubic environment. The indium experiences no electric field gradient in this site because there exists a symmetric charge distribution at the site of the probe atom. Site 1 has one donor atom next to an indium which breaks the symmetry of the charge distribution leading to a unique EFG. Since indium is a single acceptor in Si and Ge, it satisfies the charge requirement by trapping a single donor. Therefore, Site 1 is the most probable complex in acceptor-donor pairs, which also has large binding energy compared to the complexes containing more than one donor atoms. Besides, this complex is not only favored by its electrical properties but also by the geometrical constraints of the host crystal. For example, in Sb doped sample only site 1 is observed containing one Sb next to an indium (see Chapter 5). The absence of more than one Sb clusters in these measurements suggests that the oversized Sb atom on In-Sb pair creates a high strain field around the complex because of the size mismatch of the atoms involved. Hence, it is unfavorable to take more Sb atoms into already strained complex. The other indium environment in this representation is site 2, it consists of two donor atoms next to the probe, situated along the  $\langle 110 \rangle$  axes. This complex is unique in PAC measurements by the appearance of an asymmetric parameter  $\eta = 0.65$ .

Moreover, based on the thermodynamics of the equilibrium concentration of acceptor-donor pairs [HRYN83], the binding energy of the site 1 was estimated for the different group V donors. The results of the calculation, using the fractional population of the pairs from PAC data, are similar to the value of the binding energy of about 0.5 eV expected on the basis of the mutual Coulombic attraction between a single donor and an acceptor as nearest neighbors in silicon. The different values

pair	InP <sub>1</sub>	InAs <sub>1</sub>	InSb <sub>1</sub>
$\nu_Q$ (MHz)	179(1)	229(1)	271(1)
$E_B$ (eV)	0.69	0.54	0.32

**Table 4.3:** *Binding energy of the indium donor pair in Si [WICH89].*

of the binding energies is attributed to the different strength of the chemical bonds which indium forms with different species of group V donor atoms.

In the effort to verify the proposed structural models and the measured electric field gradients, theoretical calculations have been carried out by Settels et al [SETT99] based on multiple scattering Korringa-Kohn-Rostoker(KKR) Green's function method. The outcome of the calculations showed a remarkable agreement with the values of the measured EFG. Besides, the theory indicates that the magnitude of the EFG is very sensitive to the lattice relaxation around the probe nucleus. This is in fact one of the reasons stimulating further experimental investigations on

the indium donor pairs under the influence of external applied uniaxial stress. Uniaxial stress has the ability to relax the lattice constant in one of the major crystal axis, which in turn expected to cause further asymmetry of the charge distribution at the probe site and a change of the EFG.

## 4.4 Indium-group VI donor pair

### 4.4.1 In-Te pair

In solids, atoms can be ionized at high temperatures and become mobile in the substrate lattice. During the course of migration oppositely charged ions will attract to each other and form different complexes. The fact that Columbic attraction of ionized atoms leads to the formation of In-donor pairs in Si and Ge [WICH89], it is logical to expect the double donors of group-VI elements to form similar complexes in the same materials with the acceptor  $^{111}\text{In}$ . Due to the topological constraints of the host lattice, the group V and VI donors at substitutional sites are expected to form covalent bonds based on  $sp^3$  hybridization with nearest neighbor atoms. Of course, other lattice sites such as interstitial (tetrahedral or non-tetrahedral) are also possible if favorable conditions are met [ANTO86]. In the current PAC experiments, the donor atoms (S, Se, Te) and the isoelectronic carbon atom are used in the search for new pairs, and to investigate their structure in the substrate lattice. In this effort, a new quadrupole interaction frequency has been detected for Te in Si but it was not possible to see a characteristic QI frequency for the rest of the species from this group.

### 4.4.2 Results

In the study of In-Te pairs in silicon a different implantation program was used. First, radioactive indium isotope ( $^{111}\text{In}$ ) was implanted and then the samples were annealed for 600 s in vacuum at  $900^\circ\text{C}$ . Consequently, tellurium was implanted with 50 keV and a dose of  $(0.45 - 1) \times 10^{15}$  ions/cm $^2$ . The implantation energy of 50 keV, which separates the implantation profile with indium, is chosen because of the larger diffusion coefficient of tellurium in silicon than indium [LABO98]. At  $900^\circ\text{C}$  annealing temperature and 600 s holding time the diffusion length of tellurium is about 50 nm while it is only 11 nm for indium. Following the post-implantation, the PAC time spectra are taken after every isochronal annealing steps. At low annealing temperatures the PAC data showed only radiation damage. Panel 1 of Figure 4.6 shows the first sign of recovery of the radiation damage after tellurium implantation and annealing the sample at  $500^\circ\text{C}$  for 600s. At this temperature significant recrystallization has occurred, nearly  $f_0 = 72(2)\%$  of the probes occupy a

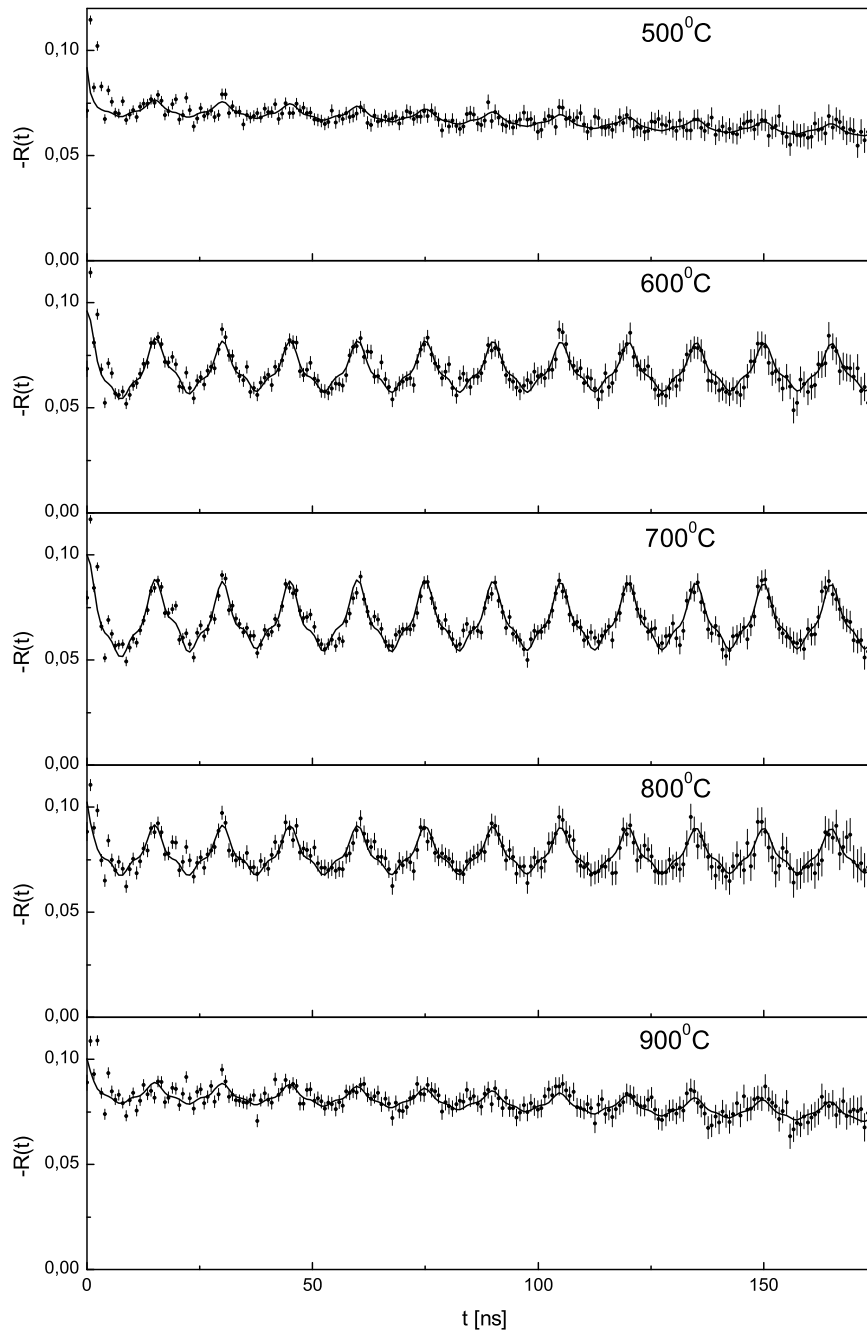


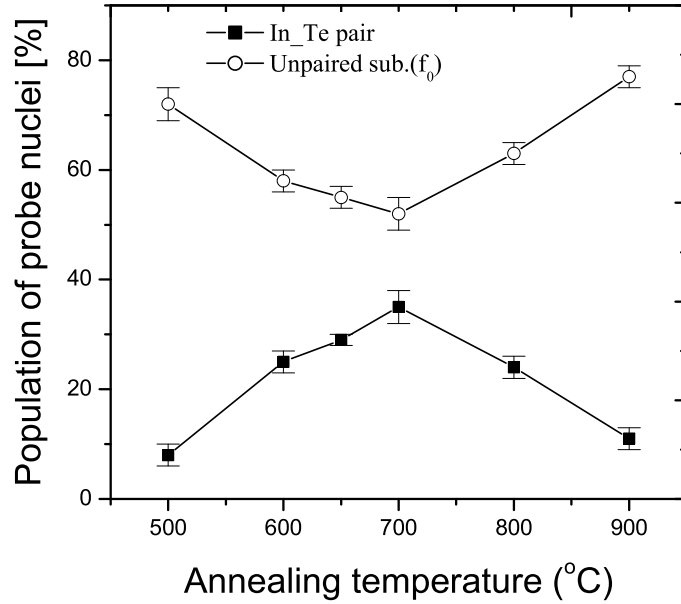
**Figure 4.6:** PAC time spectra from a Te doped Si sample showing the interaction frequency after different annealing temperatures. The detectors are positioned along  $\langle 100 \rangle$  crystal axis. The solid lines are theoretical fits according to equation 3.8 and equation 3.23.

perfect substitutional lattice site, and  $f_1 = 8(3)\%$  of the probe atoms are associated with a new frequency modulation. The remaining  $20(3)\%$  are in an unidentified lattice location. A well defined new interaction frequency is observed after annealing the sample at  $600^\circ\text{C}$  panel 2 of Figure 4.6. The quadrupole coupling constant of this

In-Te and other complexes	Annealing temperature					
	500°C	600°C	650°C	700°C	800°C	900°C
$\nu_{Q1}(\text{InTe}_1)[\text{MHz}](\text{site1})$	444(1)	444(1)	444(1)	444(1)	444(1)	444(1)
$\delta_1$	0.5(6)	0.20(2)	0.20(1)	0.20(2)	0.20(2)	0.19(2)
$\eta_1$	0.0	0.0	0.0	0.0	0.0	0.0
$f_1[\%]$	8(3)	25(1)	29(2)	35(3)	24(2)	11(3)
Subs. site(site 0)[MHz]	0.0	0.0	0.0	0.0	0.0	0.0
$\delta_0$	0.002	0.002	0.002	0.002	0.002	0.002
$f_0[\%]$	72(2)	59(3)	55(2)	52(2)	63(3)	77(3)
Polycrystalline fraction						
$f_p[\%]$	20(3)	16(2)	16(1)	13(1)	13(1)	12(1)
Additive constant	-0.009(3)	-0.006(2)	-0.005(3)	-0.002(1)	-0.0001(6)	-0.003(4)

**Table 4.4:** Fit results for In-Te pairs in silicon

interaction frequency is  $\nu_Q = 444(1)\text{MHz}$  and  $\eta = 0$ . The fractional population of this complex ( $f_1$ ) grows to a maximum at 700°C. Annealing the sample above 700°C leads to a gradual decrease of  $f_1$  as seen by the diminishing amplitude of modulation in the time spectra. Figure 4.7 shows the fractional population of the two indium

**Figure 4.7:** The fractional population of the probe nuclei at different lattice sites in Te implanted silicon.

sites versus temperature. A small value of  $f_1$  already appeared at 500°C annealing temperature but this signal is influenced by the value of damping ( $\delta = 0.5$ ) because of incomplete recovery of the radiation damage. The fraction of  $f_1 = 25(1)\%$  is detected at 600°C, a maximum 35(3)% of the probe atoms are associated with the frequency at 700°C. Higher annealing temperatures show the dissociation of the

complex, for instance only 11(3)% remained after annealing the sample at 900°C. On the other hand, the observed 72(2)% tetrahedrally symmetric substitutional site of indium at 500°C decreases by the formation of the In-Te complex, but it increases again at high temperatures by the dissociation of the complex.

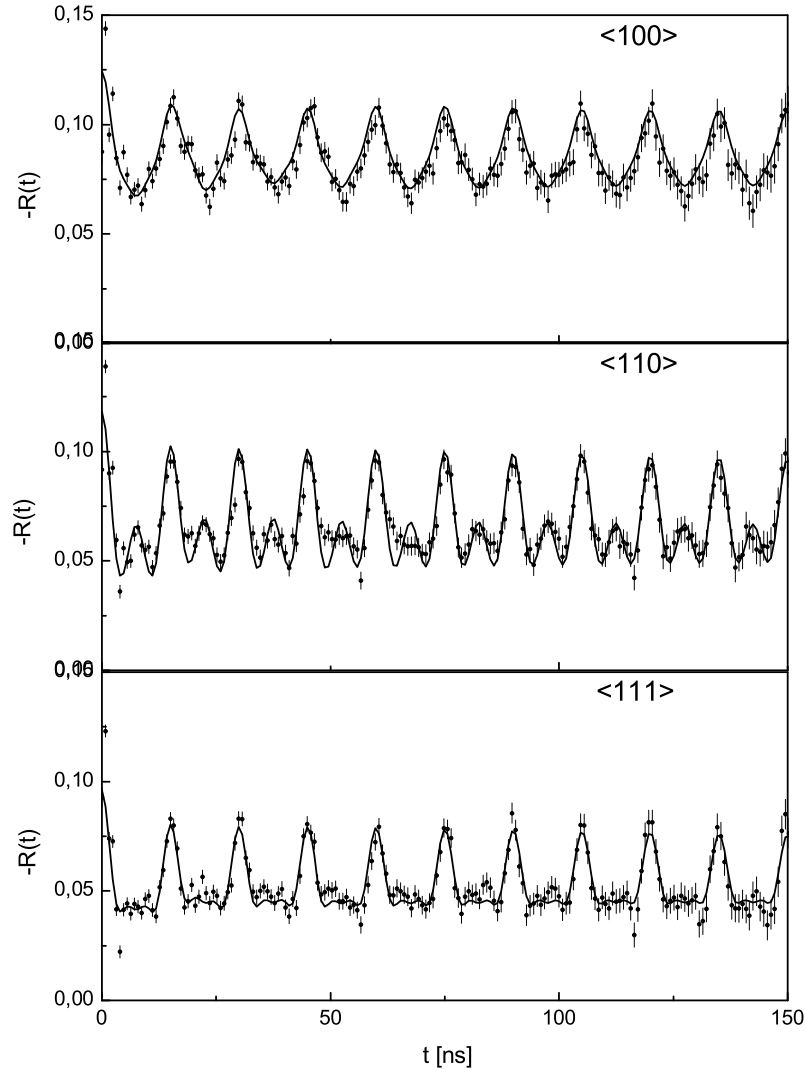


**Figure 4.8:** Orientation measurement of the In-Te pair in Si, showing the different patterns of the time spectra when the crystal axes indicated in the panels are pointed to wards detectors.

Figure 4.8 shows the orientation measurements of the EFG of the In-Te pair in silicon. During each of these measurements the detectors are aligned to one of the major crystal axes  $\langle 100 \rangle$ ,  $\langle 110 \rangle$  or  $\langle 111 \rangle$  as indicated in the panels. The different patterns of the PAC data match the theoretical fit function by assuming the direction of the principal EFG component to lie along the  $\langle 100 \rangle$  crystal axis.



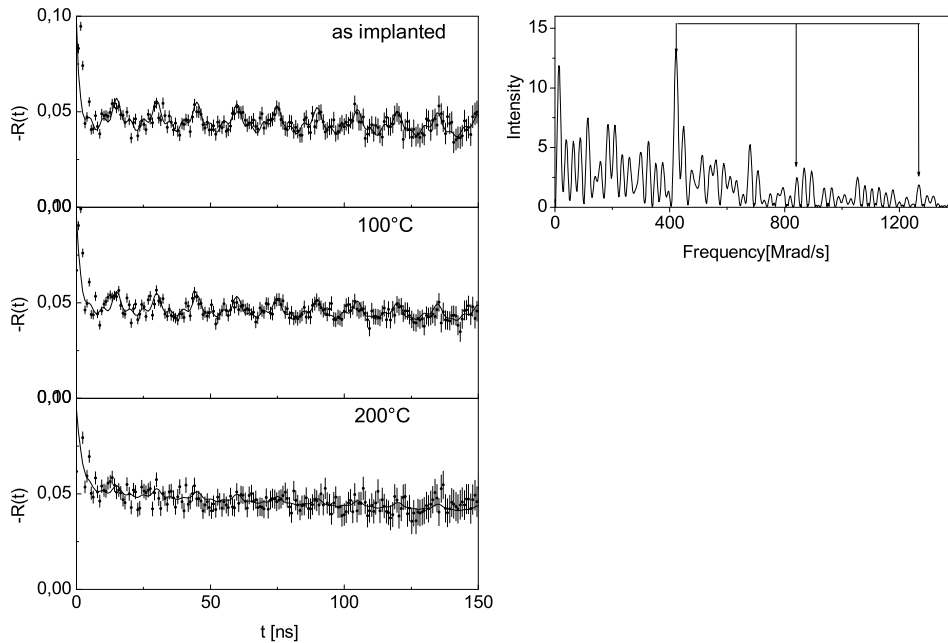


**Figure 4.9:** PAC time spectra from Te doped Si sample showing the interaction frequency right after implantation. The right panel shows Fourier transform of the as implanted time spectra.

The slight variation on the shape of the pattern in panel 1 of Figure 4.8 and panel 2 of Figure 4.6 is due to the different anisotropy coefficients used as consequence of the various detector sample distance (see section 3.2).

The time spectra of Figure 4.9 were taken from a different sample. Right after Te implantation the PAC signal showed a well defined interaction frequency of 444 MHz. Moreover, the Fourier transform of the time spectrum demonstrates the existence of a unique interaction frequency above the noise signals expected from implantation damage. The fraction of this frequency decreases after annealing the sample by 100°C for 600s and then eventually disappears at the temperature near 200°C due to incomplete recovery of the radiation damage. The fit results of the data showed an increase in the width of the frequency distribution around the mean value as we go from as implanted to 200°C to the value nearly ( $\delta = 0.75$ ). This is so because the recrystallization often takes place in silicon near 500°C [MAYR70] but during annealing below 250°C allows defect migration in random fashion leading to a dissociation of the pairs by vacancy and interstitial impurity interactions which result in the reduction of the population of the complexes created during implantation. Moreover, different implantation profiles of the solute atoms are chosen during implantation, which require atoms to diffuse to one another in order to increase the probability of pair formation. At low temperatures the diffusion is not sufficient to overcome the gap between the two profiles and form the desired

In-Te and other complexes	Annealing temperature		
	as implanted	100°C	200°C
$\nu_{Q1}(\text{InTe}_1)[\text{MHz}](\text{site1})$	444(1)	444(1)	444(1)
$\delta_1$	0.34(3)	0.45(2)	0.75(4)
$\eta_1$	0.0	0.0	0.0
$f_1[\%]$	15(2)	12(1)	6(2)
perfect subs. site			
$\delta_0$	0.002	0.002	0.002
$f_0[\%]$	35(2)	40(3)	48(2)
Polycrystalline fraction			
$f_p[\%]$	50(3)	48(2)	46(1)
Additive constant	-0.005(3)	-0.007(2)	-0.008(3)

**Table 4.5:** *Fit results of In-Te pairs in silicon from as implanted to 200°C annealing temperature.*

pairs, instead it leads to the dissociation of the existing complex by the various interaction processes.

### 4.4.3 Discussion of the results

In tellurium implanted silicon a new interaction frequency of 444(1) MHz ( $\eta = 0$ ) is measured at an annealing temperature near 550°C. According to the orientation measurements, the main component of the EFG ( $V_{zz}$ ) lies along the  $\langle 100 \rangle$  crystal axis. This new interaction frequency is nothing but the result of the existence of Te in Si, because, the frequency has never been seen before for other impurities in silicon. Due to the absence of an additional frequency in a wide range of annealing temperatures the observed frequency is assigned to an indium and tellurium pair (In-Te). Further, the  $\langle 100 \rangle$  orientation of the measured EFG suggests that Te does not possess a regular substitutional site in the host lattice. Although point charge model is not sufficient to describe completely the observed EFG in PAC, it can serve as guide to interpret the data. From this point of view, if tellurium were on a substitutional site in silicon, the resulting EFG would have been directed along the line joining the two ions (In-Te) in the complex, which in most cases would lie on the  $\langle 111 \rangle$  crystal axis in silicon. Based on the orientation of the EFG and results of channelling measurements, which are discussed below, a possible lattice location of tellurium in diamond lattice structure of silicon can be the octahedral interstitial site. In fact, this is the largest free space available in this structure where a large atom like tellurium can be easily accommodated. The tendency of group-VI donors to occupy octahedral lattice site in silicon is predicted by [ANTO86] with valence electron configuration  $(s^2p^2)p^2$ . Therefore, there are six equivalent substitutional sites of indium in this complex next to tellurium, which according to point charge model lead to a  $\langle 100 \rangle$  orientation of the EFG (see Figure 4.10).

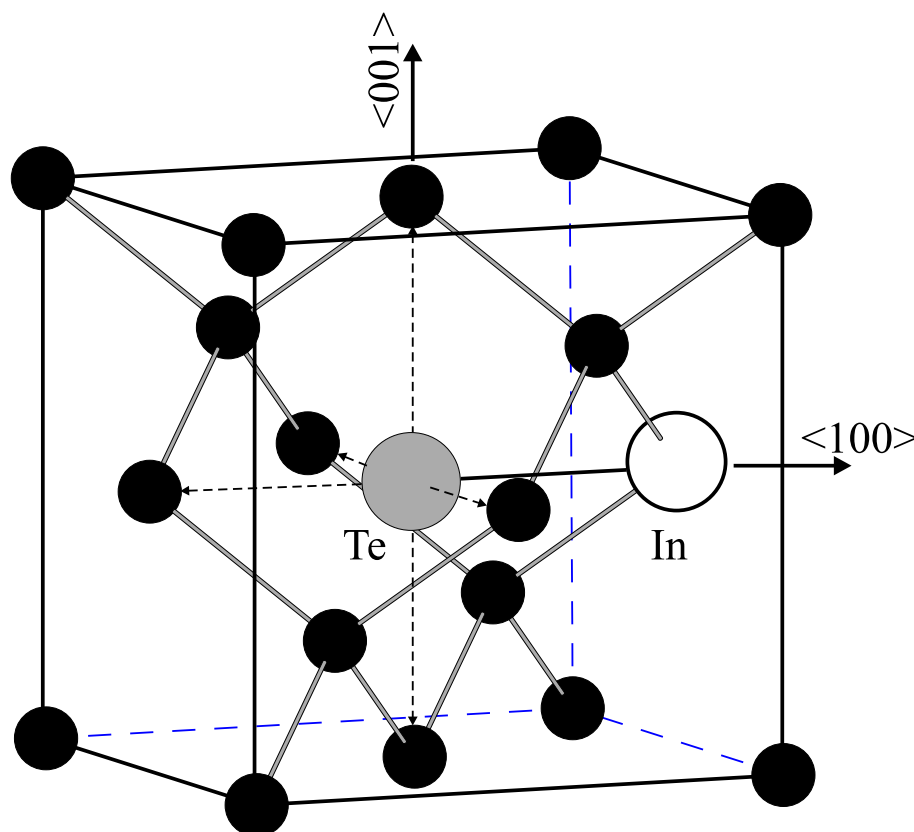


**Figure 4.10:** Possible lattice structure of the In-Te pair in silicon.

The structural assignment of group-VI impurities in silicon is generally difficult because of its chemical properties with the host atoms. However, there is evidence [LEEW75, FRER84, ANTO86] that suggests tellurium's preferential occupation at non-substitutional lattice locations in silicon. Based on the results of ion channelling, W. Lee et al. [LEEW75] have determined that substitutional fraction of tellurium in silicon varies with the implanted dose. In their report, only 30% substitutional Te was measured for a dose of  $1.4 \times 10^{15}$  atoms/cm<sup>2</sup>, but 80% substitutional Te was reported for  $1.4 \times 10^{14}$  atoms/cm<sup>2</sup>. Hence, the substitutional fraction of tellurium in silicon is strongly influenced by the implantation dose. In the current measurements, an interaction frequency is observed for doses of  $(1-3) \times 10^{15}$  atoms/cm<sup>2</sup>, which according to channelling information can be regarded as a range of doses where the majority of implanted tellurium atoms are on non-substitutional sites. On the other hand, no interaction frequency was detected for tellurium doses  $\leq 4 \times 10^{14}$  atoms/cm<sup>2</sup>. Therefore, the proposed octahedral lattice location of tellurium is in line with large non-tetrahedral interstitial fractions of tellurium measured in silicon by high resolution ion backscattering method [FRER84, ANTO86].

Another experimental evidence for the less probable occurrence of substitutional tellurium at high doses comes from the work of H. P. Frerichs and et al. [FRER84],

using high resolution ion backscattering method. Direct after implantation of tellurium in silicon, they found no detectable substitutional fraction. This information gave an hint to the current measurement that the observed frequency right after implantation is the result of the interaction of indium with non-substitutional tellurium. Moreover, the interaction frequency observed after the post-implantation of tellurium is identical with the frequency obtained after annealing the sample. This implies that in both cases the frequency is generated from an identical complex in the host lattice. The population of  $f_1 = 15(2)\%$  of the probe atom represent this complex after implantation, while  $f_0 = 35(2)\%$  of the pre-implanted indium remains undisturbed by the post implantation. This shows that the Te implantation did not completely disturb the sites of indium because of different implantation profile used for the solute atoms. According to the proposed model (see Figure 4.10), it is clear to understand that during implantation some of the Te can be channelled through the crystal, and those which are able to reach the indium implantation profile form the complex (In-Te). Hence, the frequency is most likely represents the interaction of indium with non-substitutional tellurium in silicon.

When we look to the tendency of damage recovery, the sample is quickly annealed most of the damages it sustained during implantation (first panel of Figure 4.6). At 500°C annealing temperature substantial fraction of the indium atoms have already occupied substitutional lattice sites. This is presumably due to low post-implantation energy used that caused comparatively low radiation damage. The detection of 35(3)% fraction of the In-Te complex at 700°C indicates that there exist considerable amount of Te at the interstitial sites even after high annealing temperature. Despite the time spectra showed significant recovery of the radiation induced damage.

The reversibility of the formation of the In-Te pair was also tested after its dissociation near 800°C (see Appendix A). The experiment showed no re-trapping occurred at 700°C annealing temperature for 40 min holding time after its dissociation at 900°C. Therefore, for such irreversible process, it is possible to apply first order kinetics to estimate the dissociation energy of the complex :

$$E_d = kT \ln \left[ \frac{1}{t\nu} \ln \left( \frac{N_0}{N} \right) \right] \quad (4.1)$$

where  $E_d$  is energy of dissociation and  $\nu$  the attempt frequency whose value is equal to the phonon frequency  $\nu = 10^{13} s^{-1}$  [SKUD92b].  $N_0$  and  $N$  are the initial and final population of the complex after annealing the sample at  $T$  for time  $t$ . Using the maximum population of the In-Te pair and its population at 800°C, the resulting value of the dissociation energy of the complex according to equation (4.1) is 3.45 eV. Which is comparable to the activation energy of diffusion of Te in an intrinsic silicon 3.06 eV at 800°C [LABO98]. The difference is a consequence of the additional energy required to break up the In-Te complex in silicon.

#### 4.4.4 Temperature dependence of the EFG at the In-Te pair

The measurement of the quadrupole interaction frequency (QIF) of the In-Te pair in silicon at different temperatures showed a strong temperature dependence of the electric field gradient characterizing the complex. The magnitude of the EFG of the complex decreases with increasing sample temperature. In non cubic metals, this variation of the EFG with temperature is best described by the well known empirical relation  $T^{3/2}$  [CHRS76]. This  $T^{3/2}$  dependence of the EFG in metals is considered to be the result of lattice expansion and vibration. In semiconductors, evidence was found [BARF82] that there exists a striking relationship between the EFG and the density of charge carriers in the conduction band. Therefore, based on additional PAC data, a new model was proposed and applied for the first time to the  $\text{In}_2\text{Te}_5$

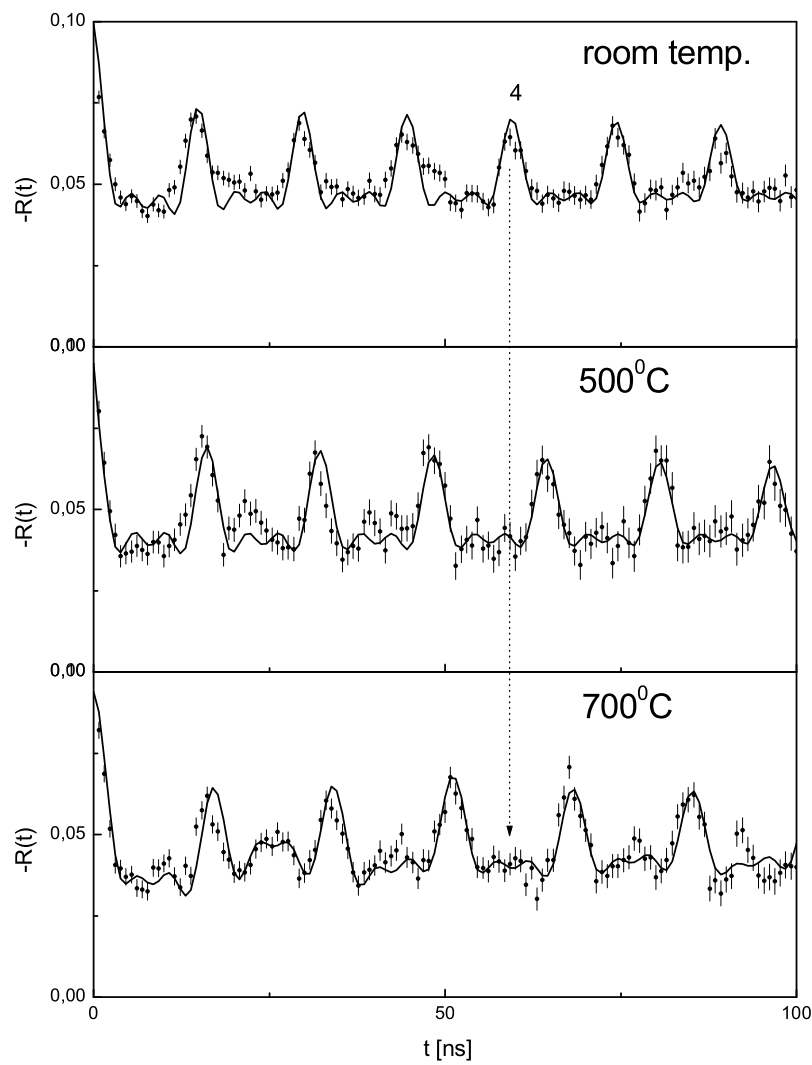


**Figure 4.11:** PAC time spectra of In-Te pair measured at different temperatures

compound semiconductor by [FORK83] and later to silicon [ACHT89]. It describes very well the observed temperature dependence of the electric field gradient.

The basic idea behind the model is that the variation of the EFG with temperature is the result of the two different charge states of the  $^{111}\text{Cd}$ -impurity complex during the time of the measurement. The population of the charge states changes with temperature, resulting in different average interaction frequency. At a given temperature, an equilibrium situation can be maintained between the population of the two states [ACHT93]. This model is applied to the In-Te complex in silicon, where tellurium takes octahedral sites along the  $\langle 100 \rangle$  crystal axis. Tellurium is neutral at octahedral sites in silicon in a completely occupied surrounding, with valence electron configuration  $(s^2p^2)p^2$  [ANTO86]. Due to topological constraints of the diamond lattice, substitutional indium is ionized because of the  $sp^3$  hybridization required to make bonds with neighboring host atoms. This extra electron is not locally satisfied, it can be obtained from the valence band. However, it is also available from the nearest interstitially located tellurium. Therefore, the transfer of an electron from the nearest octahedral site of tellurium to a substitutional indium is assumed in order to form a neutral In-Te complex. In this way, the charge requirement is locally satisfied. Hence, indium is electrically passivated. In fact, there are several evidence on the existence of neutral and single ionized tellurium in silicon [WAGN84]. By the time the indium transforms to Cd, the  $(\text{Cd-Te})^-$  complex is charged at low temperature because of the high density of charges. Increasing the sample temperature the density of charge decreases because of the dissolution of ions and favors the neutral complex  $(\text{Cd-Te})^0$ . The charge states of  $(\text{Cd-Te})^-$  and  $(\text{Cd-Te})^0$  result in two different electric field gradients  $V_{zz}(-)$  and  $V_{zz}(0)$  at the cadmium nucleus. Due to the general difficulty of determining the exact charge states of the complexes by PAC, this assignment is based on the fact that a high charge state would result in a large  $V_{zz}$ . Therefore, in the intermediate range the state of the complex is neither neutral nor negative, but fluctuates. This fluctuation of states is described by the Fermi-Dirac probability distribution  $P(T)$  for ionized states as

$$P(T) = \frac{1}{1 + g \cdot \exp\{(E_a - E_F)/kT\}} \quad (4.2)$$

Here  $g$  is the ground state degeneracy factor, which is 4 for Si and Ge, because, each acceptor impurity level can accept one hole of either spin and the impurity level is doubly degenerate as a result of the two degenerate valence bands at  $K = 0$ .  $E_a$  is the energy gap between the acceptor level of the complex  $(\text{Cd-D})^-$  and the valence band and  $E_F$  is the Fermi energy. In equation 4.2 the temperature dependent Fermi energy is used, which is given by

$$E_F = \frac{E_a}{2} - \frac{kT}{2} \ln\left(\frac{n_A}{p_0} T^{-3/2}\right) \quad (4.3)$$

where  $n_A$  is the acceptor impurity concentration and  $p_0 = 2\left(\frac{2\pi m_e^* k}{h^2}\right)^{3/2}$ ,  $m_e^*$  is the

effective mass of a defect electron. In general the average electric field gradient is

$$V_{zz}(T) = V_{zz}(0)[1 - P(T)] + V_{zz}(-)P(T) \quad (4.4)$$

In order to take into account the effect of lattice expansion and vibration, it was necessary to include the empirical factor  $(1 - \alpha T^{3/2})$  to fit the data

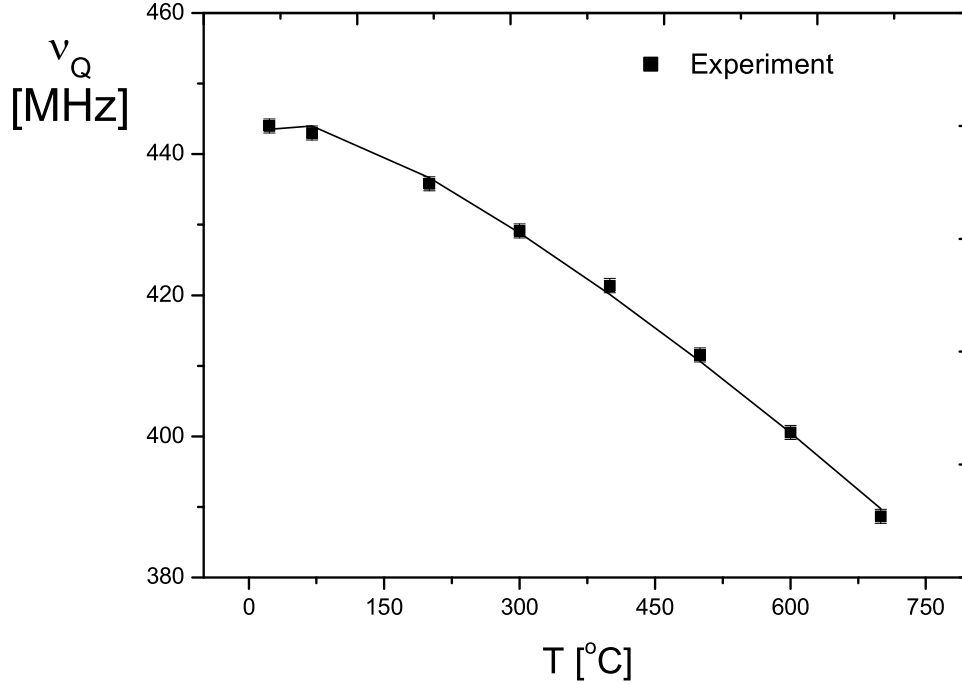


**Figure 4.12:** Quadrupole interaction frequency of the In-Te pair in silicon at different temperatures. The solid line is a fit according to equation(4.5)

$$V_{zz}(T) = (1 - \alpha T^{3/2}) \left\{ V_{zz}(0) + [V_{zz}(-) - V_{zz}(0)] \cdot \frac{1}{\left(1 + g \sqrt{\frac{n_A}{p_0} T^{-3/2} \cdot \exp(E_a/kT)}\right)} \right\} \quad (4.5)$$

The solid line in Figure 4.12 is the fit according to equation 4.5. The QIF of 444(1)MHz and 388(1)MHz are used for  $V_{zz}(-)$  and  $V_{zz}(0)$  respectively. The acceptor level of  $E_a$  and the concentration of acceptor impurities  $n_A$  are taken as free parameters in the fit and the result showed  $E_a = 0.24\text{eV}$  and  $n_A = 8.7 \cdot 10^{16} \text{atoms/cm}^3$ . The value of the impurity concentration found is of similar magnitude to the acceptor concentration ( $^{111}\text{In}$ ) usually used in the PAC measurements. The coefficient  $\alpha = 0.52 \times 10^{-5} \text{K}^{-3/2}$  is also obtained from the term that intended to include the thermal effect.

### 4.4.5 Selenium implanted silicon

In section 4.4.1, it was briefly indicated that the implantations of sulfur and selenium in silicon did not lead to the observation of unique quadrupole interaction frequency. Here, an example from one of the implantations in silicon is presented. Figure 4.13 show the time spectra taken after the implantation of selenium with dose of  $0.5 \times 10^{15}$  atoms/cm<sup>2</sup> and energy 120 keV. Different annealing programs were tested for the holding time 120 s, 300 s and 900 s respectively in vacuum, however, all of them produced similar results. Right after implantation the time spectra show only radiation damage caused by post implantation. The sign of recovery of the radiation damage was observed for the first time after annealing the sample at 550°C. At this step, nearly 60% of the probes occupy substitutional lattice site surrounded by host atoms (panel 1 of Figure 4.13). Successive high temperature annealing did not show unique interaction frequencies, instead, the population of

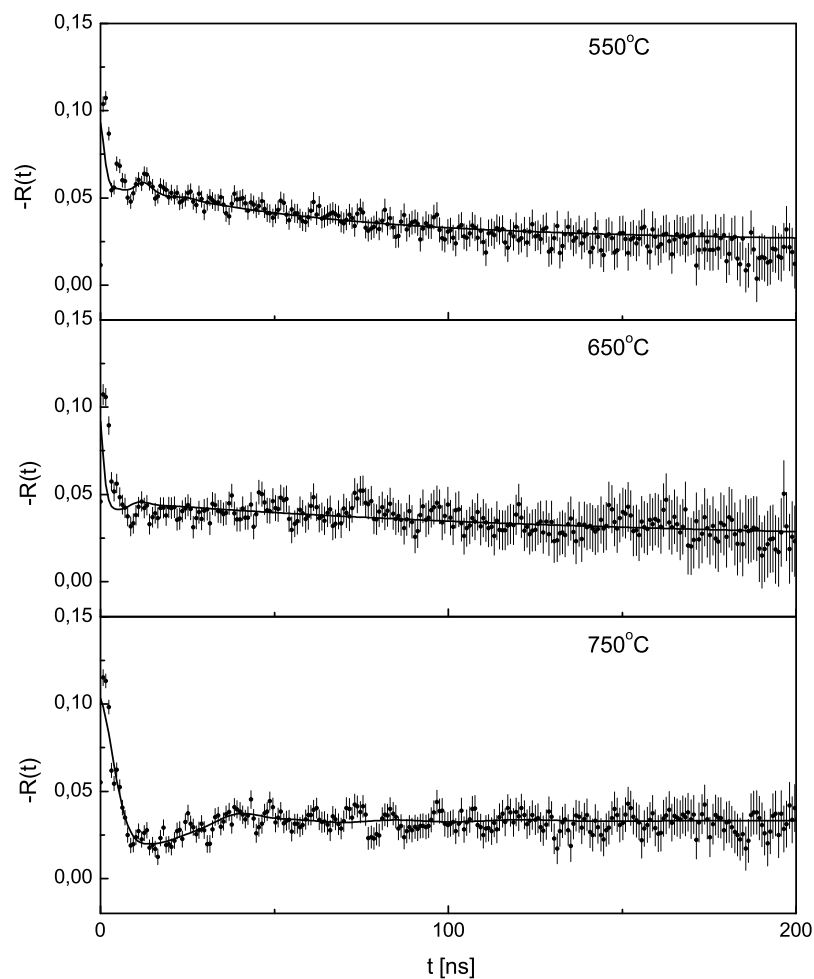


**Figure 4.13:** PAC time spectra taken from selenium implanted silicon.



the substitutional probe atoms decreases to about 30% at 750°C. This can be seen clearly by decreasing value of the coefficient of anisotropy at high temperatures. Normally, high annealing temperature enhances the population of substitutional indium in silicon, as a consequence, the value of coefficient of anisotropy increases. But, the time spectra taken after selenium implantation showed different from the expected behavior. It suggests that the indium environments are indeed affected by the presence of selenium in the sample. This is likely to be the result of a new chemical formation at the indium sites, resulting in high EFGs that can not be resolved by the PAC apparatus.

## 4.5 Indium-Carbon pair in Germanium

### 4.5.1 Introduction

The utilization of carbon in semiconductor technology has begun since the past few decades in combination with other elements and compounds. Carbon plays a vital role in the modification of the properties of semiconductors. For instance, carbon is one of the building blocks for an important wide band gap semiconductor such as SiC, which is used for high temperature devices. Among its many applications important to the present discussion, carbon is used to compensate strain in SiGe compound semiconductor [EBER92]. Apart from deliberate incorporation of carbon into materials, it is also one of the major residual impurities next to oxygen in CZ grown silicon and germanium [HALL82, HALL82]. Because of such reasons, it still remains interesting to study carbon in both Si and Ge.

Relatively much attention was not given until recently in the formation of GeC system, because of the very low solubility ( $10^8\text{cm}^{-3}$  -  $10^{10}\text{cm}^{-3}$ ) [SCAC59] of carbon in germanium. However, using the electron cyclotron resonance (ECR) plasma processing method Herrold et al. [HARR00] were able to grow microcrystalline thin film of germanium-carbide on different substrates up to 2% carbon concentration. The newly grown germanium-carbide is reported to have 1.1 eV energy band gap, very close to that of silicon, depending on the carbon concentration. This is a very important progress toward obtaining crystalline germanium carbide, which has suitable electrical and optical properties. Moreover, implantation technique is also utilized for doping carbon in germanium substrate [HOFF97] and this work. After the recovery of the radiation induced damage, Hoffmann et al. have observed significant fraction of the implanted carbon at regular substitutional lattice sites.

In general, there is a growing interest in recent years in the investigation of carbon in semiconductors. The perturbed angular correlation (PAC) method has also been employed in an attempt to study carbon in Si, but an In-C pair was not observed for several possible reasons discussed by Ott et al.[OTT94]. However, using infrared

spectroscopy, it was found that indium forms pairs with carbon in Si [COLI81]. Therefore, at first sight an indium-carbon pair is also expected in germanium because of its similar chemical properties with silicon. This could be favored by the role of carbon in compensating the strain caused by the implantation of an oversized indium atoms in germanium.

In the current experiment, an investigation is conducted using the PAC method to extend the study of the properties of carbon in germanium. In this effort, in addition to the contribution of information about the incorporation of carbon in the host lattice, it provides new values of the electric field gradients (EFGs) to the theoretical calculations of isoelectronic impurities in germanium. In this work carbon is detected at two lattice locations after different annealing temperatures. Discussion of the thermal stability of the defect complexes and comparison with the results of other methods will be made in the following sections.

### 4.5.2 Formation and thermal stability of the In-C pair in Ge

After the post-implantation of carbon the spectrum shows a highly disturbed PAC signal. The first sign of recovery of the radiation induced damage is observed after annealing the sample at 450°C (see panel 1 of Figure 4.14). The PAC signal is gradually modulated by an interaction frequency of  $\nu_{Q1} = 207(1)$  MHz ( $\eta = 0.16(3)$ ). This frequency is associated with the existence of high concentration of carbon in germanium. The amplitude of modulation increases with temperature (panel 2 and 3), showing the population growth of the defect complex. The spectra are accompanied by the frequency damping of  $\delta_1 = 1.7(6)$  and  $\delta_1 = 1.5(4)$  at 550°C and 600°C respectively. The decreasing tendency of damping with temperature indicates improvement in the recovery of radiation induced damage near the defect complexes. After annealing the sample above 600°C, this frequency is replaced by another interaction frequency of  $\nu_{Q2} = 500(1)$  MHz and ( $\eta = 0$ ) (see Figure 4.15) representing new indium environments. The difference between these two frequencies can be seen from the figures by the various time scales used. The latter dominates the remaining PAC spectra up to 850°C. Some samples were annealed close to the melting point of germanium at 900°C, which causes substantial loss of activity of the  $^{111}\text{In}$  making further measurements difficult. In order to identify the orientation of the EFGs with respect to the host lattice, PAC time spectra were taken along the three major crystal axes, such as  $\langle 100 \rangle$ ,  $\langle 110 \rangle$  and  $\langle 111 \rangle$  respectively. The Fourier transform of these time spectra are given in (Figure 4.16 and 4.17) after annealing the sample at 600°C and 750°C respectively. Figure 4.16 shows distinctly separated amplitudes of the three transition frequencies ( $\omega_1$ ,  $\omega_2$  and  $\omega_3$ ) of the first quadrupole interaction frequency (site 1a of Figure 4.18) of carbon with indium. In all three crystal axes orientations, the amplitude of the first

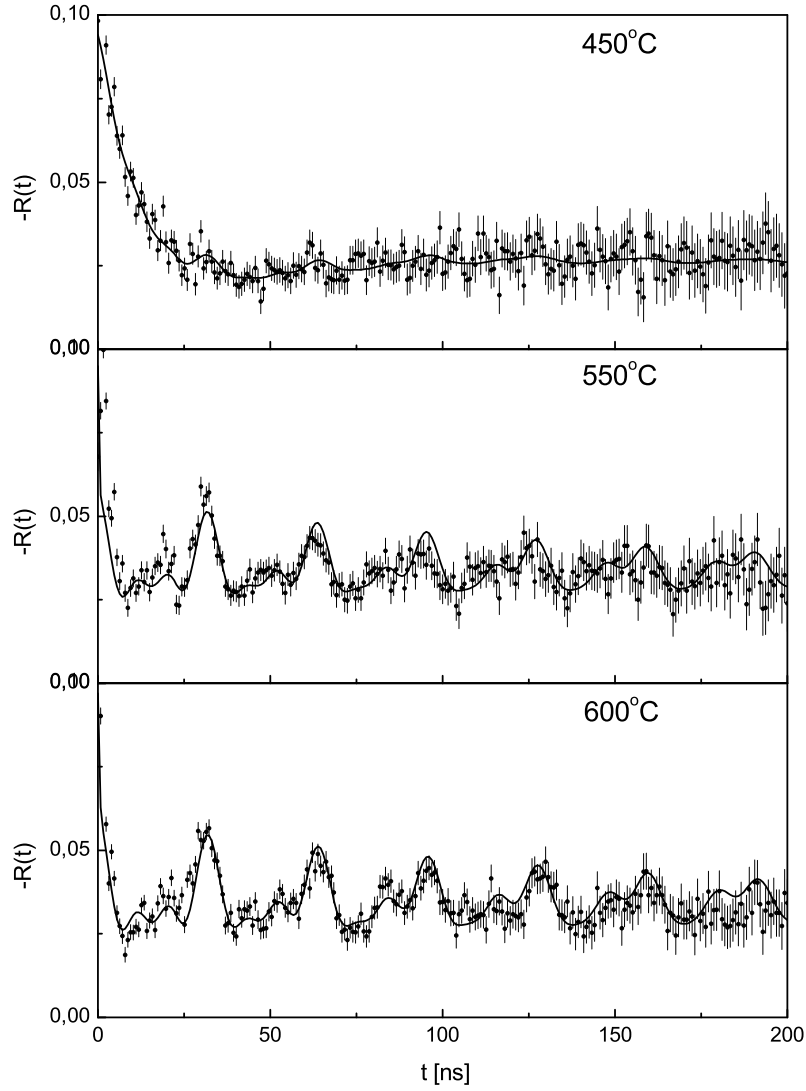


**Figure 4.14:** PAC time spectra from a carbon doped Ge sample showing the modulation of the time spectra with a well defined frequency. Below 650° C annealing an interaction frequency of  $\nu_{Q1} = 207(1)\text{MHz}$  ( $\eta = 0.16(3)$ )(site 1a) is observed. The solid line is the theoretical fit according to equation 3.23

transition  $\omega_1$  remains dominant (see panel 1-3). However, when the detectors are positioned along the  $\langle 111 \rangle$  crystal axis the amplitudes of  $\omega_2$  and  $\omega_3$  almost vanish. This is commonly seen in a diamond lattice as the alignment of  $V_{zz}$  in the direction of the detectors. The same results are observed for the second interaction frequency 500(1) MHz in Figure 4.17. Therefore, in both cases the principal component of the EFGs ( $V_{zz}$ ) of the interactions of carbon with indium in germanium lie along the  $\langle 111 \rangle$  crystal axis.

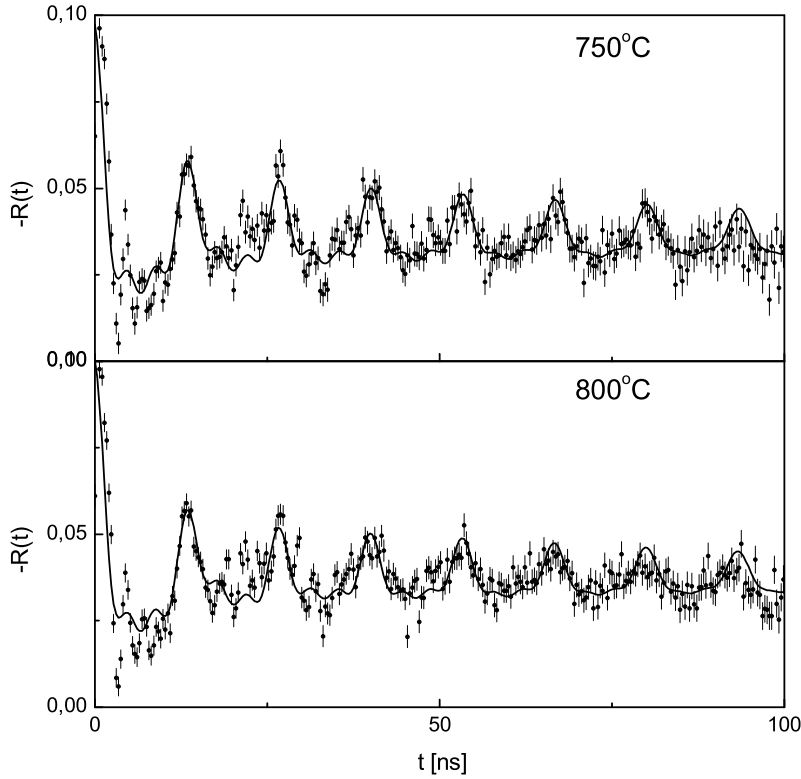


**Figure 4.15:** PAC time spectra of In-C pair above  $650^\circ\text{C}$  annealing temperatures with an interaction frequency of  $\nu_{Q2} = 500(1)$  MHz and  $\eta = 0$ . The solid line is the fit according to equation 3.23

### 4.5.3 Discussion of the results

In carbon implanted germanium two frequencies are detected after annealing the sample above  $450^\circ\text{C}$ . According to the orientation measurements the principal component ( $V_{zz}$ ) of these EFGs both lie along the  $\langle 111 \rangle$  crystal axis. Figure 4.19 shows the fractional population of the different indium environments in the sample. Below  $450^\circ\text{C}$  annealing temperature no unique interaction frequency is observed, however, there exists a small fraction of the probe atoms at undisturbed substitutional site. This fraction gradually grows at higher annealing temperatures as the sample recovers from radiation induced damage. At  $450^\circ\text{C}$ , nearly  $10(2)\%$  of the probes are found in new environments (site 1a, see Figure 4.18). This site is populated to a maximum of  $f_{1a} = 34(2)\%$  of the probe atoms after annealing the sample at  $600^\circ\text{C}$ . At higher temperatures the fraction decreases and finally disappears at  $700^\circ\text{C}$ . When the depopulation of site 1a begins above  $600^\circ\text{C}$ , another interaction frequency representing a different indium environment (site 1b) is evolved. The population of site 1b increases rapidly with annealing temperature, it grows to a

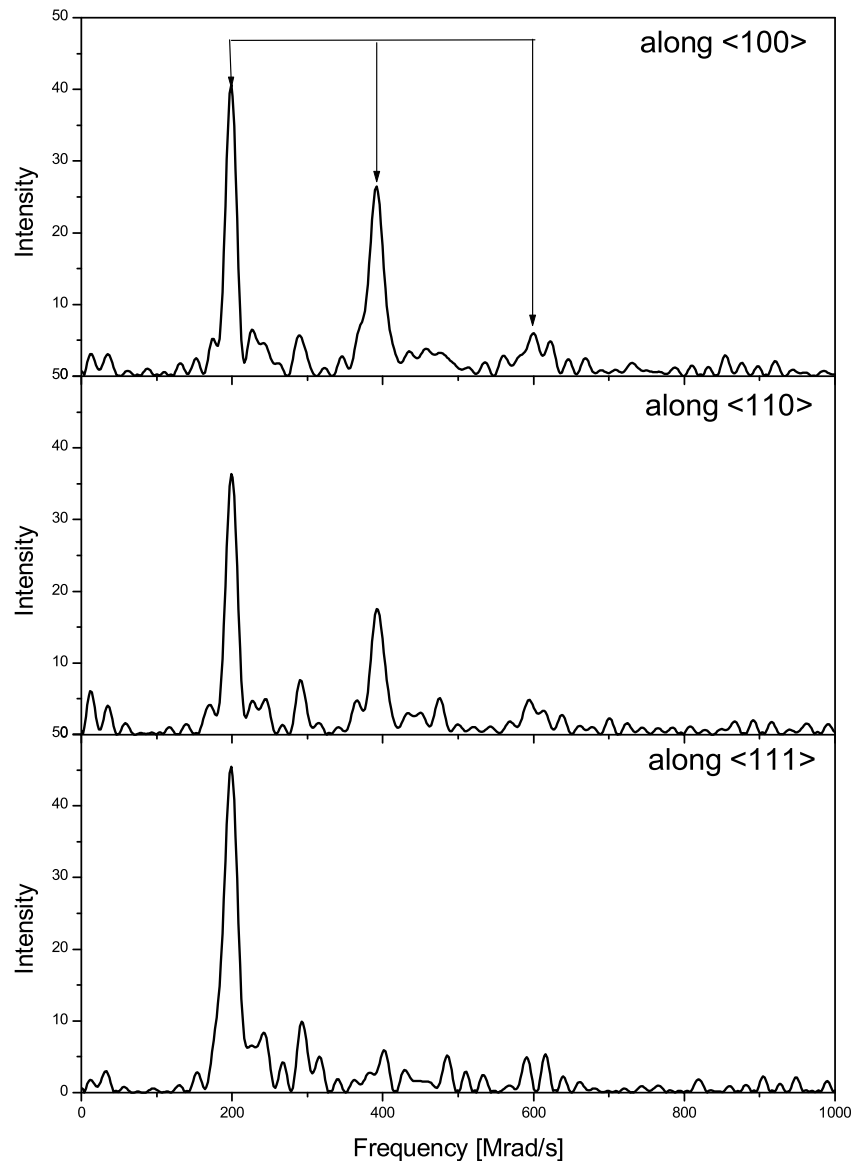


**Figure 4.16:** *Fourier transform of the PAC time spectra taken from C doped Ge sample at different crystal axis after 600° C annealing temperature representing the interaction frequency  $\nu_{Q1} = 207(1)\text{MHz}$  of site 1a*

maximum of  $f_{1b} = 35(2)\%$  at 750°C. High temperature annealing leads to the dissociation of this defect complex above 750°C. In all the spectra, substantial fraction of the probe atoms are observed at non-unique lattice sites that can not be resolved by the present PAC apparatus. Above 450°C annealing temperatures, the best fits to the data are obtained by taking into account about  $f_p = 48(3)\%$  of the probes to the lattice sites with a highly disturbed environments. These sites could be associated with several carbon clusters (precipitates), which are a consequence of different

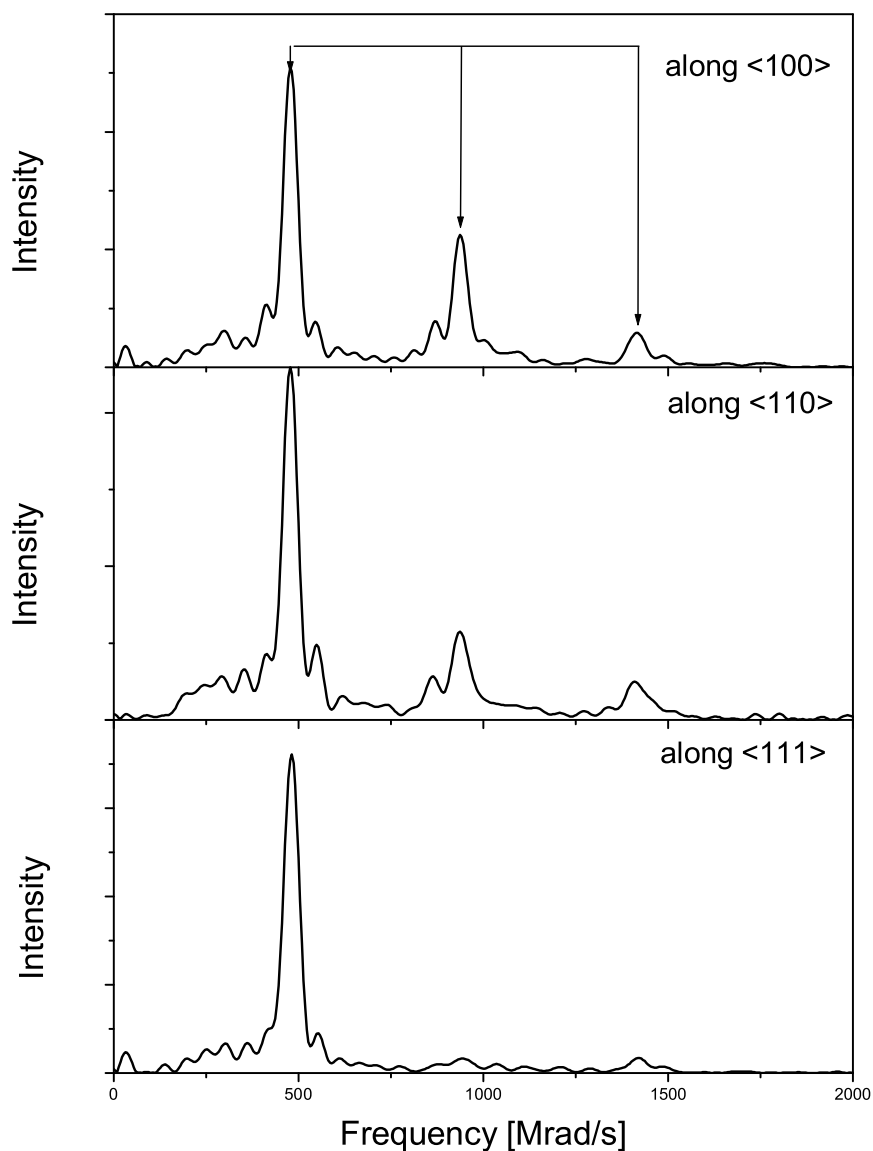


**Figure 4.17:** Fourier transform of the PAC time spectra taken from C doped Ge sample at different crystal axis after  $750^{\circ}\text{C}$  annealing temperature representing the interaction frequency  $\nu_{Q2} = 500(1)\text{MHz}$  of site 1b

chemical formation at the site of the probe atoms.

According to the infrared absorption and ion channelling studies of carbon in germanium [HOFF97], which will later be discussed in comparison with the current results, a significant fraction of substitutional carbon is reported in the range of annealing temperature from  $350^{\circ}\text{C}$  to  $700^{\circ}\text{C}$ . Another lattice location of carbon at high temperatures was not indicated by these methods. In PAC, it is possible to identify two distinct lattice sites characterized by the measured quadrupole interaction frequencies. From the present data, one can draw conclusion about the nature

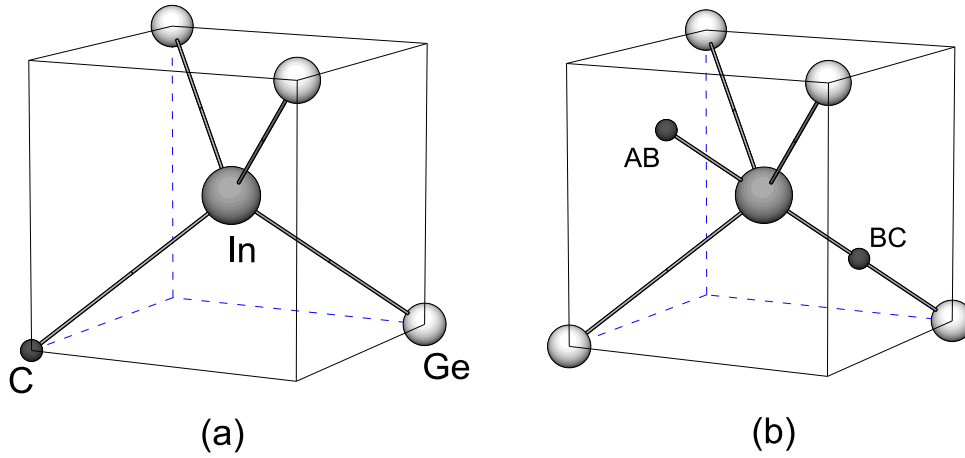


**Figure 4.18:** Possible lattice site of C in germanium after different annealing temperature (a) substitutional carbon (site 1a) (b) carbon in an interstitial lattice (site 1b), which is on either bonding or antibonding center.

of the defects. Therefore, based on the symmetry of the EFG along the  $\langle 111 \rangle$  crystal axis and channelling information on substitutional carbon in germanium, the measured interaction frequency of 207(1)MHz is assigned to the interaction of a substitutional indium and carbon pair. Both substitutional and interstitial sites have a cubic symmetry in diamond lattice. However, the existence of the asymmetric parameter ( $\eta = 0.16(3)$ ) at (site 1a) suggests that carbon is not in a perfect substitutional site in germanium. But, it could have taken a near substitutional position, which can lead to the change in the symmetry of the charge distribution around the probe nucleus. This is consistent with the estimated  $0.2\text{\AA}$  displacement of carbon from regular lattice site by ion channelling [HOFF97]. The second frequency (site 1b) is most likely a pair of substitutional indium and interstitial carbon.

In-C pair and other complexes	Annealing temperature						
	450°C	550°C	600°C	650°C	700°C	750°C	800°C
$\nu_{Q1}(\text{InC})[\text{MHz}](\text{site } 1a)$	207(1)	207(1)	207(1)	207(1)			
$\delta_{1a}$	4.32(6)	1.75(2)	1.50(1)	1.50(1)			
$\eta_{1a}$	0.16(3)	0.16(3)	0.16(3)	0.16(3)			
$f_{1a}[\%]$	10(2)	30(2)	34(2)	14(3)			
$\nu_{Q2}(\text{InC})[\text{MHz}](\text{site } 1b)$				500(1)	500(1)	500(1)	500(1)
$\delta_{1b}$				3.5(1)	1.5(1)	1.5(1)	1.5(1)
$\eta_{1b}$				0.0	0.0	0.0	0.0
$f_{1b}[\%]$				16(2)	31(2)	35(2)	32(2)
perfect subs. site							
$\delta_0$	0.002	0.002	0.002	0.002	0.002	0.002	800°C
$f_0[\%]$	16(2)	22(3)	19(2)	23(2)	20(3)	18(3)	17(2)
Polycrystalline fraction							
$f_p[\%]$	74(2)	48(1)	47(2)	47(3)	49(2)	47(1)	51(2)
Additive constant	-0.010(3)	-0.0095(2)	-0.0077(3)	-0.0093(1)	-0.0083(1)	-0.0067(1)	-0.0039(1)

**Table 4.6:** Fit results for In-C pairs in germanium

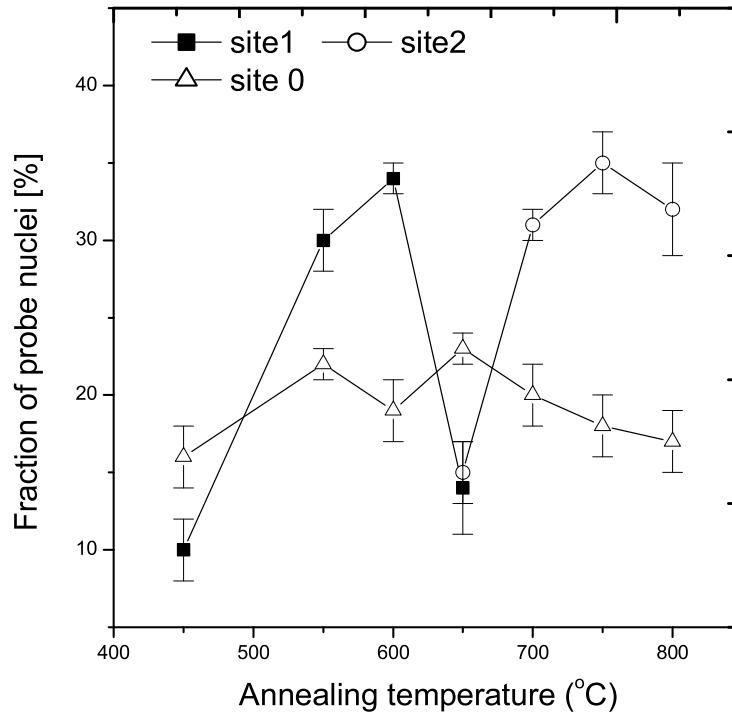


**Figure 4.19:** *Fraction of the probe nuclei at different environments in carbon doped germanium*

Other possibilities for site 1b, such as more than one substitutional C atoms around a probe nucleus is not impossible, but it is less probable because of significant difference of the bond length of C-C ( $1.53\text{\AA}$ ) and Ge-Ge ( $2.41\text{\AA}$ ) [BERD97]. Moreover, the measured asymmetry parameter ( $\eta = 0$ ) from this site leaves even two C cluster next to an indium out of question. Because, two substitutional nearest neighbors at the probe site in diamond lattice usually result in non zero asymmetry parameter. Therefore, the most probable location of carbon at high annealing temperatures is either a bonding or anti-bonding interstitial center.

The frequency damping is generally large in all the spectra taken after carbon implantation. Damping values  $\delta_{1a} = \delta_{1b} = 1.5(2)$  are obtained at  $600^\circ\text{C}$  and  $750^\circ\text{C}$  annealing temperatures respectively. This is evident in the figures (see Figure 4.14 and 4.15) by decreasing amplitudes of modulation with time. The frequency damping is believed to be the result of the radiation damage caused by carbon implantation. However, its presence even at high annealing temperatures (up to  $800^\circ\text{C}$ ) suggests that the sample is not completely recovered from the damage, or it has sustained permanent surface deformation. Carbon implantation is not expected to cause permanent damage by the chosen implantation parameter, but during crystal regrowth the nature of the surface could be changed because of the various size of atoms participation. Heterogeneous surface lattice structure can be caused by the lattice mismatch between germanium and the small covalent radius of carbon



atoms [DEAN79]. The inhomogeneity of lattice could lead to slight variation of the surrounding of the same complexes that contain indium and carbon. Such non-uniform environments would result in a wide statistical distribution of the electric field gradient around the mean value, causing a frequency damping in the time spectra. Moreover, the presence of a substantial fraction of the probe atoms in an undefined lattice location would also indicate the complex nature of carbon implanted germanium crystal.

The preliminary experimental tests show that the observed complexes are not reversible after dissociation at 650°C and 800°C respectively. Therefore, based on first order kinetics (equation 4.1), the dissociation energies of the complexes are estimated to be 2.84 eV and 3.52 eV for substitutional and interstitial carbon in germanium respectively. The difference in the dissociation energies is the result of the various energy required to form substitutional and interstitial carbon in the host lattice. These values are not exaggerated compared to the energies  $\sim 2.8\text{eV}$  and  $\sim 4.7\text{eV}$  required to break the Ge-Ge and Ge-C bonds respectively [GAYD68]. Moreover, the In-C complexes discussed here involve atoms In, Ge and C, which have different thermodynamic property than the Ge-C system.

#### 4.5.4 Comparison with results of ion channelling and infrared absorption measurements

An interesting similarity is observed between the results of PAC on the one hand and ion channelling and infrared absorption methods by L. Hoffmann et al. [HOFF97] on the other. According to infrared absorption measurements, after the implantation of  $^{12}\text{C}$  in germanium and subsequent annealing at 450°C, a single sharp absorption line is observed at  $531\text{-cm}^{-1}$ . This line is shifted down to  $512\text{-cm}^{-1}$  when  $^{12}\text{C}$  is replaced by another carbon isotope  $^{13}\text{C}$ . The frequency ratio between the two lines is 1.037, which differs by only 0.4% from  $\sqrt{13/12}$ , as it is expected for a carbon atom bound by a harmonic potential to a rigid lattice. According to this result and comparison with theoretical calculation, it has been concluded that the  $531\text{-cm}^{-1}$  line represents a local vibrational mode of one carbon atom bound to germanium.

On the same sample, ion channelling measurements were also carried out to identify the lattice location and estimate the fractional population of the different lattice sites of carbon in germanium. The measured angular distributions of proton and deuteron yields around the three major axes are shown in Figure 4.20 [HOFF97]. For all three axes, there is a dip in the proton yield when the beam is aligned with the axis. The width of the dips is close to the that of backscattered deuterons, but the normalized minimum yields for the protons are much higher than those for the deuterons. Only substitutional (perfect lattice site) or near substitutional sites are consistent with broad dips in yield for all three major axes. A significant

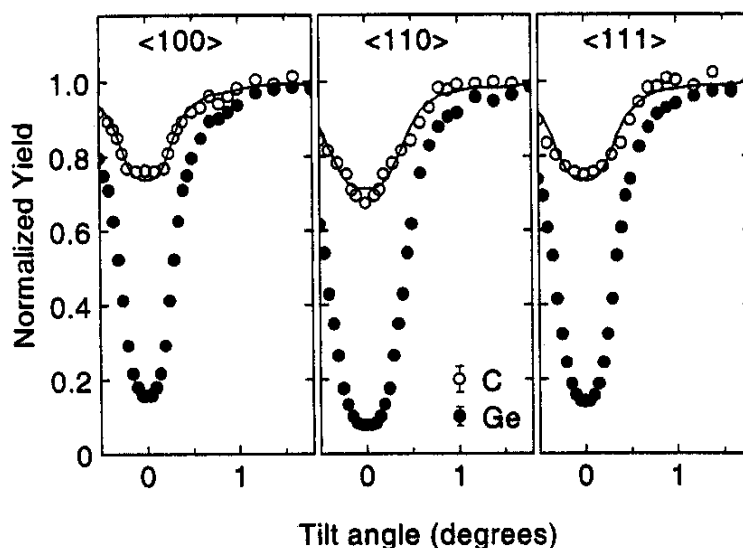


**Figure 4.20:** Results of ion channelling study of substitutional carbon in germanium [HOFF97]

fraction of the carbon atoms are consequently located at substitutional sites. The solid lines through the data points in the figure represent the best fit to the data. The fit correspond to 31(3)% of carbon atoms located at substitutional sites while the remaining 69(3)% are located randomly.

The effect of isochronal annealing on the substitutional carbon is tested by both methods in the temperature range between 450°C and 700°C. That is, the intensity of 531-cm<sup>-1</sup> absorption line and the yield of < 110 > curves by ion channelling are compared (Figure 4.21). The 531-cm<sup>-1</sup> mode begins to appear at 350°C and reaches a maximum intensity at 450°C. Annealing at higher temperatures leads to a decrease in the intensity and eventually the mode disappears at 700°C. The < 110 > proton-yield curves show a broad dip at 450°C, which is proportional to the population of substitutional carbon as discussed above. When the temperature is increased the dip decreases indicating the depopulation of the substitutional carbon. At 602°C, the dip starts to narrow, which shows that a new well-defined carbon structure is formed at this temperature. At 700°C, the substitutional dip is completely gone and yet a new structure is formed which gives rise to a peak at zero tilt angle. Thus, qualitatively, the disappearance of the 531-cm<sup>-1</sup> mode occurs in parallel with depopulation of the substitutional sites.

Comparing the range of temperature in which substitutional carbon is observed by ion channelling and infrared absorption method (Figure 4.21) and the detection of site 1a by PAC (Figure 4.19). We see a similar range of temperature that all the methods are able to detect the occurrence of well defined structural site of carbon in germanium. According to these information, it is possible to conclude that site 1a with an interaction frequency  $\nu_Q = 207(1)$  MHz is the result of the

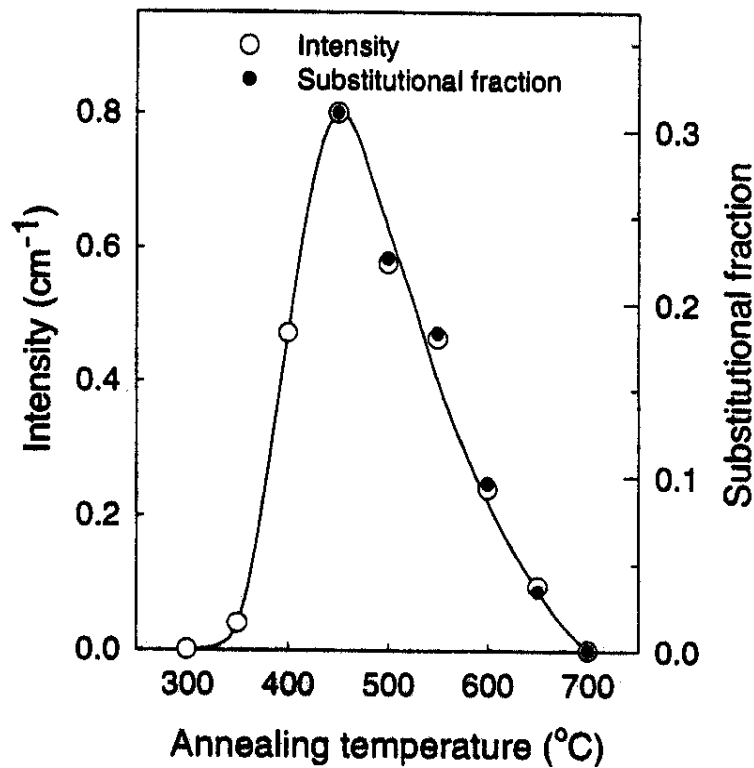


**Figure 4.21:** Results of the intensity of the line  $531\text{ cm}^{-1}$  of infrared absorption on the one hand and substitutional carbon by ion channelling on the other in germanium [HOFF97]

interaction of indium with substitutional carbon. Moreover, the disappearance of the substitutional fraction of carbon in Ge above  $650^\circ\text{C}$  annealing temperature by the ion channelling method suggests, that the observed lattice site (site 1b) in PAC is not a consequence of the interaction of indium with substitutional carbon.

Finally, the ratio of the quadrupole coupling constants of the two complexes yields  $\nu_{Q1}/\nu_{Q2} = 0.414$ . Based on the point charge model, assuming interstitial carbon carries charge twice as that of substitutional, the ratio of the proximity of carbon to the indium at the interstitial and the substitutional sites is  $r_i/r_s = 0.9$ . Which is of course far from expected unless interstitial carbon occupy anti-bonding site instead of bonding (Figure 4.18). This result clearly shows the inadequacy of the model, which makes difficult to derive the exact interstitial position of carbon from the measured data. However, the  $r^{-3}$  dependance of the electric field gradient, and the fact that the magnitude of the EFG of site 1b is about two times larger than that of site 1a, suggest that, carbon at site 1b is with close proximity to the indium than site 1a. Therefore, the most probable location of site 1b by this comparison is once again an interstitial.

# Chapter 5

## EFFECT OF UNIAXIAL STRESS on In-IMPURITY PAIRS in Si

### 5.1 Introduction

The study of hyperfine fields under the influence of external uniaxial stress has been carried out employing different methods on the various defect complexes in elemental and single crystal semiconductors. Using electron spin resonance, G. D. Watkins et al. [WATK60] have studied the effect of preferred alignments of defects and quantitative determination of the magnitude of the electronic redistribution under uniaxial stress. Recently, the perturbed angular correlation method has also contributed new information about the influence of uniaxial stress at the site of the probe atom ( $^{111}\text{In}$ ) in silicon and germanium by G. Marx [MARX95]. In PAC, the application of uniaxial stress on a sample basically induces electric field gradients at the site of defect complexes by changing the charge distribution around the probe atoms. By the external uniaxial stress, probe atoms are not expected to change their lattice location but lose the natural symmetry of the charge distribution.

In the silicon and germanium diamond structure, the probe nuclei ( $^{111}\text{In}$ ) occupy substitutional lattice sites in well annealed samples (see section 3.3.2). In these lattice sites, they experience no electric field gradient because there exists symmetrically cubic lattice environment. This symmetry can be broken if the probe atom either trap a defect or by the presence of an externally induced lattice relaxation at the probe sites. These conditions would lead to the appearance of a unique interaction frequency in a PAC time spectra.

Figure 5.1 shows a unit cell of the diamond lattice structure, which is composed of 18 atoms in a cube of side  $\mathbf{a}$ . The probe atom replaces one atom in this unit cell when it takes a substitutional site. In doing so, it forms tetrahedral covalent

bonds with the surrounding host atoms and possesses a position equidistant from the four nearest neighbors which in turn makes a cubic surrounding whose side is  $1/2\mathbf{a}$ , equivalent of  $1/8$  of the volume of the unit cell. From the point of view of the

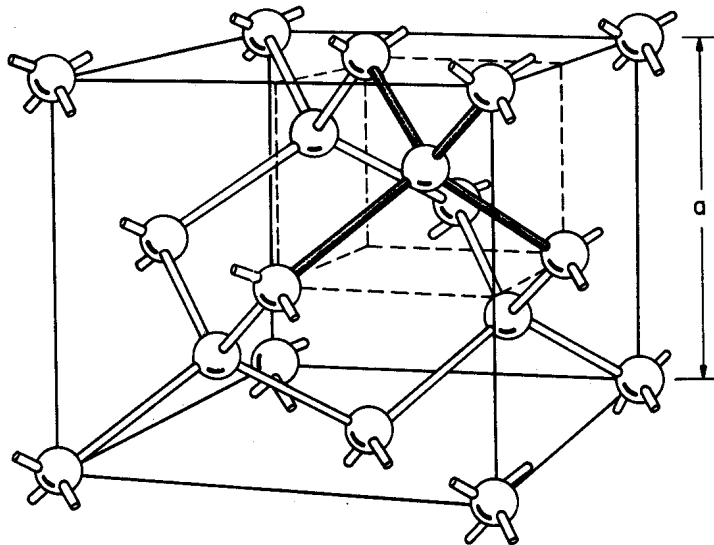


**Figure 5.1:** A unit cell of the diamond lattice structure of Si and Ge. It is composed of 18 atoms. A section of the diagram with dashed lines shows cubic environment of a lattice site.

group symmetry this cubic environment has several degrees of symmetry freedom. As seen in Figure 5.2, it has four threefold rotational axes along the  $\langle 111 \rangle$  direction, three two fold rotational axes along  $\langle 100 \rangle$  and two vertical reflection mirror planes. This cubic structure leads to an electric field gradient tensor whose

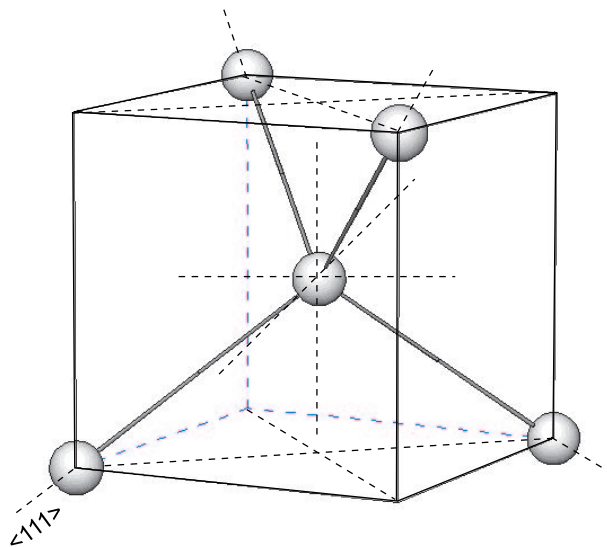


**Figure 5.2:** Rotational and reflection plane symmetry of the cubic environment.

components possesses zero value in its principal axis system, i.e.  $V_{xx} = V_{yy} = V_{zz} = 0$  and consequently zero asymmetry parameter ( $\eta = 0$ ).

Uniaxial stress along the  $\langle 110 \rangle$  crystal axis causes variation of the lattice parameters around the probe atoms mainly along the same direction. Hence, it lowers the symmetry of the cubic environment of the substitutional atoms. Major lattice deformation is expected to take place in the direction of the applied stress, which also coincides with the direction of the principal component of tension induced EFG ( $V_{zz}$ ). This direction of the  $V_{zz}$  is confirmed by the orientation measurements [MARX95]. The relationship between the magnitude of the EFG and the strength of deformation has been discussed in the previous work. There is a direct correlation between them, i.e. whenever there is an increase in lattice deformation in one direction there is a corresponding increase of  $V_{zz}$  in the same direction. Therefore, the field gradient tensor follows a similar pattern of changes as the direction of deformation. However, it is still difficult to tell exactly which environment is

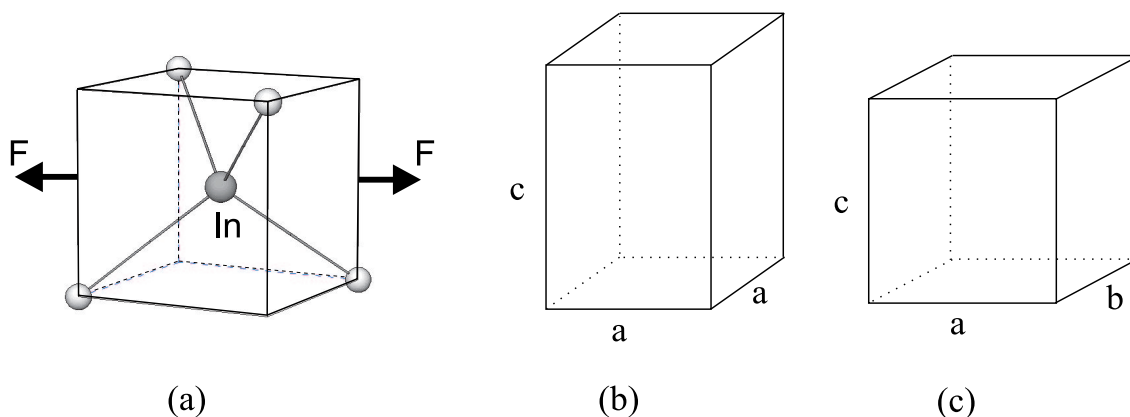


**Figure 5.3:** Possible change of indium environment under the influence of uniaxial stress along  $\langle 110 \rangle$ . (a) cubic, (b) tetragonal and (c) rhombohedral

formed at the probe site in a stressed sample. But, there are some possible lattice configurations that can be considered in this situation. Among the many possible lattice configurations the simplest form of deformations like tetragonal and rhombohedral structure are expected from the action of uniaxial stress along the  $\langle 110 \rangle$  axis. The resulting field gradient tensors in both cases have a non zero value. For instance, in the rhombohedral structure whose sides are  $a \neq b \neq c$  the tensor of the EFG would also behave as  $V_{xx} \neq V_{yy} \neq V_{zz} \neq 0$  and  $\eta \neq 0$ . In tetragonal structure where  $a = b \neq c$  the tensor of the EFG would be  $V_{xx} = V_{yy} \neq V_{zz} \neq 0$  and  $\eta = 0$ .

## 5.2 Method of creating uniaxial stress

In order to create uniaxial stress, samples are prepared with edges along one of the major crystal axes. In the current experiments the samples were cut 7 mm wide and 20 mm long, the length was cut along the  $\langle 110 \rangle$  crystal axis. In doing so, the  $\langle 110 \rangle$  axis is chosen to transmit stress along the same direction and causing deformation at the site of the probe atoms. Pressing between two cylinder heads

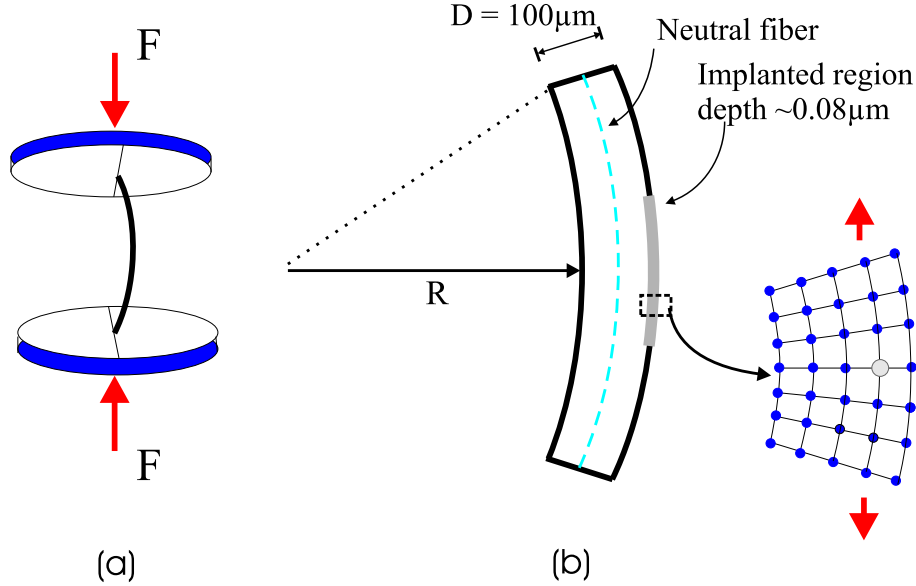


**Figure 5.4:** Techniques of producing uniaxial stress on implanted samples. (a) a sample between two cylinder heads (b) Schematic diagram of tensile stressed sample and microscopic environment of a probe atom.

causes the sample to bend like a smooth arc. In this way, it is possible to create two types of stress on the opposite faces of the sample (see Figure 5.4b). In the outer surface a tensile stress is created since lattice constants are stretched. The inner face will have a compressional stress by the opposite change of the dimension of the lattices. In both cases a deformation takes place along the direction of the stress i.e. the  $\langle 110 \rangle$  crystal axis. In an atomic scale the change of the lattice constant can be regarded as linear. For a linear deformation like this the stress  $\sigma$  can be determined experimentally by the equation

$$\sigma = E \cdot \frac{\Delta L}{L} \quad (5.1)$$

where  $E$  is elastic modulus and  $\Delta L/L$  is the relative change of length of the sample, which by this method can reach values of the order of  $10^{-3}$ . In a small linear deformation where Hook's law holds, the second-rank stress tensor  $\sigma_{ij}$  and the

fourth-rank elastic tensor  $C_{ijkl}$  are given by the relation

$$\sigma_{ij} = \sum_{kl} C_{ijkl} \varepsilon_{kl} \quad (5.2)$$

where  $\varepsilon_{kl}$  is strain tensor. For cubic structure of Si and Ge crystals this tensorial equation can be put into the following matrix

$$\begin{pmatrix} \sigma_{xx} \\ \sigma_{yy} \\ \sigma_{zz} \\ \sigma_{yz} \\ \sigma_{zx} \\ \sigma_{xy} \end{pmatrix} = \begin{pmatrix} C_{11} & C_{12} & C_{12} & 0 & 0 & 0 \\ C_{12} & C_{11} & C_{12} & 0 & 0 & 0 \\ C_{12} & C_{12} & C_{11} & 0 & 0 & 0 \\ 0 & 0 & 0 & C_{44} & 0 & 0 \\ 0 & 0 & 0 & 0 & C_{44} & 0 \\ 0 & 0 & 0 & 0 & 0 & C_{44} \end{pmatrix} \begin{pmatrix} \varepsilon_{xx} \\ \varepsilon_{yy} \\ \varepsilon_{zz} \\ \varepsilon_{yz} \\ \varepsilon_{zx} \\ \varepsilon_{xy} \end{pmatrix} \quad (5.3)$$

Based on the elements of the matrix the elastic modulus (E) can be written as

$$\frac{1}{E} = \frac{C_{11} + C_{12}}{(C_{11} - C_{12}) \cdot (C_{11} + 2 \cdot C_{12})} - 2 \cdot \left( \frac{1}{C_{11} - C_{12}} - \frac{1}{2 \cdot C_{44}} \right) \cdot (n_x^2 n_y^2 + n_x^2 n_z^2 + n_z^2 n_y^2) \quad (5.4)$$

where the  $n_i$  ( $i = x, y, z$ ) are the projection of the unit vectors in the direction of the three coordinate axes. The magnitude of the linear elastic modulus depends on axes of the crystal. The calculated value of E along the three major axes of silicon and germanium are given in Table 5.1

Material	Elastic modulus (E)	< 100 >	< 110 >	< 111 >
silicon	(Mbar)	1.3016	1.6909	1.8781
germanium	(Mbar)	1.0295	1.3753	1.5518

**Table 5.1:** Elastic modulus of silicon and germanium at room temperature.

On the other hand, the relative change of length can be determined experimentally using the relation

$$\frac{\Delta L}{L} = \frac{D}{2R + D} \quad (5.5)$$

D and R are the thickness and radius of curvature of the sample, respectively.



### 5.3 Intrinsic silicon under tensile stress along the $\langle 110 \rangle$ direction.

One of the factors stimulating the present study of defects under the action of uniaxial stress was the measurable effect caused by the applied stress at the site of a substitutional probe atom. In an effort to test the reproducibility of this technique the probe atoms were implanted into thin intrinsic silicon sample. The sample was prepared from a  $100\ \mu\text{m}$  thick silicon wafer with a size of  $20\text{mm} \times 7\text{mm}$  and  $\langle 110 \rangle$  surface. The longer edge was chosen to lie along the  $\langle 110 \rangle$  crystal axis. The implantation was made exactly in the middle of the surface of the sample which allows to produce maximum tension on the implanted region. Before the sample was subjected to the external uniaxial stress, it was annealed at  $900^\circ\text{C}$  for 600s. The PAC time spectra taken without stress showed full anisotropy coefficient indicating that all probe nuclei occupy perfect substitutional sites in the host lattice (panel 1 of Figure 5.6a). It also suggests that the distribution of charges around the

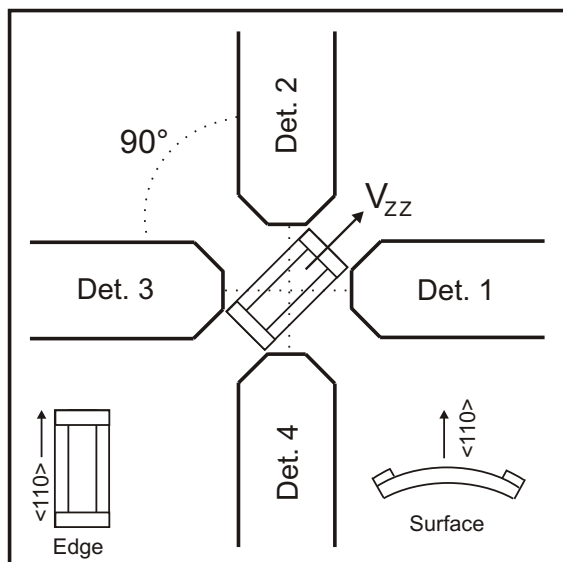


**Figure 5.5:** Schematic diagram of the detector arrangement for measuring the tension induced EFG in Raghavan geometry, where the main component of the EFG ( $V_{zz}$ ) lies in a detector plane and pointing exactly between two detectors situated at  $90^\circ$ .

probe atoms is symmetric, hence, no EFG is observed. By mounting the sample on a curved surface of  $43\text{mm}$  constant radius, which corresponds to a uniaxial tensile stress of  $1.81(4)$  kbar along  $\langle 110 \rangle$  crystal axis, a well defined interaction frequency of  $\nu_Q = 20(1)$  MHz  $\eta = 0.15(1)$  is measured (panel 2 of Figure 5.6a). This tension induced frequency is the result of the asymmetric charge distribution at the probe nuclei whose symmetry was broken by the external applied stress. It should be noted here that this measurement was taken in the so called Raghavan geometry,

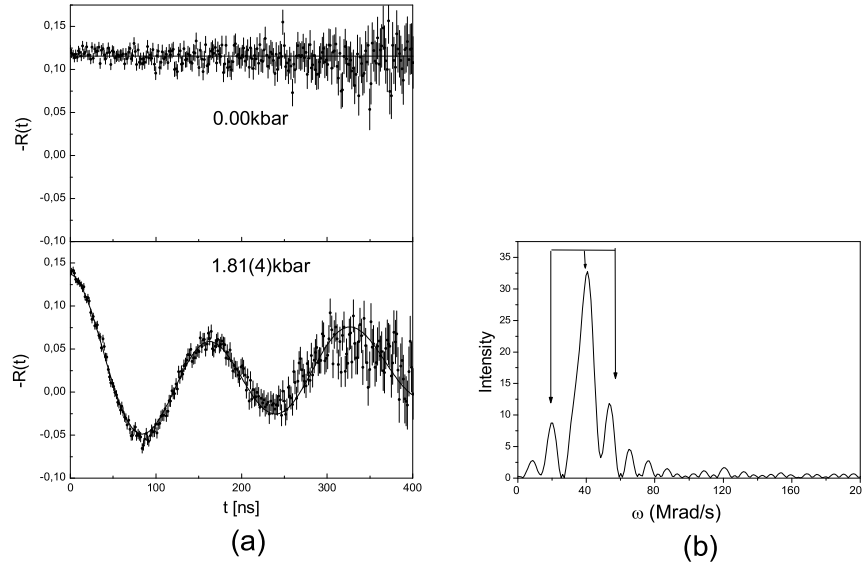


**Figure 5.6:** *Intrinsic silicon sample doped with  $^{111}\text{In}$  and annealed at  $900^\circ\text{C}$  for 600s. (a) Panel 2 shows well defined tension induced frequency of  $20(1)\text{MHz}$  by the application of  $1.81(4)\text{kbar}$  uniaxial tensile stress along  $\langle 110 \rangle$  (b) The corresponding Fourier transform of the frequency.*

where the second harmonic of the transition frequency ( $\omega_2$ ) was measured instead of the principal component  $\omega_1$ .

## 5.4 In-Sb pair under tensile stress

The thermal stability study of the In-Sb pair by Wichert et al. [WICH89] showed that the complex is formed near  $627^\circ\text{C}$  annealing temperature, its fractional population grows to a maximum near  $800^\circ\text{C}$  and dissociates afterwards. In the current measurements, the silicon sample was implanted with  $^{121}\text{Sb}$  ( $5 \times 10^{14}$  atoms/cm $^2$ , Energy = 120 keV). Annealing the sample at  $800^\circ\text{C}$  after the indium post-implantation leads to the appearance of a well defined interaction frequency on the measured PAC time spectra (panel 1 of Figure 5.7). The quadrupole coupling constant of this frequency is  $\nu_Q = 271(1)\text{MHz}$   $\eta = 0.0$ , it is identical with the frequency reported in the literature. The maximum fractional population of the indium-antimony pair detected here is  $f_1 = 25(2)\%$ . About  $f_0 = 55(2)\%$  of the probe atoms remain in undisturbed substitutional lattice locations. The PAC time spectrum taken without external stress was fitted by taking  $19(2)\%$  of Sb free substitutional probe atoms be subjected to a weak EFG. These probes account for the low frequency modulation in the time spectrum (see panel 1 Figure 5.7). It is most probably due to the internal strain caused by the implantation of an oversized Sb atoms in silicon and/or the heterogenous lattice structure formed during the recrystallization process.

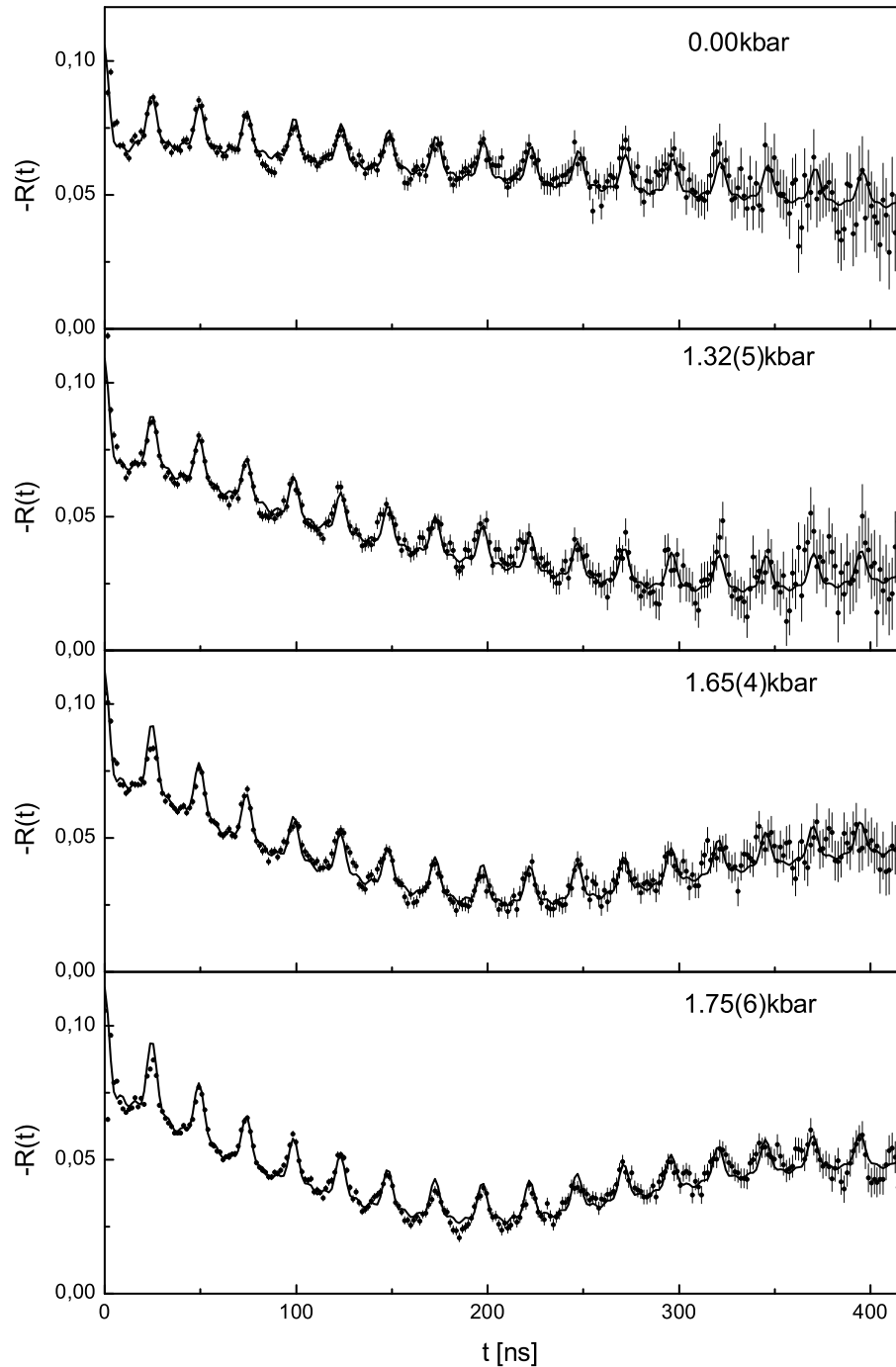


**Figure 5.7:** *In-Sb pair in silicon under the influence of uniaxial tensile stress along  $\langle 110 \rangle$*

Consequently, measurements were also taken under different values of uniaxial stress. The sample was placed between two cylinder heads whose long edge coincides with the  $\langle 110 \rangle$  crystal axis, which allows the transmission of uniaxial stress in the same axis to the sites of the probe nuclei. Moreover, the detectors are

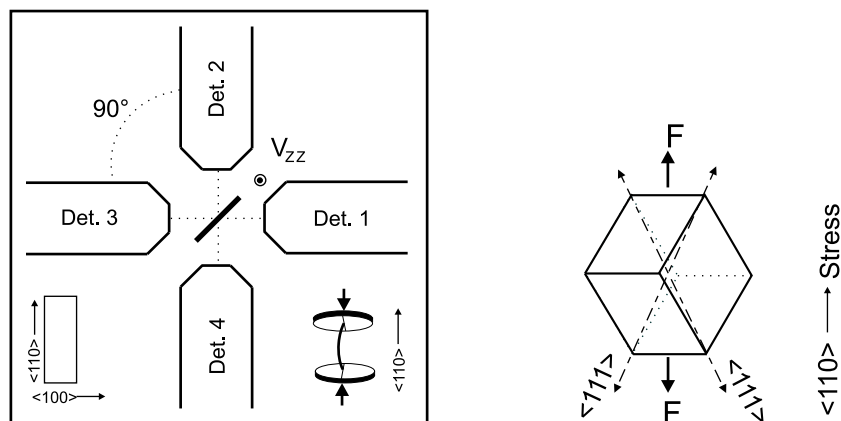


**Figure 5.8:** Schematic diagram of the detectors arrangement for measurements under uniaxial tensile stress. The main component of tension induced EFG ( $V_{zz}$ ) lie perpendicular to the detectors plane. The right side shows the direction of the stress at probe site

arranged in such a way that the tension induced electric field gradient lies perpendicular to the detector plane (Figure 5.8). By this geometry, one measures the first component of the transition frequency  $\omega_1$ . All detector are aligned  $10^\circ$  off axis from  $\langle 111 \rangle$  crystal orientation. This position has no influence on the magnitude of the EFG but plays an important role when information is derived about the direction of

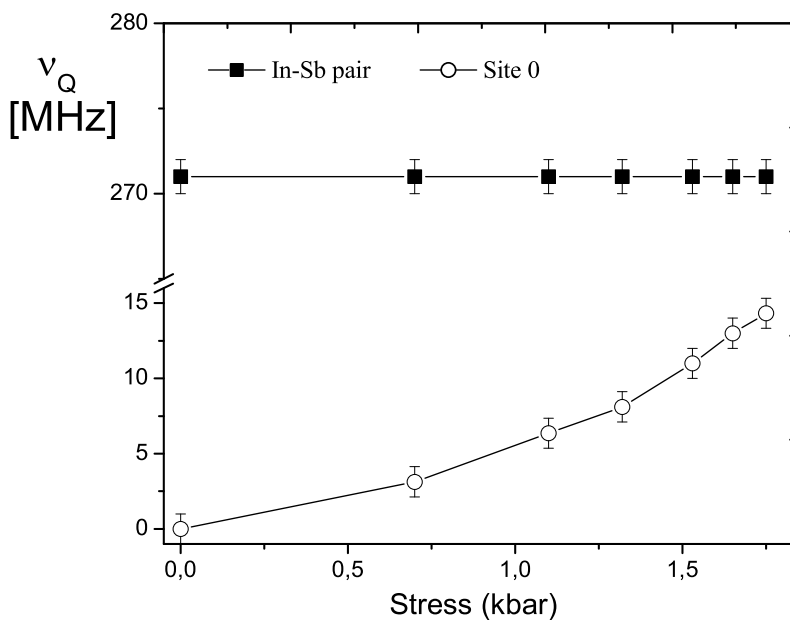


**Figure 5.9:** Interaction frequency of the In-Sb pair and tension induced frequency from site 0 in silicon for different value of applied stress.

the EFG with respect to the host lattice. However, the structures of the pairs were identified by another independent measurements, therefore, the primary goal of this experiment is to investigate the effect of external stress on the magnitude of the associated EFGs. The time spectra are taken successively for different magnitudes of uniaxial tensile stress (panel 2 to 4 of Figure 5.7). In panel 2, one can clearly see the development of a new frequency as the result of the action of the applied stress. At a stress value of 1.32 kbar, for instance, this slowly varying frequency has

In-Sb and other complexes	Uniaxial tensile stress along $\langle 110 \rangle$					
	0.75kbar	1.10kbar	1.32kbar	1.55kbar	1.65kbar	1.75kbar
$\nu_{Q1}(\text{InSb}_1)[\text{MHz}](\text{site1})$	271(1)	271(1)	271(1)	271(1)	271(1)	271(1)
$\delta_1$	0.15(7)	0.20(5)	0.20(5)	0.20(5)	0.20(5)	0.20(5)
$\eta_1$	0.0	0.0	0.0	0.0	0.0	0.0
$f_1[\%]$	25(2)	25(2)	25(2)	25(2)	25(2)	25(2)
$\nu_{Q0}(\text{Sub. indium})[\text{MHz}](\text{site0})$	2.80(1)	6.40(1)	8.51(1)	11.10(1)	13.12(1)	14.47(1)
$\delta_0$	28(3)	33(5)	28(2)	28(2)	27(2)	26(2)
$\eta_0$	0.17(3)	0.22(5)	0.27(3)	0.30(4)	0.30(3)	0.30(2)
$f_0[\%]$	35(3)	35(2)	35(2)	35(3)	35(3)	35(3)
$\nu_{Q01}(\text{Imp. Sub. indium})[\text{MHz}]$	0.0(1)	0.0(1)	0.0(1)	0.0(1)	0.0(1)	0.0(1)
$\delta_{01}$	0.0	0.0	0.0	0.0	0.0	0.0
$f_{01}[\%]$	19(2)	19(2)	19(2)	19(2)	19(2)	19(2)
Poly crystalline fraction						
$f_p[\%]$	21(2)	21(1)	21(1)	21(1)	21(1)	21(2)
Additive constant	-0.015(6)	-0.014(5)	-0.013(5)	-0.011(3)	-0.009(3)	-0.0075(2)

**Table 5.2:** Fit results of In-Sb pair under uniaxial tensile stress along  $\langle 110 \rangle$  in silicon

a magnitude of 8.51(1) MHz modulating the entire spectrum. This tension induced frequency is detected from the fractional population  $f_0$  of site 0 (see Figure 4.5), where substitutional probes occupy lattice sites surrounded by host atoms. The magnitude of this tension induced frequency increases with the value of external applied stress (Figure 5.9). On the other hand, there were no evidence of the effect of external stress on other fractions of the probe atoms in the sample. For instance, the frequency associated with the In-Sb pair remains unaffected by the stress to the knowledge beyond the error limit. This indicates that a new mechanical property has been created in the region containing the complex which hinders the transmission of the stress to the probe sites.

## 5.5 In-As pair under compressional uniaxial stress

Figure 5.10 shows the PAC time spectra taken from an arsenic implanted silicon sample. The silicon sample was implanted with  $^{75}\text{As}$  (Dose:  $4 \times 10^{14}$  atoms/cm<sup>2</sup>; 120 keV), and then it was annealed at 800°C for 600s before coincidence time spectra were taken. The first panel of Figure 5.10 shows well defined quadrupole interaction frequencies  $\nu_{Q1} = 229(1)\text{MHz}$  ( $\eta = 0$ ) and  $\nu_{Q2} = 239(1)\text{MHz}$  ( $\eta = 0.65$ ).

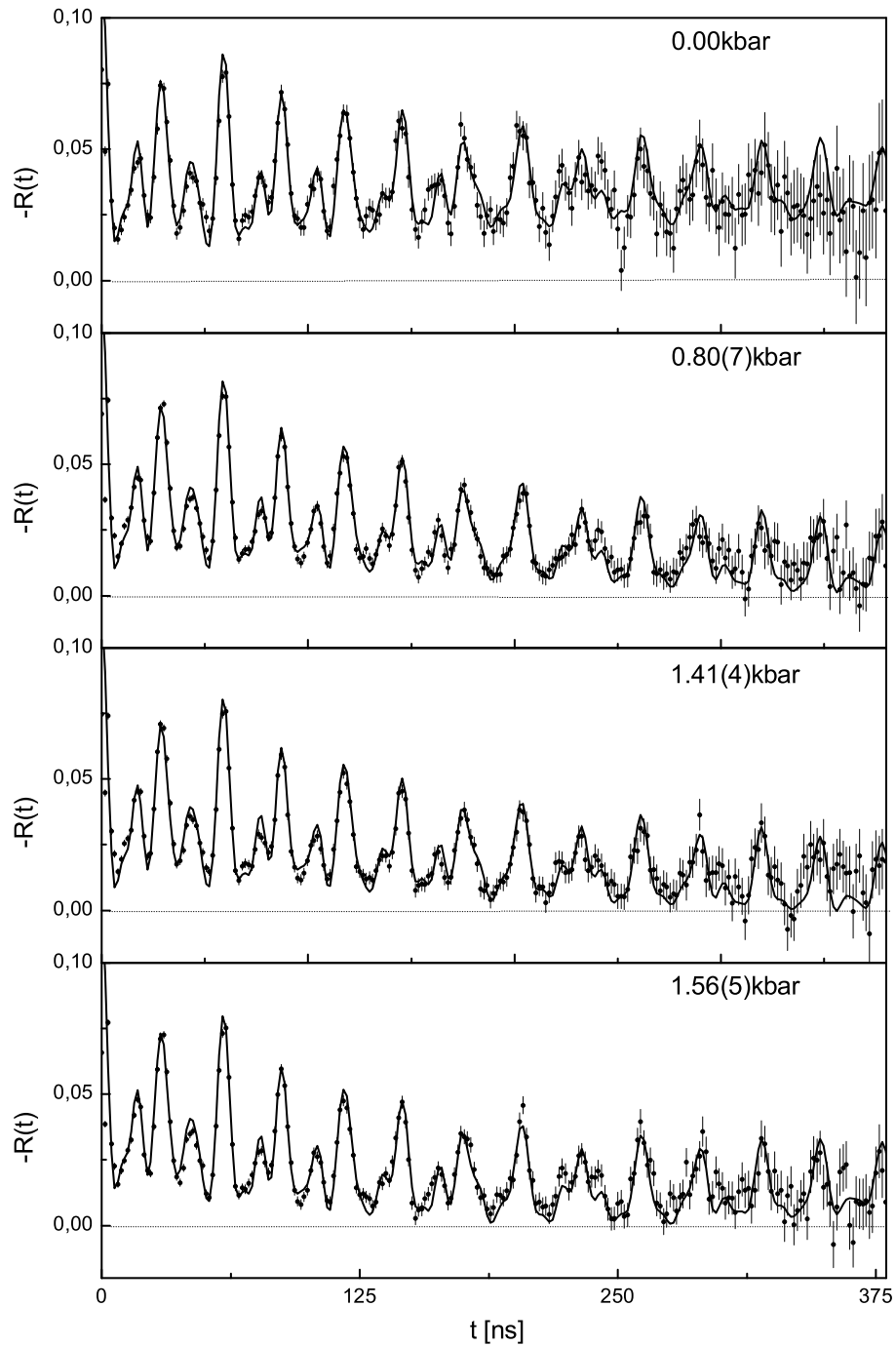


**Figure 5.10:** *In-As pair in silicon under the influence of uniaxial compressional stress along  $\langle 110 \rangle$*

The frequencies are associated with the interaction of indium with pre-implanted arsenic atoms. Exceptionally, the fractional population of the In-As pairs were extremely high compared to other donor species in silicon. After annealing the sample at  $800^\circ\text{C}$  a fractional population of  $f_1 = 43(2)\%$  of InAs<sub>1</sub> pair (site 1) and

$f_2 = 23(2)\%$  of the  $\text{InAs}_2$  (site 2) are measured. The fraction  $f_0 = 21(3)\%$  of the probe atoms possess an undisturbed substitutional sites in the host lattice. When the sample is subjected to the external uniaxial compressional stress, the entire spectrum has been modulated by a slowly varying frequency (panel 2 of Figure 5.10). A frequency of  $3.35(1)$  MHz was detected at  $0.80(3)$  kbar. This frequency is once again the result of the distortion of the cubic symmetry of the indium environment (site 0) by the applied stress. It is exactly the same situation as in the case of the Sb doped sample. In the As doped sample, the fractional population of this site ( $f_0$ ) is relatively small compared to  $35(3)\%$  in the Sb implanted sample, as a consequence, the amplitude of the frequency modulation is small in the arsenic doped silicon. The magnitude of the tension induced frequency on  $f_0$  increases with the value of external applied stress as shown in Figure 5.11. This tension induced  $\nu_Q$  varies roughly linear with applied uniaxial stress. A maximum value of  $8.6(1)$  MHz is attained at  $1.56(5)$  kbar. The rest of the populations of the probe atoms do not show any response at all values of the stress. The interaction frequencies of the complexes containing  $^{111}\text{In}$  and As remain unchanged by the applied stress. The only effect that has been seen was slight variation of the asymmetry parameter ( $\eta \simeq 0.06(3)$ ) on the  $\text{InAs}_1$  complex. When we are looking to the other parameters of the tension induced EFG of site 0, the values of the frequency damping are relatively high in general indicating a large width of the frequency distribution around the

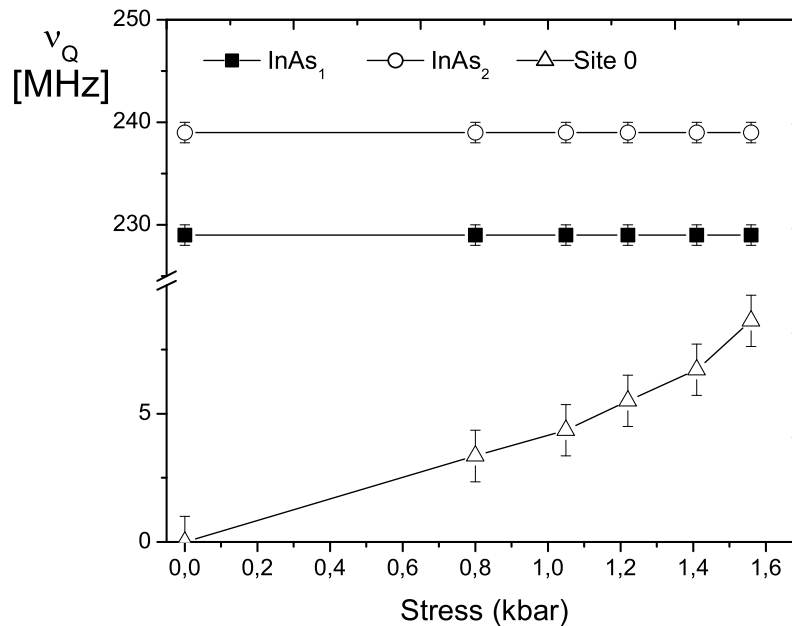


**Figure 5.11:** The result of the action of uniaxial stress along  $\langle 110 \rangle$  crystal axis on the different complexes of arsenic doped silicon sample. The interaction frequencies of  $\text{In-As}_x$  complexes remain unchanged but tension induced frequency from donor free substitutional fraction ( $f_0$ ) increases with the value of stress.

In-As and other complexes	Uniaxial tensile stress along $\langle 110 \rangle$					
	0.0kbar	0.80kbar	1.05kbar	1.22kbar	1.41kbar	1.56kbar
$\nu_{Q1}(\text{InAs}_1)$ [MHz](site1)	229(1)	229(1)	229(1)	229(1)	229(1)	229(1)
$\delta_1$	0.58(6)	0.55(6)	0.55(6)	0.55(6)	0.55(6)	0.55(6)
$\eta_1$	0.0	0.01(2)	0.03(1)	0.06(3)	0.05(2)	0.05(3)
$f_1$ [%]	43(2)	43(2)	43(2)	43(2)	43(2)	43(2)
$\nu_{Q2}(\text{InAs}_2)$ [MHz](site2)	239(1)	239(1)	239(1)	239(1)	239(1)	239(1)
$\delta_2$	1.15(6)	1.15(6)	1.25(6)	1.25(6)	1.25(6)	1.25(6)
$\eta_2$	0.65	0.65	0.65	0.65	0.65	0.65
$f_2$ [%]	23(2)	23(2)	23(2)	23(2)	23(2)	23(2)
$\nu_{Q0}(\text{Sub. indium})$ [MHz](site0)	0.0	3.35(1)	4.35(1)	5.5(1)	6.71(1)	8.62(1)
$\delta_0$	0.0	25(3)	27(4)	36(3)	40(2)	42(2)
$\eta_0$	0.0	0.12	0.15	0.18	0.22	0.24
$f_0$ [%]	21(2)	21(3)	21(2)	21(2)	21(3)	21(3)
Poly crystalline fraction						
$f_p$ [%]	13(2)	13(2)	13(2)	13(2)	13(2)	13(2)
Additive constant	-0.0043(5)	-0.0042(4)	-0.0060(2)	-0.0046(5)	-0.0036(4)	-0.0019(2)

**Table 5.3:** Fit results of In-As pair under uniaxial tensile stress along the  $\langle 110 \rangle$  crystal axis in silicon.

mean value. It is suggesting the nonuniform environments of the implanted region.

## 5.6 Uniaxial compressional stress on In-Te pair

The pairing of indium with tellurium in silicon is detected for the first time in this work. It is the only frequency reported so far for an indium-double donor pair in silicon. According to the discussion given Chapter 4, tellurium occupies presumably octahedral interstitial site in silicon at high dose Te implantation. Like group V donors presented in the last sections, the In-Te pair is also studied under the action of uniaxial stress. A tellurium (dose of  $1 \times 10^{15}$  atoms/cm<sup>2</sup>, 40 keV) was implanted in silicon followed by annealing the sample at 400°C and 700°C for 600s consecutively. Figure 5.12 shows the PAC time spectra of the In-Te complex in silicon under different values of uniaxial stress. Panel 1 of Figure 5.12 shows the interaction frequency of the complex whose quadrupole coupling constant is 444(1) MHz ( $\eta = 0$ ). This frequency is clean from low noise signal and sharply defined with narrow width of the frequency distribution ( $\delta_1 = 0.15$ ). The fractional population of this pair is  $f_1 = 31(2)\%$  for this sample. The population of  $f_0 = 33(2)\%$  occupy perfect substitutional lattice sites. The fraction  $f_p = 26(2)\%$  of the probe atoms are in undefined lattice location. By applying uniaxial compressional stress of 0.91(5) kbar one can see clearly a low frequency modulation on the time spectrum (panel 2 of Figure 5.12). A tension induced frequency of 7.4(1) MHz is derived from this spectrum. This low frequency modulation is the effect of external stress on donor free substitutional indium ( $f_0$ ). The distribution around mean value of the frequency is very wide, a damping value of  $\delta_0 = 40(3)$  is measured for this stress. The magnitude of this tension induced frequency of site 0 increases with applied stress, a maximum of 18.3(1) MHz is detected at 1.82(6) kbar. The effect of stress



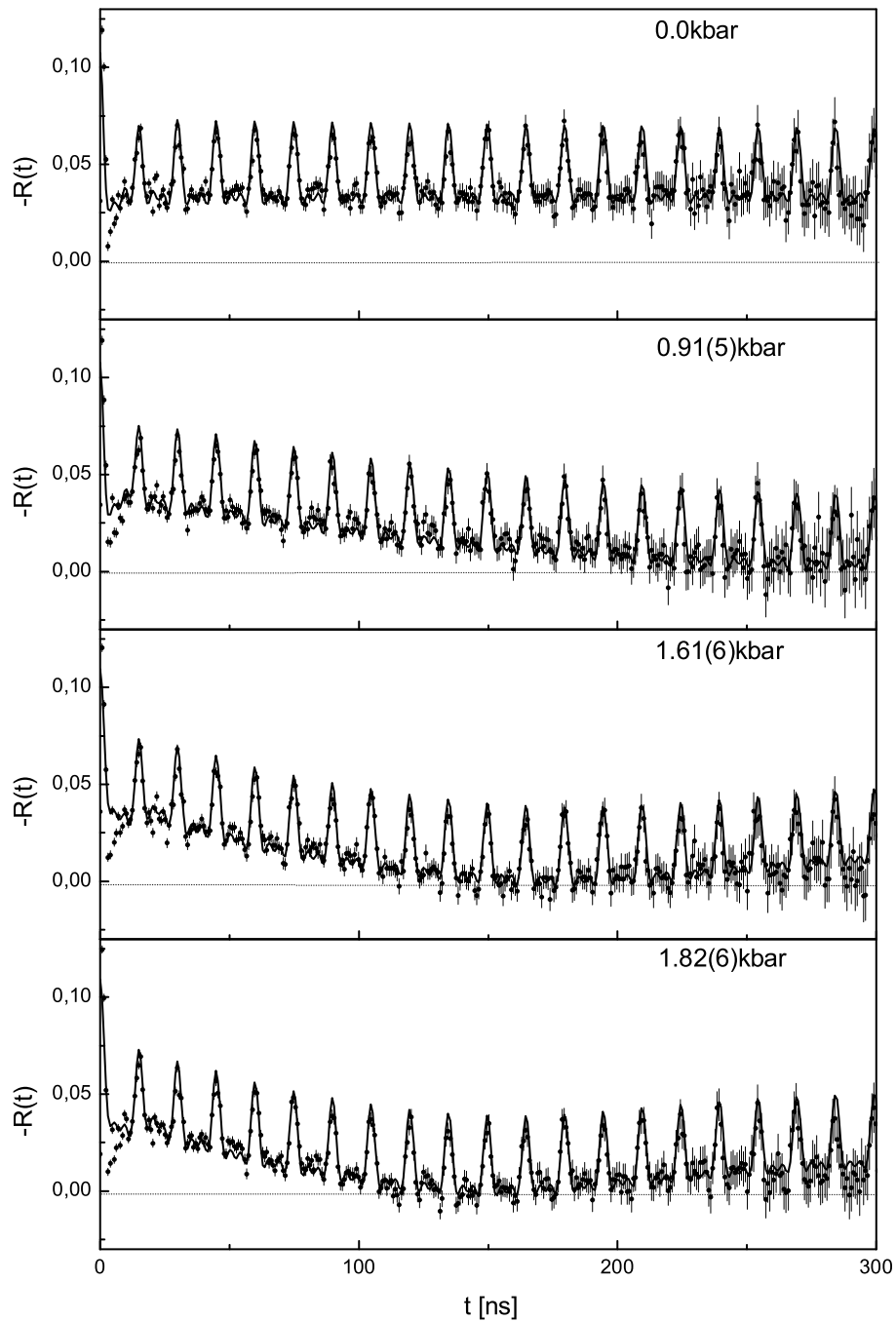


**Figure 5.12:** *In-Te pair in silicon under the influence of uniaxial compressional stress along  $\langle 110 \rangle$  crystal axis.*

on the other fractions of the probe atoms is similar to the previous sections. The analysis of the data showed no measurable change in the interaction frequency of the In-Te pair, even at the maximum possible value of the stress. This suggests that the complex containing indium and tellurium remains unchanged by applied compressional uniaxial stress. The best fit to the data is obtained by considering  $f_{01}$

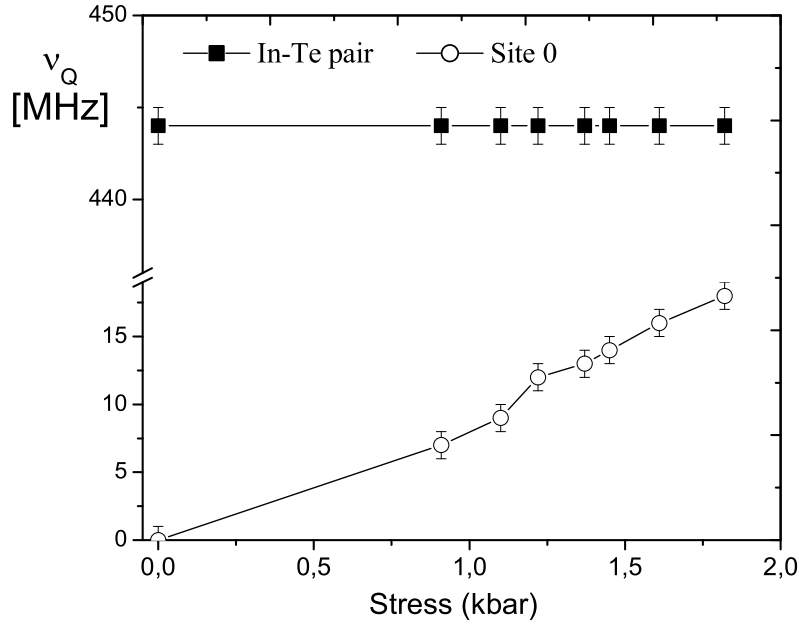


**Figure 5.13:** *In-Te pair in silicon under the influence of uniaxial compressional stress along  $\langle 110 \rangle$*

= (10-15)% of the substitutional probe atoms be unaffected by the external stress (see Table 5.4). Possible reasons shall be given in the discussion.

In-Te and other complexes	Uniaxial tensile stress along $\langle 110 \rangle$						
	0.91kbar	1.10kbar	1.22kbar	1.37kbar	1.45kbar	1.61kbar	1.82kbar
$\nu_{Q1}(\text{InTe}_1)$ [MHz](site1)	444(1)	444(1)	444(1)	444(1)	444(1)	444(1)	444(1)
$\delta_1$	0.15(6)	0.15(6)	0.15(6)	0.15(6)	0.15(6)	0.15(6)	0.15(6)
$\eta_1$	0.0	0.0	0.0	0.0	0.0	0.0	0.0
$f_1$ [%]	31(2)	31(2)	31(2)	31(2)	31(2)	31(2)	31(2)
$\nu_{Q0}(\text{Sub. indium})$ [MHz](site0)	7.4(1)	9.5(1)	12.2(1)	13.2(1)	14.15(1)	15.8(1)	18.3(1)
$\delta_0$	40(3)	44(5)	38(2)	35(2)	28(3)	28(2)	28(2)
$\eta_0$	0.0	0.0	0.0	0.0	0.0	0.0	0.0
$f_0$ [%]	33(2)	31(2)	28(3)	28(3)	28(3)	28(3)	28(3)
(Sub. indium)[MHz](site0)	0.0	0.0	0.0	0.0	0.0	0.0	0.0
$\delta_{01}$	0.02	0.02	0.02	0.02	0.02	0.02	0.02
$f_{01}$ [%]	10(2)	12(3)	15(2)	15(2)	15(3)	15(3)	15(3)
Poly crystalline fraction							
$f_p$ [%]	26(3)	26(2)	26(1)	26(1)	26(1)	26(1)	26(2)
Additive constant	-0.014(5)	-0.007(2)	-0.009(3)	-0.008(2)	-0.009(1)	-0.008(3)	-0.008(2)

**Table 5.4:** *Fit results of In-Te pair under uniaxial compressional stress along  $\langle 110 \rangle$  in silicon*

## 5.7 Uniaxial stress on In-P pair

A silicon sample was implanted with phosphorous a dose of  $2 \times 10^{14}$  atoms/cm<sup>2</sup> and an energy 60 keV. After the post-implantation of indium, the sample was annealed at 900°C for 600 s and 700°C for 50 minutes respectively. The PAC time spectra taken after annealing show a well defined interaction frequency associated with the presence of phosphorous in the sample (panel 1 of Figure 5.14). The analysis of the data yield an interaction frequency of  $\nu_Q = 179(1)$  MHz  $\eta = 0$  representing the In-P pair in silicon (see Chapter 4). The In-P complex accounts for  $f_1 = 26(2)\%$  of the probe atoms in the sample. The majority of the probe atoms ( $f_0 = 51(3)\%$ ) occupy phosphorous free perfect substitutional sites in the substrate lattice (site 0). The time spectra are taken successively under different values of uniaxial tensile stress (panel 2 - 4 of Figure 5.14). The spectra in each panel look very similar indicating that no detectable change has taken place on both In-P complex and the donor free substitutional site of the probe atoms for stress value as high as 1.81(6)kbar. Least square fits to the data show indeed no variation of the parameters within the error margin. The most interesting part of this experiment is the absence of a tension induced frequency on site 0. Despite the majority of the probe atoms possess perfect substitutional lattice location in the sample, no indication of the effect of external stress is observed. This shows that no lattice relaxation has taken

In-P and other complexes	Uniaxial tensile stress along $\langle 110 \rangle$			
	0.00kbar	1.31kbar	1.50kbar	1.81kbar
$\nu_{Q1}(\text{InP}_1)[\text{MHz}](\text{site1})$	179(1)	179(1)	179(1)	179(1)
$\delta_1$	0.15(6)	0.18(3)	0.18(3)	0.18(3)
$\eta_1$	0.0	0.0	0.0	0.0
$f_1[\%]$	26(2)	26(2)	26(2)	26(2)
(Sub. indium)[MHz](site0)	0.0	0.0	0.0	0.0
$\delta_0$	0.0	0.0	0.0	0.0
$f_0[\%]$	51(2)	51(2)	51(3)	51(3)
$\nu_{Q01}(\text{imper. Sub. indium})[\text{MHz}]$	4.04(1)	5.04(1)	4.96(1)	5.30(1)
$\delta_{01}$	10.0	10.0	10.0	10.0
$\eta_{01}$	0.05	0.05	0.05	0.05
$f_{01}[\%]$	15(2)	15(2)	15(2)	15(2)
Polycrystalline fraction				
$f_p[\%]$	8(1)	8(1)	8(1)	8(1)
Additive constant	-0.016(3)	-0.013(2)	-0.016(3)	-0.017(2)

**Table 5.5:** Fit results of In-P pair under uniaxial tensile stress along  $\langle 110 \rangle$  in silicon

place at the site of the probe atoms. In other words, the sample could have lost its elastic property by the phosphorous implantation.

This unexpected effect is a clear indication of the different nature of phosphorous implanted region of silicon as compared to the implantation of antimony and arsenic

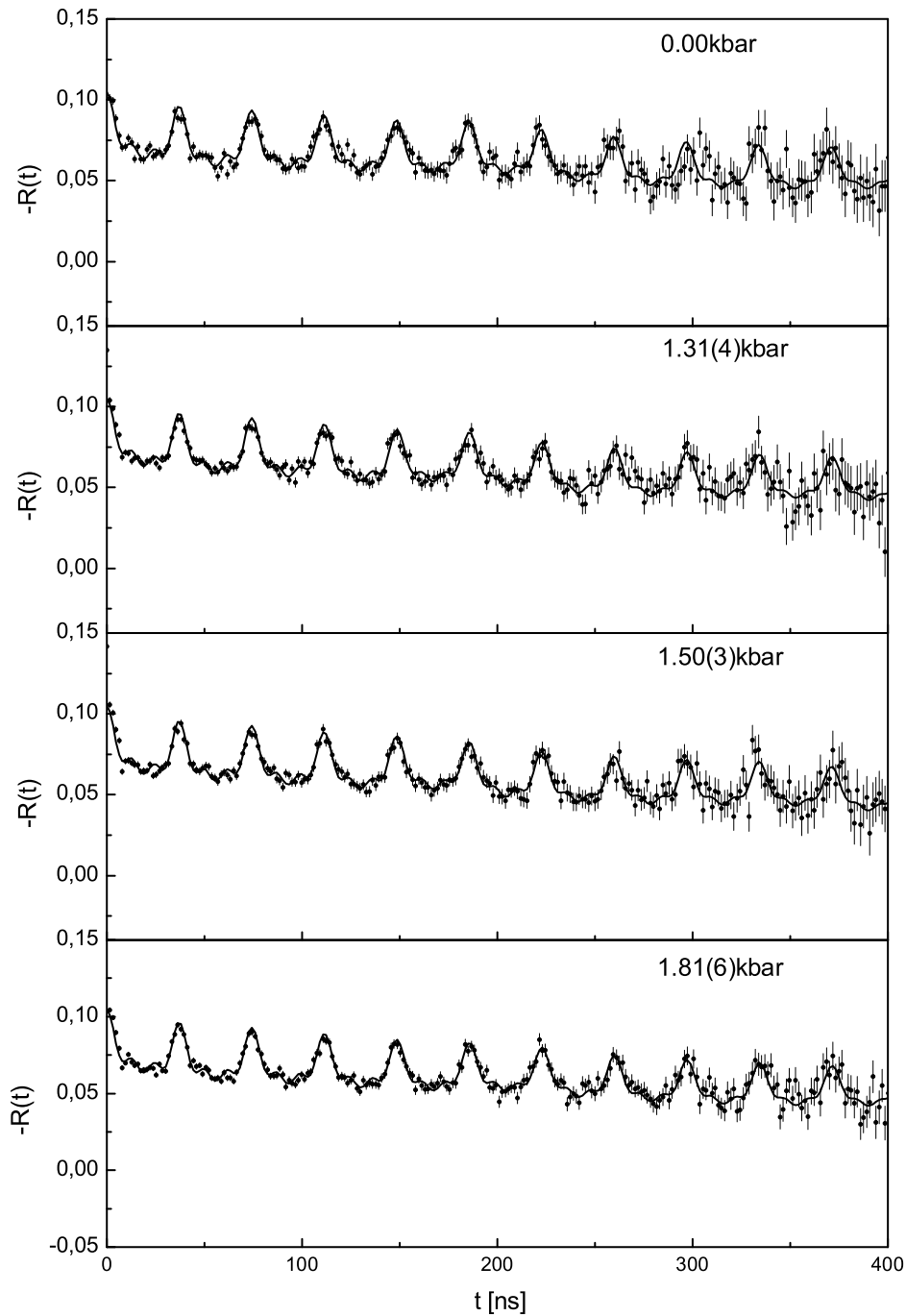


**Figure 5.14:** *In-P* pair in silicon under the influence of uniaxial tensile stress along  $\langle 110 \rangle$  crystal axis.

atoms. Moreover, the best fit to the data taken without external stress was obtained by taking into account 15(2)% of the probes in a non perfect cubic environment subjected to a weak EFG due to lattice imperfections. This can be explained by the formation of heterogeneous surface lattice structure in the implanted region of the sample.

## 5.8 Discussion of the results

The experimental investigations of the indium-donor pairs under the action of uniaxial stress are presented in the last sections. The results show that the influence of the external stress on the implanted silicon varies with the type of donor atoms used. This can be inferred from the response of the probe atoms situated at different complexes in the samples. In all the measurements, the fraction of probe atoms paired with donors in silicon maintain consistent behavior by being completely insensitive to the external stress. Detectable effects of the applied stress are observed from the population of probes surrounded by host atoms (site 0). The tension induced frequency from this site roughly increases linear with the applied stress as shown in Figure 5.15. It is also evident in the figure that there are different slopes of the lines passing through the data points. This suggests that the magnitude of the stress induced frequency depends on the size of the donor atoms incorporated into the samples. High value of frequency is measured from the silicon sample doped with largest donor atom. In fact, site 0 is free from donors as nearest neighbor and should have identical response to the same value of stress regardless of the existence of other impurities. However, the observed variation is most likely the effect of the presence of various donor atoms in the bulk silicon.

In most of the cases, the tension induced frequencies are accompanied by high values of the frequency damping ranging from about  $\delta_0 = 10$  to 45. This large width of the frequency distribution in PAC normally is the result of either static fluctuation of the EFG or a dynamic process that take place at the site of the probe atoms during the measurements. In each cases, there are typical pattern that can be seen on the time spectra [SKUD92]. When there is static fluctuation of the EFG, the frequency damping will be followed by a varied width of the amplitude of the frequency peaks. Whereas in dynamic process no change in the width of the frequency peak is expected following the damping. But, it is difficult here to verify any of them because the tension induced frequencies are very low, and the observed number of frequency peaks are less than two which makes a comparison impossible. However, dynamic behavior is less likely to occur in these measurements, because we are dealing with large substitutional impurities which are not expected to jump from one lattice site to the other at room temperature in a completely occupied surrounding.

In general, there are three points to be raised from the results of the current experiments.

- First, why the complexes containing indium and donor atoms are not responding to the external stress?
- Second, why stress induced frequencies from donor free substitutional sites are highly damped?

- Third, why the mechanical property of phosphorous implanted silicon is different?

To begin with the first, this group belongs to the complexes containing indium and donor atoms in silicon. The pairs have been detected by an independent measurements, and they are characterized by respective unique interaction frequencies. Indium has an atomic radius of  $1.63\text{\AA}$  [DEAN79] much larger than silicon atom. The presence of an indium at a lattice site in silicon creates high strain fields in the surrounding. Therefore, one can expect that an additional oversized atom next

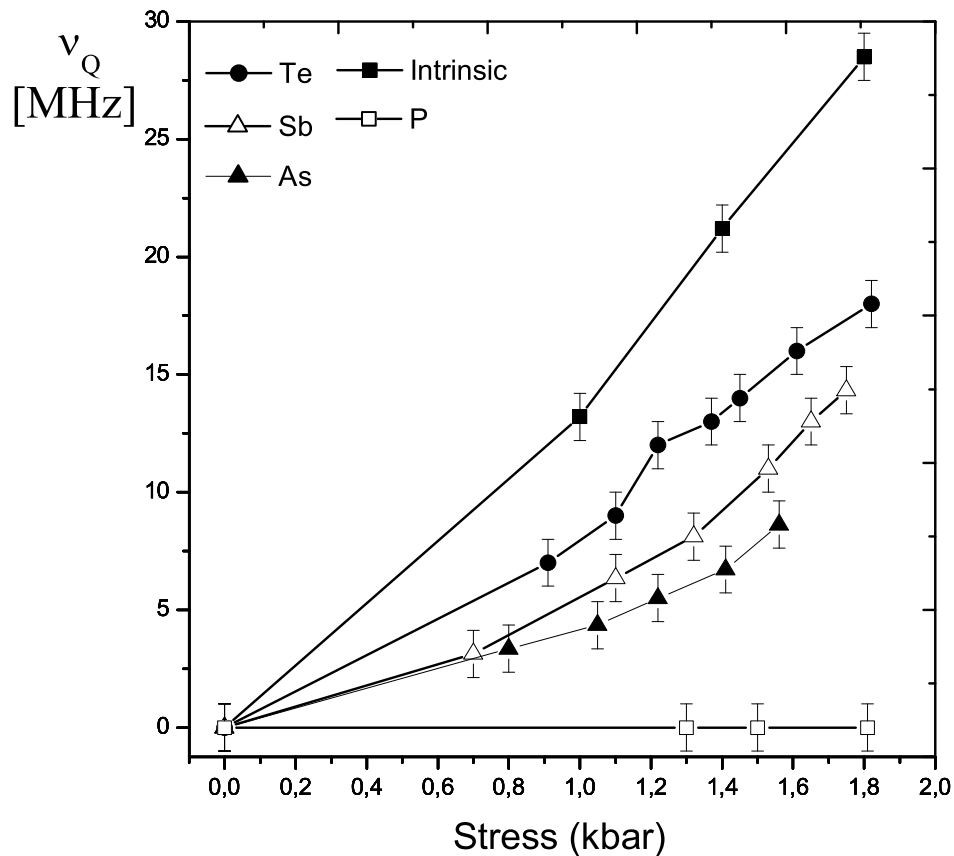


**Figure 5.15:** Stress induced frequencies at site 0 by an external uniaxial stress along  $\langle 110 \rangle$  crystal axis, after various donor implantations in silicon.

to an indium would produce even higher strain field near the complex. Moreover, the maximum lattice relaxation possible by the external stress is only 0.1% of the lattice constant. But, donor atoms like As or Sb next to an indium relax the lattice much larger than induced externally M. Settler [SETT99]. Therefore, the presence of high strain fields prevents further lattice relaxation by external stress around the complexes. As the result, no measurable change of the quadrupole interaction frequency is observed from an indium-donor pairs for all the impurities tested so far.

The second point is the response of the donor free substitutional fraction of the probe atoms (site 0). The main results from this site are an increasing value of tension induced EFG with external stress and high frequency damping. The tendency of the EFG to increase with the stress is in agreement with previous measurements by G. Marx [MARX95]. However, according to the results from the present experiment the response to the applied stress varies with the kind of donor atoms incorporated in the samples (see Figure 5.15). The frequency values of the intrinsic silicon are taken from the work of G. Marx in the figure for comparison with the donor doped samples. The values of these frequencies are higher than those obtained from donor doped samples for all values of the stress. It is also clearly seen in the figure that the magnitude of the stress induced frequency decreases with the size of the donor atoms used in silicon. This trend of response of the probe atoms fails to hold in the case of phosphorous doped sample. Despite the fact that phosphorous accounts for

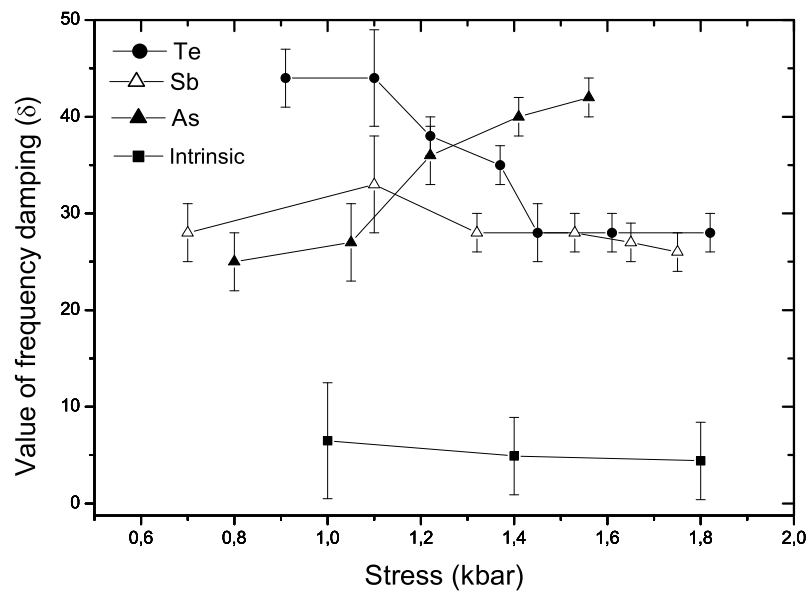


**Figure 5.16:** *The values of damping for stress induced frequencies of site 0 in impurity doped silicon.*

the lowest donor concentration used, no detectable change has occurred at the sites of all probe atoms in the sample. This suggests that the sample presumably changes its elastic property by phosphorous implantation.

The frequency damping measured from stress induced frequencies of site 0 is generally very high (see Figure 5.16). Maximum value of  $\delta_0 = 44$  is observed in tellurium doped silicon. In most cases, the values of damping show the tendency to decrease with increasing value of stress. However, it increases in the case of arsenic doped silicon, where the population of site 0 is the lowest. Figure 5.16 shows a difference

of about 20 in the values of damping between intrinsic and donor implanted samples. This can be expected because the donor implanted samples sustain additional radiation damage from the second implantation. Besides, the involvement of the various impurities in the substrate lattice during crystal regrowth could lead to the formation of inhomogeneous surface structure. The existence of such heterogenous lattice structure can cause static fluctuation of the EFG of the same complexes. For instance, probe atoms may occupy lattice site surrounded by far sited defects whose presence in the vicinity of the probe slightly vary perfect lattice ordering. It is also possible that probes take sites at the edge of dislocations (see Appendix D). The occurrence of such kind of environments can prevent identical response of the same complexes to an external applied stress. Which in turn leads to large width of EFG distribution around the mean value or large frequency damping. Moreover, the probe atoms are implanted in the samples to the depth nearly  $800\text{\AA}$  below the surface. Because of the curved nature of the stressed samples, there exists a stress gradient which varies radially from neutral fiber zone towards the surface (Figure 5.4 (b)). Consequently, probes on the surface are comparatively more stressed than those on the bottom of the implanted layer. Hence, the action of the external stress

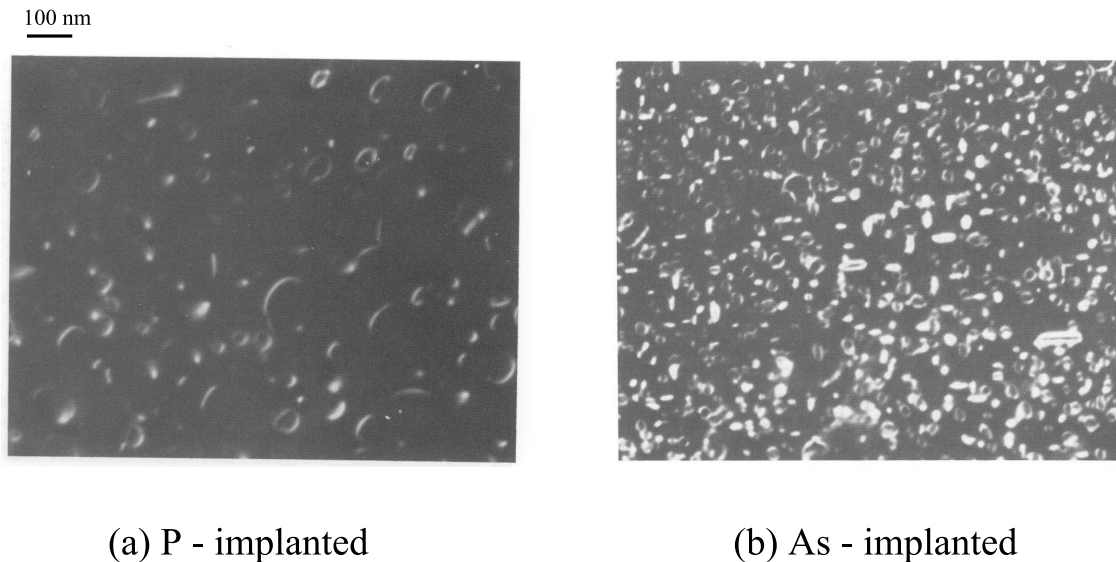


**Figure 5.17:** Plane view of transmission electron micrograph (TEM) of (a) phosphorous and (b) arsenic implanted silicon after annealing the samples at  $900^{\circ}\text{C}$  for 30 minutes [PRUS87] [KEVI87].

slightly differs across the probe atoms causing small deviations of the EFGs which contribute to the width of the frequency distribution. This is another possible reason leading to static distribution of the EFG.

The existence of heterogenous lattice structures are observed by transmission electron micrograph (TEM) by [PRUS87] [KEVI87] in arsenic and phosphorous im-



planted silicon samples. The degree of inhomogeneity of the lattice structure depends on damage sustained by the sample during implantation. Which is of course directly related with the dose, energy and the kind of impurity atom used. Figure 5.17 shows the TEM micrograph of phosphorous and arsenic implanted samples with equal dose of ( $5 \times 10^{15}$  atoms/cm<sup>2</sup>), energy 50 keV and 100 keV respectively. The plane view of the micrograph were taken after annealing the samples at 900°C for 30 minutes. In both cases several dislocation loops are observed. However, the size of dislocation loops in P implanted samples are larger than As. The same difference has also been observed, in the cross-sectional view of the micrographs, on the size of dislocations beneath the surface. Such size difference of the dislocations might have some association to the differences seen in the present experiments (Figure 5.15), on the mechanical properties of donor doped silicon. Nevertheless, this is an additional evidence to the existence of heterogenous structure in the implanted region.

In general, the large value of damping has significant influence on the frequency pattern of the time spectra. Its impact on the weak frequencies like the one measured under the action of uniaxial stress is clearly seen in the previous sections of this chapter. A tension induced frequency of 16 MHz was simulated to emerge out of

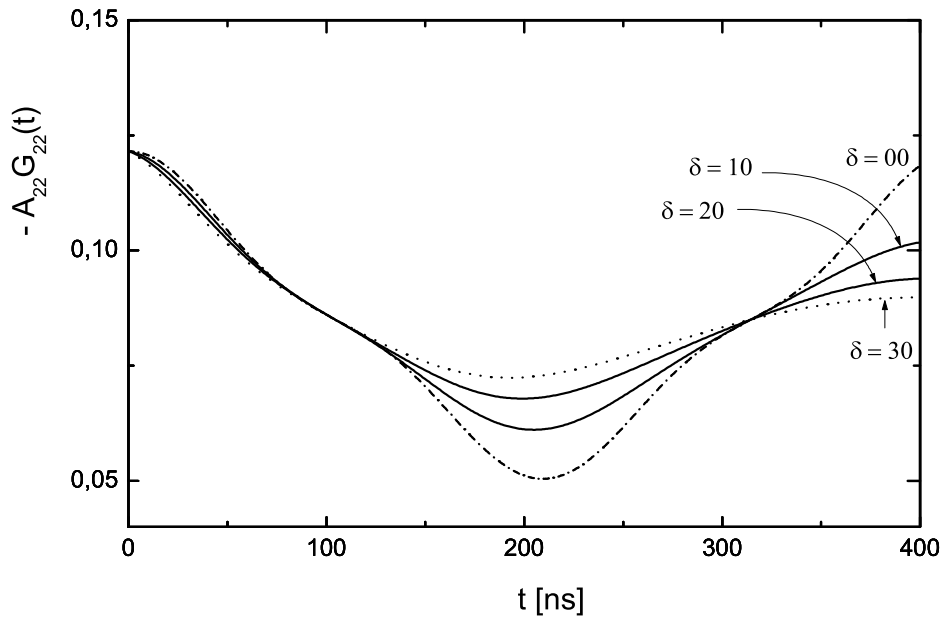


**Figure 5.18:** The QI frequency of 16 MHz is simulated to 30% population of the probe atoms. The figure shows drastic change of the amplitude of modulation with the value of damping.

30% of probe atoms subject to external uniaxial stress. The amplitude of the second

antinode of the modulation decreases by nearly 70% for  $\delta = 30$  (see Figure 5.18). The influence of damping is even high for small population of the probe atoms and weaker frequencies. The PAC time spectra presented in the last sections are the superposition of the various frequencies detected from the samples.

The third point of discussion is the different elastic response of silicon to the external stress as a result of phosphorous implantation. This can be compared by referring to only the response of donor free substitutional sites (site 0) (see Figure 5.15) in the samples. On the microscopic scale the response of these sites should have been similar regardless of the presence of impurity atoms elsewhere in the sample, because, all samples are prepared from the same silicon wafer and treated under the same conditions. The presence of impurity in the sample often would change the mechanical property the bulk silicon, and hence it hinders the transmission of uniaxial stress to the lattice sites. However, a complete lose of elasticity is not expected by the chosen impurities and implantation parameters. The absence of a tension induced frequency from the phosphorous doped sample suggests that no lattice relaxation has taken place at the probe sites. This is only possible if the implanted region lost its elastic property. Inelastic behavior of crystalline solids is primarily caused by the presence of large density of dislocation loops [RAJG98]. Of course, the TEM micrograph clearly showed the existence of such dislocation loops after implantation of phosphorous and arsenic. The difference in the covalent radii of P and Si is responsible for the lattice mismatch and hence, for the occurrence of the large density of dislocations. The large size dislocation loops in phosphorous doped silicon might have caused permanent deformation in the implanted region. Therefore, it can be concluded that the absence of observable effect on phosphorous implanted silicon by the action of external uniaxial stress is the existence of plastic deformation due to the dense network of dislocation loops. Generally, the size and the density of dislocation loops in the implanted region varies with the type impurity atoms and implantation parameters (dose and energy). Hence, similar change to the elasticity of silicon could also be expected with various degree of variations as the result of the presence of other atoms in the substrate lattice.

## Conclusions

The study of defects in semiconductors has made important contributions to the understanding of the nature of various defects. The knowledge about the nature of defects helps to devise ways and means to eliminate or minimize the undesired behavior they may cause for many applications. In this regard, the perturbed angular correlation method has played a significant role in the understanding of point defects in metals and semiconductors. In the present investigation of indium-impurity pairs in semiconductors using PAC, new complexes are identified in silicon and germanium. The structure and thermal stability of these defect complexes are studied.

The search for an indium-impurity pairs was conducted using elements (S, Se, Te and C) in silicon and germanium. The implantation of sulfur and selenium in both elemental semiconductors did not lead to a unique quadrupole interaction frequency. The time spectra taken at successive annealing temperatures show signs of damage recovery at the beginning, but at high annealing temperatures the indium environment is disturbed again suggesting the occurrence of new chemical transformation near the indium sites. The EFGs associated with the new indium environments can not be resolved by the present PAC electronics. As a consequence, it is not possible to derive the structure of the new sites. However, at high doses of tellurium in silicon, indium forms pairs with Te characterized by a unique quadrupole interaction frequency of  $\nu_Q = 444(1)\text{MHz}$ . The orientation of the principal component of the EFG of the complex lies along the  $\langle 100 \rangle$  crystal axis. This orientation of the EFG suggests that tellurium does not possess a regular substitutional lattice location. This assumption is indeed in agreement with results of ion channelling experiments at high dose Te implantations in silicon. The assignment of tellurium at octahedral site at least justifies the observed direction of the EFG by point charge model. The measurements of the quadrupole interaction frequency of the In-Te pair at different sample temperatures showed a strong dependence on temperature. The change of the QIF with temperature is well described by the model that assumes different charge states of the complex during the time of the measurements. The empirical relation  $\sim T^{3/2}$ , which is commonly used in metals, is inadequate to describe the measured data.

The high dose carbon implantations in germanium brought about the formation of carbon-indium pairs in the host crystal. For the first time, in the current PAC experiment, isoelectronic carbon is detected at two distinct lattice locations at different annealing temperatures. The complexes are characterized by the associated unique quadrupole interaction frequencies of  $\nu_Q = 207(1)\text{MHz}$  and  $\nu_Q = 500(1)\text{MHz}$  respectively. A  $\langle 111 \rangle$  orientation of the corresponding EFGs was found, which is typical for substitutional and tetrahedral interstitial sites of defects near a substi-

tutional probe atoms in a diamond lattice structure. The low solubility of carbon in germanium has hampered many efforts to grow crystalline germanium-carbide in the past. Recently, it was possible to obtain microcrystalline germanium-carbide by ECR method [HARR00]. According to the results of the present experiment, carbon occupies substitutional lattice site in the range of annealing temperatures from 450°C to 600°C. However, it occupies an interstitial site above 650°C. The PAC time spectra taken above 450°C showed on average 50% of the indium atoms take sites that can not be resolved by the current PAC apparatus. This sites may be associated with different carbon clusters (precipitates) which produce very high EFGs difficult to be resolved. Therefore, this result suggest that the majority of implanted carbons occupy non regular lattice sites. But, there are significant amount of isolated substitutional carbon in germanium below 650°C.

Further, new results have been obtained from the experiments on indium-impurity pairs in silicon under the influence of uniaxial stress. This part of the experiment was intended to vary the interaction frequencies of the different complexes by the action of external stress. By this method, it is expected to cause lattice relaxation at the probe sites whereby new information can be extracted about the extent of deformation of the complexes by external force. In this regard, it was possible to observe the various response of probe atoms situated at different lattice sites in silicon. The absence of detectable response at an indium-donor pairs under the action of uniaxial stress is possibly due to the existence of high strain field around the complex, which prevents lattice relaxation at the site of the probe atoms. Besides, the extent of deformation that can be achieved by applying uniaxial stress to the samples is limited to  $\Delta L/L \sim 10^{-3}$ , which corresponds to about 0.1% change of the lattice constant in one major crystal axis. This value is one order of magnitude less than any of the lattice relaxation derived from the theoretical calculations of the EFGs of the complexes containing indium-single donor pairs in silicon [SETT99]. On the other hand, measurable effects have been detected from donor free substitutional sites of indium except in the phosphorous doped sample. The resulting tension induced frequencies approximately vary linear with the value of the applied stress (see Figure 5.15). However, it depends on the size of donor atoms which may play here an important role in the change of elastic properties of silicon. Due to the limitation of the PAC method to only microscopic scale, it is difficult to derive quantitative description of the bulk properties from these measurements. For example, the inelastic response of the complex containing indium-donor pairs and the different mechanical property of phosphorous implanted silicon. However, based on the studies of the mechanical properties of solids dense dislocation loops are likely to be responsible for the inelastic behavior of the phosphorous doped sample. In view of the current results, it seems promising to extend these studies to all impurities, such as acceptors, in order to improve our understanding of the influence of dopants and impurities on the mechanical properties of semiconductors.

# Appendix A

## In-Te pair in silicon

### A.1 Dissociation energy for an irreversible process

Consider a complex **XY** containing **X** and **Y** impurities in the host lattice. In order to dissociate the impurities each one of them has to overcome a potential barrier that keeps them together. Sufficient energy can be obtained from thermal treatment of the samples. For the process that is not reversible the rate of dissociation can be approximated using first order kinetics :

$$\begin{aligned} \mathbf{XY} &\rightarrow \mathbf{X} + \mathbf{Y} \\ \frac{dN}{dt} &= -CN \end{aligned} \tag{A.1}$$

where  $C = \nu \exp(\frac{E_d}{kT})$ ,  $E_d$  is the activation energy of dissociation and  $\nu$  is the dissociation attempt frequency whose value is equal to the phonon frequency  $\nu = 10^{13} \text{ s}^{-1}$  [SKUD92b, PEAR86].

$$\int_{N_0}^N \frac{dN}{N} = - \int_0^t \nu \exp(\frac{E_d}{kT}) dt \tag{A.2}$$

Integrating equation (A.1) from the initial population of the complex  $N_0$  to the population  $N$  after annealing the sample at temperature  $T$  for time  $t$ . The dissociation energy of the complex would be :

$$E_d = kT \ln \left[ \frac{1}{t\nu} \ln \left( \frac{N_0}{N} \right) \right] \tag{A.3}$$

In the case of In-Te pair in silicon the dissociation is irreversible as shown in figure (A.1). where the complex never trapped again at 700°C annealing temperature for 40min after dissociation at 900°C. Therefore, for such irreversible process it is possible to apply the relation (A.3) to estimate dissociation energy of the complex.

Using the maximum population of the In-Te pair and its population at 800°C, the resulting value of dissociation energy of the complex according equation (A.3) is 3.45 eV. Which is comparable to the activation energy of diffusion of Te in silicon 3.06 eV at 800°C [LABO98]. The expected difference is a consequence of more energy requirement of tellurium to break up from In-Te complex in silicon, which has strong ionic binding energy of about 1 eV with indium alone, than diffusing in intrinsic silicon.

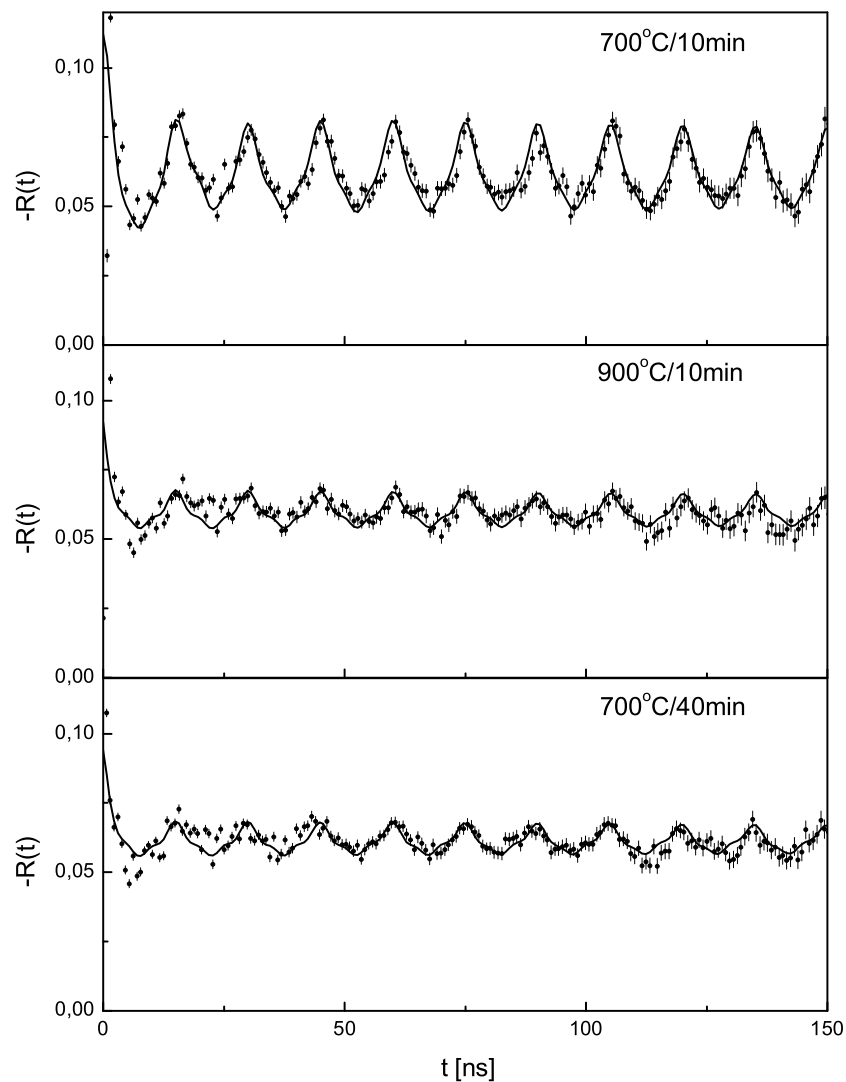


**Figure A.1:** Reversibility study of the In-Te pair in silicon. The figure showed the complex can not be re-trapped after dissociation at 900°C annealing temperature.

## A.2 Fourier transform of the interaction frequency of In-Te pair

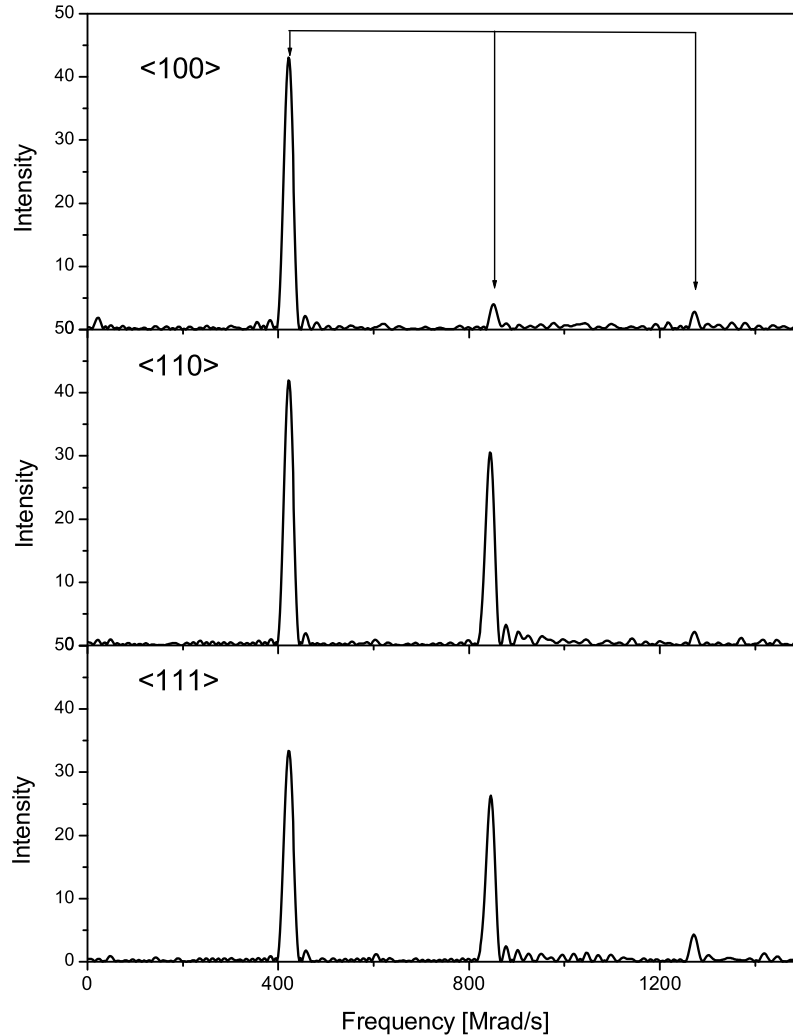


**Figure A.2:** Fourier transform of the PAC time spectra from In-Te pair in Si, which are taken at 3-different major crystal axes as indicated in the figure. This result showed the EFG characterizing the complex lie along  $\langle 100 \rangle$  axis.

In order to identify the direction of the main component of the EFG of the In-Te pair in silicon, PAC time spectra were taken by pointing the major crystal axes towards the detectors as indicated in the panels. The Fourier transform of the time spectra show the principal transition frequency  $\omega_1$  remain dominant in all cases. When the detectors point toward  $\langle 100 \rangle$  crystal axis  $\omega_2$  and  $\omega_3$  disappear indicating that

the EFG is also lie along the same axis.

### A.3 Uniaxial stress on In-Te pair in silicon.

Figure A.3 is part of the time spectra taken under the influence of uniaxial stress in silicon.

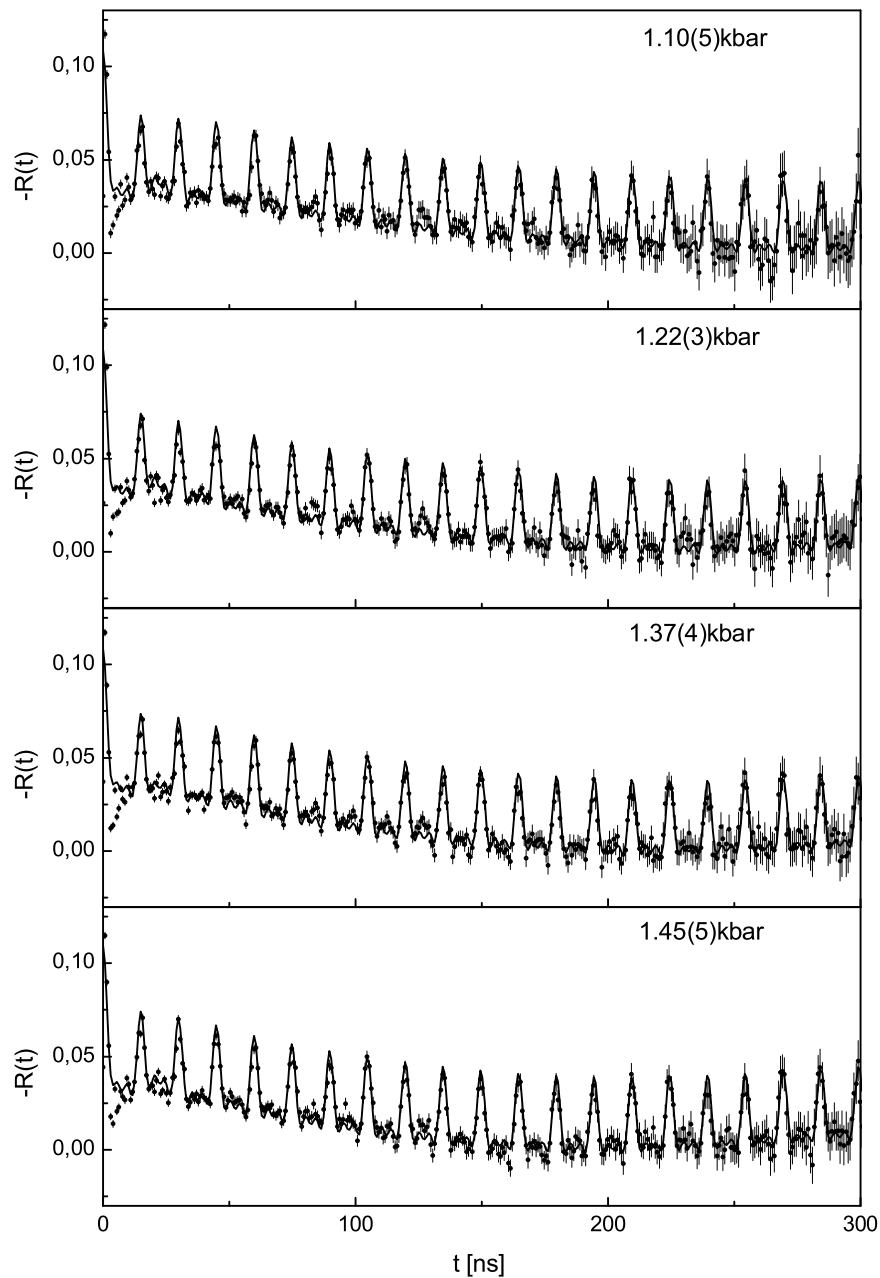


**Figure A.3:** In-Te pair in silicon under the influence of uniaxial compressional stress along  $\langle 110 \rangle$  crystal axis.



# Appendix B

## In-Sb pair in silicon.

### B.1 Uniaxial stress on In-Sb pair at low temperature in silicon.

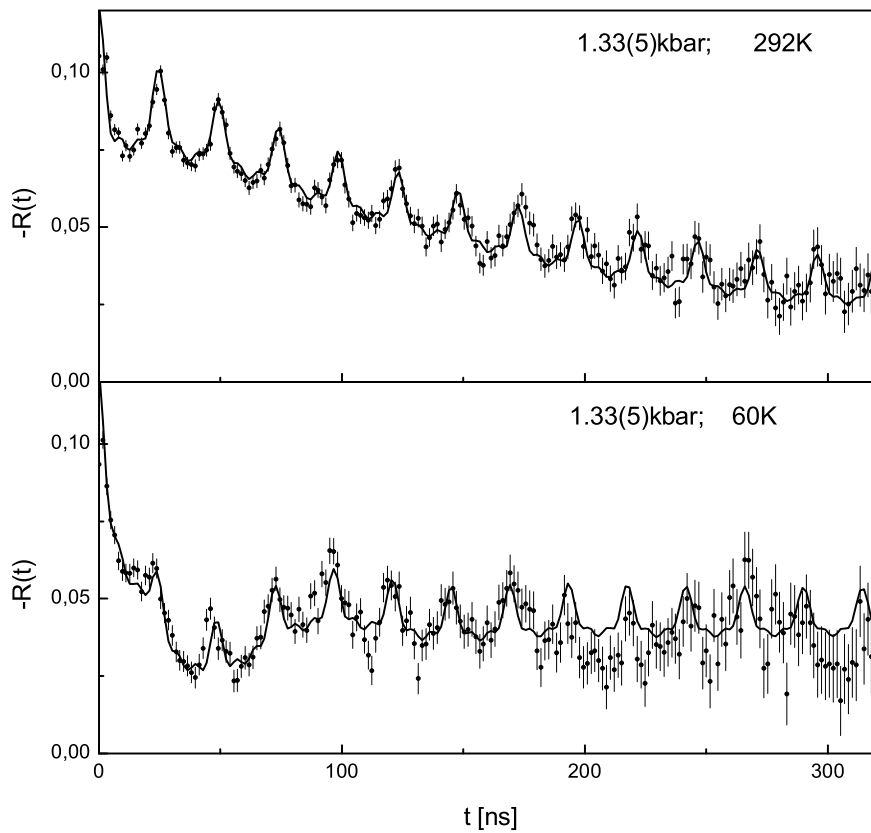


**Figure B.1:** *In-Sb pair in silicon under the influence of uniaxial compressional stress along  $\langle 110 \rangle$  crystal axis, measured at different temperature.*

Panel 1 of the following figure shows the influence of uniaxial stress at room temperature. In the second panel the spectrum was obtained by reducing the temperature

to 60K. At room temperature tension induced frequency of 8.5(1)MHz was measured at the indicated value of stress panel 1. When the sample is cooled near 60K keeping the stress constant the frequency rises to 70(1)MHz.

## B.2 Uniaxial stress on In-Sb pair in silicon.

Part of the measurements of the In-Sb pair in silicon under uniaxial stress.

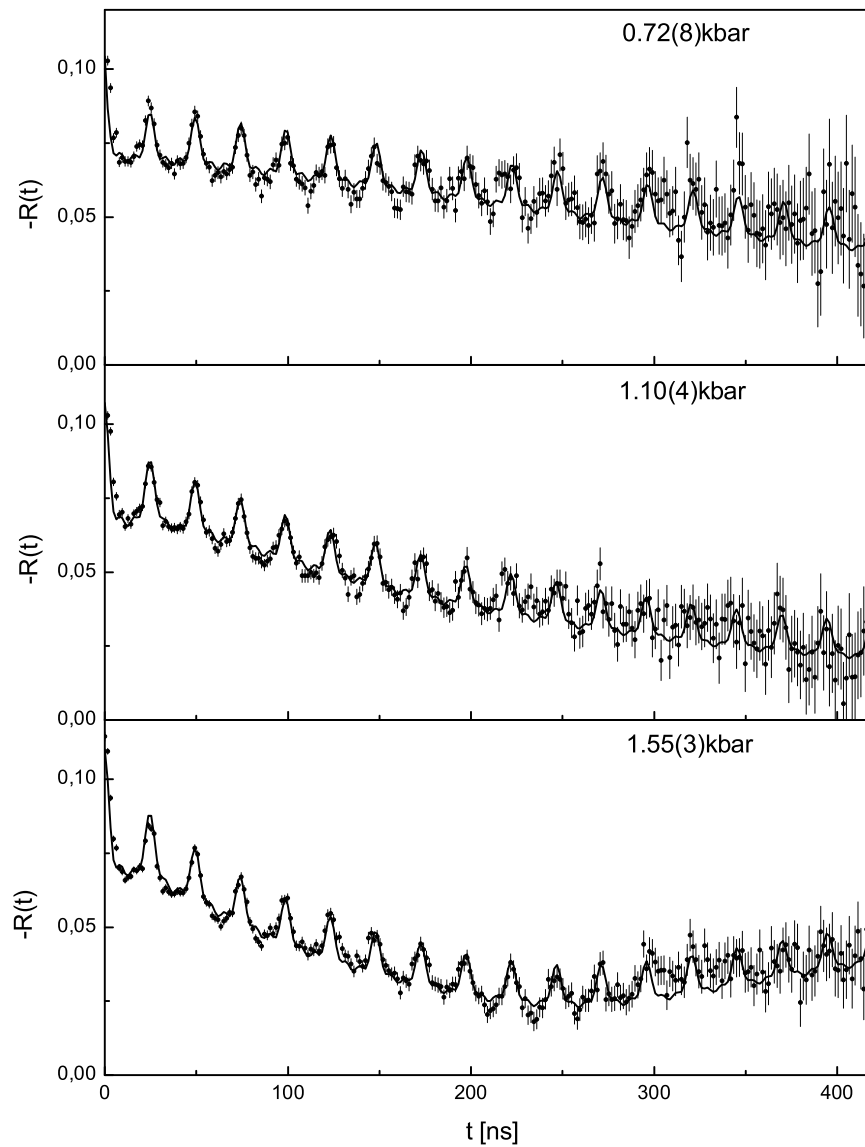


**Figure B.2:** In-Te pair in silicon under the influence of uniaxial compressional stress along  $\langle 110 \rangle$  crystal axis.

# Appendix C

## $s_n^{eff}$ -Coefficients

### C.1 polycrystalline source

In the case of axially symmetric ( $\eta=0$ ) interaction of the polycrystalline source, where atoms are randomly oriented in space, averaging over all possible field directions results in cross-term ( $k_1 \neq k_2$ ) to vanish and hence the perturbation function is formed by the attenuation factor  $G_{kk}(t)$  as :

$$G_{kk}(t) = \sum_n s_{kn} \cos(n\omega_1 t) \quad (C.1)$$

and

$$s_{kn} = \sum_{m,m'} \begin{pmatrix} I & I & k \\ m' & -m & -m' + m \end{pmatrix} \quad (C.2)$$

where n is according to equation 2.58 stated in chapter 2, which can be determined by the combination of allowed m-levels of the intermediate state (m, m'). For probe atoms spin  $I = 5/2$  of the polycrystalline source, the amplitudes are (for  $k = 2$ ) [BEZA98] :

$$s_{20} = 0.2 \quad s_{21} = 0.3714 \quad s_{22} = 0.2857 \quad s_{23} = 0.1429 \quad (C.3)$$

For non-axially symmetric electric field gradient the amplitudes of  $s_{kn}$  depends on the asymmetric parameter  $\eta$ . For spin  $I = 5/2$  of the polycrystalline source the  $s_{2n}$  are approximated [PUTZ82] by polynomial functions of  $\eta$  as :

$$\begin{aligned} s_{20} &= 0.20018 - 0.00642\eta + 0.3363\eta^2 - 0.42682\eta^3 + 0.15533\eta^4 \\ s_{21} &= 0.37294 - 0.03492\eta - 0.15689\eta^2 + 0.11476\eta^3 \\ s_{22} &= 0.28595 - 0.00472\eta - 0.00837\eta^2 + 0.02186\eta^3 \\ s_{23} &= 0.14318 - 0.00167\eta + 0.05591\eta^2 - 0.06813\eta^3 + 0.02376\eta^4 \end{aligned} \quad (C.4)$$

## C.2 $s_n^{eff}$ -Coefficients for single crystal source.

The correlation function for single crystalline source is given by the equation (2.66) as :

$$W(\vec{k}_1, \vec{k}_2, t) = \sum_{k_1 k_2, N_1 N_2} A_{k_1}(\gamma_1) \cdot A_{k_2}(\gamma_2) G_{k_1, k_2}^{N_1, N_2}(t) \cdot [(2k_1 + 1) \cdot (2k_2 + 1)]^{-1/2} \cdot Y_{k_1}^{N_1*}(\theta_1, \varphi_1) Y_{k_2}^{N_2}(\theta_2, \varphi_2) \quad (C.5)$$

For spin I = 5/2 equation (C.5) can be written in a more instructive form as :

$$W(\vec{k}_1, \vec{k}_2, t) = 1 + A_{22} \sum_{n=0}^3 s_n^{eff}(\theta_1, \varphi_1, \theta_2, \varphi_2, \theta) \cos(\omega_n(\eta) \cdot t) \quad (C.6)$$

the following  $s_n^{eff}$  coefficients are derived by U. Pütz [PUTZ82] using spherical harmonic functions ( $Y(\theta, \varphi)$ ) and ratios of the different components of anisotropy coefficients. The terms containing higher order of anisotropy coefficients ( $A_{4k}/A_{22}$ ) are neglected here i.e.  $A_{42} = A_{44} = 0$  :

$$s_0^{eff} = \frac{1}{4} \cdot (3\cos^2\theta_1 - 1) \cdot (3\cos^2\theta_2 - 1) \quad (C.7)$$

$$s_1^{eff} = \frac{6}{7} \cdot \left( \sin\theta_1 \cdot \cos\theta_1 \cdot \sin\theta_2 \cdot \cos\theta_2 \cdot \cos(\varphi_2 - \varphi_1) \right) + \frac{27}{56} \cdot \left( \sin^2\theta_1 \cdot \sin^2\theta_2 \cdot \cos 2(\varphi_2 - \varphi_1) \right) + \frac{A_{24}}{A_{22}} \cdot \left( \frac{5 \cdot \sqrt{3}}{14} \sin\theta_1 \cdot \cos\theta_1 \cdot \sin\theta_2 \cdot \cos\theta_2 \cdot (3 - 7\cos^2\theta_2) \cdot \cos(\varphi_2 - \varphi_1) - \frac{A_{24}}{A_{22}} \left( \frac{35 \cdot \sqrt{3}}{14 \cdot 8} \cdot \sin^2\theta_1 \cdot \sin^2\theta_2 \cdot (7\cos^2\theta_2 - 1) \cdot \cos 2(\varphi_2 - \varphi_1) \right) \right) \quad (C.8)$$

$$s_2^{eff} = \frac{15}{7} \cdot \left( \sin\theta_1 \cdot \cos\theta_1 \cdot \sin\theta_2 \cdot \cos\theta_2 \cdot \cos(\varphi_2 - \varphi_1) \right) + \frac{A_{24}}{A_{22}} \cdot \left( \frac{5 \cdot \sqrt{3}}{14} \sin\theta_1 \cdot \cos\theta_1 \cdot \sin\theta_2 \cdot \cos\theta_2 \cdot (3 - 7\cos^2\theta_2) \cdot \cos(\varphi_2 - \varphi_1) \right) \quad (C.9)$$

$$s_3^{eff} = \frac{15}{56} \cdot \left( \sin^2\theta_1 \cdot \sin^2\theta_2 \cdot \cos 2(\varphi_2 - \varphi_1) \right) + \frac{A_{24}}{A_{22}} \cdot \left( \frac{35 \cdot \sqrt{3}}{112} \sin^2\theta_1 \cdot \sin^2\theta_2 \cdot (7\cos^2\theta_2 - 1) \cdot \cos 2(\varphi_2 - \varphi_1) \right) \quad (C.10)$$

The angles  $(\theta_1, \varphi_1)$  and  $(\theta_2, \varphi_2)$  are taken in the principal axis system of the EFG (Figure 2.4).

# Appendix D

## Inhomogeneous lattice structure

The existence of inhomogeneous lattice structure could cause large frequency damping in PAC measurements. For instance, probe atoms may occupy lattice site surrounded by far sited defects (site 2 of Figure D.1) whose presence in the vicinity of the probe slightly vary perfect lattice ordering. It is also possible that probes

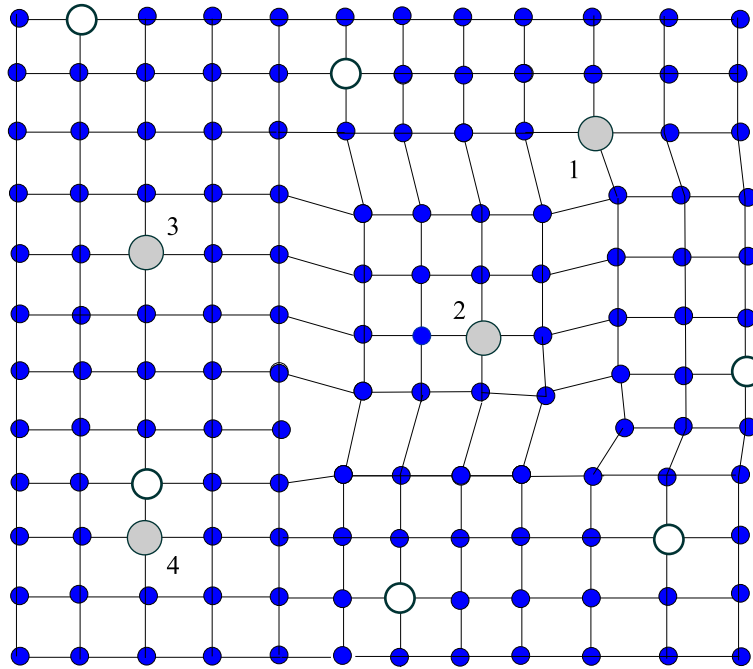


**Figure D.1:** *Imperfect lattice structure caused by ion implantation. Showing different possible environment of the probe atoms, which are numbered 1-4.*

take a site at the edge of dislocations (site 1 of Figure D.1). The occurrence of such kind of environments can prevent identical response of the same complexes to the external applied stress, which in turn leads to large width of frequency distribution around the mean value or large frequency damping.

# List of Tables

1.1	Physical constants of Ge and Si. . . . .	8
3.1	Results of the Monte-Carlo simulation calculation of the absorption coefficient for varies $\gamma$ -energies for different source-detector distance [MARX95]. . . . .	40
3.2	Geometrically corrected anisotropy coefficient of $^{111}\text{In}/^{111}\text{Cd}$ $\gamma - \gamma$ cascade . . . . .	40
3.3	Measured anisotropy coefficient of $^{111}\text{In}/^{111}\text{Cd}$ $\gamma - \gamma$ cascade . . . . .	41
3.4	Ion implantation data . . . . .	44
3.5	Fit results of indium implanted silicon and germanium samples. . . . .	48
4.1	Fit results of In-P pairs in silicon . . . . .	52
4.2	Fit results of In-As pairs in silicon . . . . .	54
4.3	Binding energy of the indium donor pair in Si [WICH89]. . . . .	57
4.4	Fit results for In-Te pairs in silicon . . . . .	60
4.5	Fit results of In-Te pairs in silicon from as implanted to 200°C annealing temperature. . . . .	63
4.6	Fit results for In-C pairs in germanium . . . . .	76
5.1	Elastic modulus of silicon and germanium at room temperature. . . . .	85
5.2	Fit results of In-Sb pair under uniaxial tensile stress along $\langle 110 \rangle$ in silicon . . . . .	90
5.3	Fit results of In-As pair under uniaxial tensile stress along the $\langle 110 \rangle$ crystal axis in silicon. . . . .	93
5.4	Fit results of In-Te pair under uniaxial compressional stress along $\langle 110 \rangle$ in silicon . . . . .	95
5.5	Fit results of In-P pair under uniaxial tensile stress along $\langle 110 \rangle$ in silicon . . . . .	96

# List of Figures

1.1	Schematic diagram of Czochralski (CZ) technique. . . . .	7
1.2	A unit cell of the diamond lattice structure. . . . .	8
1.3	The electrical conductivity of Ge and Si versus temperature in the intrinsic region [DARG94]. . . . .	9
1.4	The resistivity of Si as a function of impurity concentration [SZE81].	10
2.1	The splitting of the intermediate energy level for the spin $I=5/2$ and $\eta=0$ . . . . .	15
2.2	The splitting of the intermediate energy levels of spin $I = 5/2$ and associated transition frequencies as a function of the asymmetry parameter ( $\eta$ ) according to eq. 2.25 and 2.27 . . . . .	16
2.3	(a) Decay scheme of a $\gamma - \gamma$ transition. (b) Schematic diagram of spatial distribution of radiation from ensemble of nuclei which have emitted $\gamma_1$ into detector 1 and its evolution with time in the presence of an extranuclear field. . . . .	19
2.4	Emission direction of the gamma-rays in the laboratory system. . .	20
2.5	The figure shows a frequency pattern that varies with different values of the asymmetry parameter. . . . .	26
2.6	Various patterns of an interaction frequency whose EFG lies along the $\langle 100 \rangle$ crystal axis in a diamond lattice. The detectors are pointed alternatively toward major axes as indicated in the panel. .	28
3.1	Schematic diagram of the PAC set up. . . . .	30
3.2	The partial decay scheme of $^{111}\text{In}$ . . . . .	31
3.3	Energy spectrum of $^{111}\text{In}$ measured with a $\text{BaF}_2$ detector. The shaded areas indicate typical setting of the SCA windows. . . . .	32
3.4	Typical pattern of the PAC time spectra for probe atoms at different environments. . . . .	38

3.5	Two dimensional view of the cone like geometry of the BaF <sub>2</sub> detector.	40
3.6	Geometrically corrected anisotropy coefficients using Monte-Carlo simulation for $\gamma - \gamma$ transition in <sup>111</sup> In . . . . .	41
3.7	Schematic diagram of the Bonn mass separator, showing the main components of the accelerator system . . . . .	42
3.8	Schematic diagram of the Freeman type ion source [THOM78] . . .	43
3.9	Example of ion extraction from a plasma . . . . .	43
3.10	Two dimensional schematic representation of a disordered atomic arrangement caused by ion implantation(a) and recrystallization after annealing (b). . . . .	45
3.11	PAC time spectra from indium implanted silicon sample showing an increase in anisotropy by annealing the sample. The solid line is fit of the appropriate perturbation. . . . .	46
3.12	PAC time spectra from indium implanted Germanium sample . . .	47
4.1	PAC time spectra modulated by interaction frequency of In-P pair in silicon. The solid line is the theoretical fit according to equation 3.23, measurements are taken along $\langle 100 \rangle$ crystal axis. . . . .	51
4.2	The fractional population of indium at different environments. . . .	52
4.3	PAC time spectra showing the retrapping of In-P pair in silicon. . . .	53
4.4	PAC time spectra from In-As pairs in silicon showing well defined interaction frequencies associated with different indium environments in As doped silicon. The solid line is computer fit according to equation 3.23 . . . . .	55
4.5	Models representing possible substitutional indium environment in Si and Ge, where D stands for donor atoms and the white balls are host atoms [WICH89] . . . . .	56
4.6	PAC time spectra from a Te doped Si sample showing the interaction frequency after different annealing temperatures. The detectors are positioned along $\langle 100 \rangle$ crystal axis. The solid lines are theoretical fits according to equation 3.8 and equation 3.23. . . . .	59
4.7	The fractional population of the probe nuclei at different lattice sites in Te implanted silicon. . . . .	60
4.8	Orientation measurement of the In-Te pair in Si, showing the different patterns of the time spectra when the crystal axes indicated in the panels are pointed to wards detectors. . . . .	61



4.9	PAC time spectra from Te doped Si sample showing the interaction frequency right after implantation. The right panel shows Fourier transform of the as implanted time spectra. . . . .	62
4.10	Possible lattice structure of the In-Te pair in silicon. . . . .	64
4.11	PAC time spectra of In-Te pair measured at different temperatures	66
4.12	Quadrupole interaction frequency of the In-Te pair in silicon at different temperatures. The solid line is a fit according to equation (4.5) . . . . .	68
4.13	PAC time spectra taken from selenium implanted silicon. . . . .	69
4.14	PAC time spectra from a carbon doped Ge sample showing the modulation of the time spectra with a well defined frequency. Below 650°C annealing an interaction frequency of $\nu_{Q1} = 207(1)$ MHz ( $\eta = 0.16(3)$ )(site 1a) is observed. The solid line is the theoretical fit according to equation 3.23 . . . . .	72
4.15	PAC time spectra of In-C pair above 650°C annealing temperatures with an interaction frequency of $\nu_{Q2} = 500(1)$ MHz and $\eta = 0$ . The solid line is the fit according to equation 3.23 . . . . .	73
4.16	Fourier transform of the PAC time spectra taken from C doped Ge sample at different crystal axis after 600°C annealing temperature representing the interaction frequency $\nu_{Q1} = 207(1)$ MHz of site 1a .	74
4.17	Fourier transform of the PAC time spectra taken from C doped Ge sample at different crystal axis after 750°C annealing temperature representing the interaction frequency $\nu_{Q2} = 500(1)$ MHz of site 1b .	75
4.18	Possible lattice site of C in germanium after different annealing temperature(a) substitutional carbon (site 1a) (b) carbon in an interstitial lattice (site 1b), which is on either bonding or antibonding center. . . . .	76
4.19	Fraction of the probe nuclei at different environments in carbon doped germanium . . . . .	77
4.20	Results of ion channelling study of substitutional carbon in germanium [HOFF97] . . . . .	79
4.21	Results of the intensity of the line $531 \text{ cm}^{-1}$ of infrared absorption on the one hand and substitutional carbon by ion channelling on the other in germanium [HOFF97] . . . . .	80
5.1	A unit cell of the diamond lattice structure of Si and Ge. It is composed of 18 atoms. A section of the diagram with dashed lines shows cubic environment of a lattice site. . . . .	82

5.2	Rotational and reflection plane symmetry of the cubic environment.	82
5.3	Possible change of indium environment under the influence of uniaxial stress along $\langle 110 \rangle$ . (a) cubic, (b) tetragonal and (c) rhombohedral	83
5.4	Techniques of producing uniaxial stress on implanted samples. (a) a sample between two cylinder heads (b) Schematic diagram of tensile stressed sample and microscopic environment of a probe atom. . . .	84
5.5	Schematic diagram of the detector arrangement for measuring the tension induced EFG in Raghavan geometry, where the main component of the EFG ( $V_{zz}$ ) lies in a detector plane and pointing exactly between two detectors situated at $90^\circ$ . . . . .	86
5.6	Intrinsic silicon sample doped with $^{111}\text{In}$ and annealed at $900^\circ\text{C}$ for 600s. (a) Panel 2 shows well defined tension induced frequency of 20(1)MHz by the application of 1.81(4)kbar uniaxial tensile stress along $\langle 110 \rangle$ (b) The corresponding Fourier transform of the frequency. . . . .	87
5.7	In-Sb pair in silicon under the influence of uniaxial tensile stress along $\langle 110 \rangle$ . . . . .	88
5.8	Schematic diagram of the detectors arrangement for measurements under uniaxial tensile stress. The main component of tension induced EFG ( $V_{zz}$ ) lie perpendicular to the detectors plane. The right side shows the direction of the stress at probe site . . . . .	89
5.9	Interaction frequency of the In-Sb pair and tension induced frequency from site 0 in silicon for different value of applied stress. . . . .	89
5.10	In-As pair in silicon under the influence of uniaxial compressional stress along $\langle 110 \rangle$ . . . . .	91
5.11	The result of the action of uniaxial stress along $\langle 110 \rangle$ crystal axis on the different complexes of arsenic doped silicon sample. The interaction frequencies of In-As <sub>x</sub> complexes remain unchanged but tension induced frequency from donor free substitutional fraction ( $f_0$ ) increases with the value of stress. . . . .	92
5.12	In-Te pair in silicon under the influence of uniaxial compressional stress along $\langle 110 \rangle$ crystal axis. . . . .	94
5.13	Interaction frequencies of the In-Te pair in silicon under the influence of uniaxial compressional stress along $\langle 110 \rangle$ . . . . .	95
5.14	In-P pair in silicon under the influence of uniaxial tensile stress along $\langle 110 \rangle$ crystal axis. . . . .	97

<i>List of Figures</i>	120
5.15 Stress induced frequencies at site 0 by an external uniaxial stress along $\langle 110 \rangle$ crystal axis, after various donor implantations in silicon. . . . .	99
5.16 The values of damping for stress induced frequencies of site 0 in impurity doped silicon. . . . .	100
5.17 Plane view of transmission electron micrograph (TEM) of (a) phosphorous and (b) arsenic implanted silicon after annealing the samples at 900°C for 30 minutes [PRUS87] [KEVI87]. . . . .	101
5.18 The QI frequency of 16 MHz is simulated to 30% population of the probe atoms. The figure shows drastic change of the amplitude of modulation with the value of damping. . . . .	102
A.1 Reversibility study of the In-Te pair in silicon. The figure showed the complex can not be re-trapped after dissociation at 900°C annealing temperature. . . . .	107
A.2 Fourier transform of the PAC time spectra from In-Te pair in Si, which are taken at 3-different major crystal axes as indicated in the figure. This result showed the EFG characterizing the complex lie along $\langle 100 \rangle$ axis. . . . .	108
A.3 In-Te pair in silicon under the influence of uniaxial compressional stress along $\langle 110 \rangle$ crystal axis. . . . .	109
B.1 In-Te pair in silicon under the influence of uniaxial compressional stress along $\langle 110 \rangle$ crystal axis, measured at different temperature.	110
B.2 In-Te pair in silicon under the influence of uniaxial compressional stress along $\langle 110 \rangle$ crystal axis. . . . .	111
D.1 Imperfect lattice structure caused by ion implantation. Showing different possible environment of the probe atoms, which are numbered 1-4. . . . .	114

# Bibliography

- [ACHT89] N. Achtziger, S. Deubler, D. Forkel, H. Wolf, and W. Witthuhn; *Investigation of cadmium-donor pairs in silicon*; Appl. Phys. Lett. Vol. 55 No. 8 pp. 766-768 (1989)
- [ACHT93] N. Achtziger and W. Witthuhn; *Perturbed-angular-correlation spectroscopy of the fluctuating hyperfine interaction at Cd-donor pairs in silicon: An approach to electronic transitions at impurities in semiconductors*; Phys. Rev. B47, pp. 6990-7004 (1993)
- [ANTO86] E. ANTONICK; *Chemical Trends in Lattice Location of Implanted Impurities in Silicon*; Radiation Effect, Vol. 88 pp.217-222 (1986)
- [ANTO86b] E. ANTONICK; *On the Lattice Location of Implanted Impurities in Silicon*; Nuclear Instruments and Methods in Physics Research B14, pp.193-203 (1986)
- [AREN80] A. R. Arends, C. Hohenemser F. Pleiter, H. Dewaard; *Data Reduction Methodology for Perturbed Angular Correlation Experiments*; Hyperfine Interactions Vol. 8 pp.191-213 (1980)
- [DARG94] A. Dargys and J. Kundrotas; *Handbook on physical properties of Ge, Si, GaAs and InP*; pp. 59-115 (1994)
- [BARF82] H. Barfuss, G. Bhnlein, H. Hohenstein, W. Kreische, H. Niedrig and A. Reimer; *Charge Carrier Governed Temperature Dependence of the EFG for  $^{111}\text{Cd}$  in Tellurium*; Z. Physik, B-Condensed matter 45, pp. 193-195; (1982)
- [BARR92] N. P. Barradas; *NNFit Manual*; Lissabon (1992)
- [BARR93] N. P. Barradas, M. Rots, A. A. Melo, J. C. Soares; *Magnetic anisotropy and temperature dependence of the hyperfine fields of  $^{111}\text{Cd}$  in single crystalline cobalt*; Phys. Rev. B Vol. 47 pp. 8763-8768 (1993)
- [BERD97] M. A. Berding, A. Sher and M. van Shilfgaarde ; *Group-IV semiconductor compounds*; Phys. Rev. B Vol. 56 No. 7 pp. 3887 (1997)

- [BEZA98] Eva Bezakova; *Implantation Damage in Materials Studied by Hyperfine Interaction*; Ph.D. Dissertation at the Australian National University (1998)
- [BENN87] A. Benninghoven, F. G. Rüdener, H. W. Werner; *Secondary Ion Mass Spectrometry: Basic Concepts, Instrumental Aspects, Applications and Trends*; Wiley, New York (1987)
- [BERA69] R. Béraud, I. Berkes, J. Danère, G. Marest and R. Rougny *Effect of Finite Time-Resolution on Perturbed Angular Correlation Measurements*; Nucl. Inst. Meth. Vol. 69 pp. 41-44 (1969)
- [BIER80] J. P. Biersack, L. G. Haggmark; *A Monte Carlo computer program for the transport of energetic ions in amorphous targets*; Nucl. Inst. Meth. Vol. 174 no. 1-2 pp. 257-269 (1980)
- [BLAH96] P. Blaha, P. Dufek, K. Schwarz, H. Haas *Calculation of electric hyperfine interaction parameters in solids*; Hyperfine Interactions Vol. 97-98 no. 1-4 pp.3-10 (1996)
- [BLOO92] P. Blood and J. W. Orton; *The Electrical Characterization of Semiconductors: Majority Carriers and Electron States*; Academic Press, London (1992)
- [BOUR88] J. C. Bourgoin, M. Lannoo; *Point defects in semiconductors II*; Springer Verlag (1983)
- [BUTZ89] T. Butz; *Analytic perturbation functions for static interactions in perturbed angular correlations of  $\gamma$ -rays*; Hyp. Int. Vol. 52 no. 3 pp. 189-228 (1989)
- [CHRS76] J. Christiansen, P. Heubes, R. Keitel, W. Leoffler, W. Sandner and W. Witthuhn ; *Temperature Dependence of the EFG in Noncubic metals*; Z. Physik B24, pp. 177-187; (1976)
- [COLI81] Colin E. Jones, David Scafer, Walter Scott, and R. J. Hager; *Carbon-acceptor pair centers (X centers) in silicon.*; J. Appl. Phys. Vol. 52 No. 8 pp. 5148 (1981)
- [CROI98] N. Croitoru, R. Dahan, P. G. Rancoita, M. Rattaggi, G. Rossi, A. Seidman; *Study of resistivity and majority carrier concentration of silicon damaged by neutron irradiation*; Nucl. Phys. B - Proc. Suppl. Vol. 61B pp. 456-463 (1996)
- [DEAN79] J. A. Dean Edt.; *Lange's Handbook of Chemistry*; McGRAW-HILL, New York, pp 3-121 (1979)

- [EBER92] K. Eberl, S. S. Iyer, S. Zollner, J. C. Tsang and F. K. LeGoues; *Growth and strain compensation effects in the ternary  $Si_{1-x-y}Ge_xC_y$  alloy system*; Appl. Phys. Lett. Vol. 60 pp. 3033-3035 (1992)
- [FIRE96] R. B. Firestone, V. S. Shirly; *Table of Isotopes*; eight Edition Vol. 1 (1996)
- [FRER84] H. P. Frerichs and S. Kalbitzer; *Lattice Positions of Implanted Silicon Crystals*; Radiation Effects, Vol. 83 pp. 135-143(1984)
- [FRAU65] H. Frauenfelder, R. M. Steffen; *Alpha-, Beta- and Gamma Spectroscopy*, Vol. 2, Ed., K. Siegbahn pp. 997 (1965)
- [FORK83] D. Forkel, W. Engel, M. Iwatschenko-Borho, R. Keitel and W. Witthuhn ; *Cd-Impurities in the semiconductor  $In_2Te_5$  studied by the PAC method*; Hyperfine Interactions 15/16 pp.821-26; (1983)
- [FORK92] D. Forkel N. Achtziger, A. Baurichter, M. Deicher, S. Deubler, M. Puschmann , H. Wolf and W. Witthuhn ; *Acceptor-Donor pairs in germanium* ; Nuclear Instrument and Methods in Physics Research B63; (1992)
- [GERD69] E. Gerdau, J. Wolf, H. Winkle, J. Braunsfurth; *Quadrupole interaction of  $^{181}Ta$  in Hf compounds*; Proc. Roy. Soc. A Vol. 311 No. 1504 pp. 197-200 (1969)
- [GAYD68] A. G. Gaydon; *Dissociation Energies and Spectra of Diatomic Molecules, 3<sup>d</sup> ed.*; Chapman & Hall, London, (1968)
- [HART68] J. L. Hartke; *The three-dimensional Pole-Frenkel effect*; J. Appl. Phys. Vol. 39 No. 10 pp. 4871-4873 (1968)
- [HALL82] E. E. Haller, W. L. Hansen, P. Luke, R. McMurray and B. Jarrett; *Carbon in High-Purity Germanium*; IEEE Transactions on Nuclear Science, Vol. NS-29 No. 1 pp. 745-750 (1982)
- [HARR00] J. T. Harrold, Vikram L. Dalal; *Growth and properties of microcrystalline germanium-carbide alloy grown using electron cyclotron resonance plasma processing*; Journal of Non-Crystalline Solids, Vol. 270 pp. 255 (2000)
- [HEND72] B. Henderson; *The Structures and Properties of Solids*; Defects in Crystalline Solids, Edt. Bryan R. Coles (1972)
- [HOFF97] L. Hoffmann, J. C. Bach, and B. Bech Nielsen; *Substitutional carbon in germanum*; Phys. Rev. B ; Vol. 55 No. 17 pp. 11 167 (1997)

- [HRYN83] A. Z. Hryniewicz and K. Krolas; *Formation of two-impurity complex in dilute alloys observed through perturbed angular correlation of  $\gamma$ -rays*; Phys. Rev. B Vol. 28 No. 4 pp. 1864-1869(1983)
- [KEVI87] Kevin S. JONES, S. PRUSSIN and E. R. WEBER; *The effect of implant species on defect anneal kinetics part II: arsenic and germanium implantation* ; Hyp. Int. Vol. B21 pp. 499-501 (1987)
- [LABO98] Landolt-Bornstein; *Diffusion in Semiconductors and non-metallic solid* ; Edi. D.L. Beke Vol. 33 pp. 185 (1998)
- [LANG91] M. Lang, G. Pensel, M. Gebhard, N. Achtziger, M. Uhrmacher; *Deep Level transient spectroscopy on radioactive impurities: demonstration for Si:<sup>111</sup>In*; Appl. Phys. A Vol. A53 No. 2 pp. 95-101 (1991)
- [LEEW75] T. F .Lee, R. D. Pashley, T. C. McGill and J. W. Mayer; *Investigation of tellurium-implanted silicon*; J. Appl. Phys. Vol. 46 pp. 381 (1975)
- [LORE02] K. Lorenz; *Implantationsstudien an Grupe III-Nitriden*; Dissertation Universität Bonn (2002)
- [MARX95] G. Marx; *Akzeptor-Wasserstoff-Komplexe und spannungsinduzierte elektrische Feldgradienten in Silizium und Germanium*; Dissertation Universität Bonn (1995)
- [MATT62] E. Matthias, W. Schneider and R. M. Steffen; *Nuclear Level Splitting caused by Electric Quadrupole and Magnetic Dipole Interaction*; Phys. Rev. Vol. 125 No. 1 pp. 261 (1962)
- [MAYR70] J. W. Mayer, L. Eriksson and J. A. Davies ; *Ion implantation in semiconductor* ; Academic Press, New York (1970)
- [NEWM82] N. C. Newman ; *Defects in silicon* ; Rep. Prog. Phys. Vol. 45 pp. 1163-1211 (1982)
- [OTT94] U. Ott, H. Wolf, Th. Krings, Th. Wichert, H. Hsslein, R. Sielemann, M. Deicher R.C. Newman, and W.Zulehner ; *On the pairing between Indium and Carbon Atoms in Silicon*; Material Science Forum, Vol. 143-147 pp. 1251-1256 (1994)
- [PEAR87] S. J. Pearton, J. W. Corbett and T. S. Shi; *Hydrogen in crystalline semiconductors*; Appl. Phys. A43, 153-195 (1987)
- [PEAR86] S. J. Pearton, W. C. Dautremount-smith, J. Chevallier, C. W. Tu and K. D. Cumming; *Hydrogenation of shallow-donor levels in GaAs*; J. Appl. Phys. 59(8), 2821-2827 (1986)

- [PETE90] J. W. Petersen, J. Nielsen; *Identification of bandgap states by deep level transient spectroscopy on radioactive probes: the case of Au and Pt in silicon*; Appl. Phys. Lett. Vol. 56 no. 12 pp. 1122-1124 (1990)
- [PRUS87] S. PRUSSIN and Kevin S. JONES; *The effect of implant species on defect anneal kinetics part I: silicon and phosphorous implantation*; Hyp. Int. Vol. B21 pp. 496-498 (1987)
- [PUTZ82] U. Pütz; *Gitterdefekte in Wolfram und Platin nachgewiesen mit Hilfe der TDPAC-Methode*; Dissertation Universität Bonn (1982)
- [PUTZ89] U. Pütz ; *Analytic Perturbation Functions for Static Interactions in Perturbed Angular Correlations of  $\gamma$ -Rays*; Hyperfine Interactions Vol. 52 pp. 189-228 (1989)
- [RECH80] E. Recknagel ; *Site Characterization of Implanted Atoms in Materials*; Vol. B47 Edt. A. Perez and R. Coussement (1980)
- [RAGH71] R. S. Raghavan and P. Raghavan; *A new method for differential perturbed angular correlation measurements*; Nuclear Instrument and Methods in Physics Research; 92 435-437 (1971)
- [RAJG98] K. K. Rajgopal and A. R. Srinivasa; *Mechanics of the inelastic behavior of materials Part 1.*; Journal of Plasticity, Vol. 14, No.10-11, pp. 945 (1998)
- [SCHA92] G. Schatz, A. Weidinger; *Nukleare Festkörperphysik*; (Teubner Studienbücher) Teubner Stuttgart (1992)
- [SCAC59] R. I. Scace and G. A. Slack; ; J. Chem. Phys. 30 pp. 1551 (1959)
- [SCHM80] P. C. Schmidt, K. D. Sen, T. P. Das, A. Weiss; *Effect of self-consistency and crystalline potential in the solid state on nuclear quadrupole Sternheimer antishielding factors in closed-shell ions*; Phys. Rev. B Vol. 22 no. 9 pp. 4167-4179 (1980)
- [SETT99] M. Settel, T. Korhonen, N. Papanikkolaous, R. Zeller and P. H. Dederichs; *Substitutional carbon in germanium*; Phys. Rev. Lett. pp. 4369 (1999)
- [SIEG65] Ed. K. Siegbahn; *Alpha-, beta- and gamma-ray Spectroscopy*; North-Holland Publ. Comp. Amsterdam (1965)
- [SALO64] M. Salomon, L. Boström, T. Lindqvist, M. Perez, and M. Zwanziger; *Studies of the electric quadrupole interaction with the differential angular correlation method*; Arkiv För Fysik, pp. 97 Vol. 27 (1964)



- [SKUD92] H. Skudlik, M. Deicher, R. Keller, R. Magerle, W. Pfeiffer, D. Steiner, Th. Wichert and E. Recknagel ; *Influence of electronic parameters on the electric-field gradients induced by H at the probe atom  $^{111}\text{In} / ^{111}\text{Cd}$  in Si* ; Phys. Rev. B Vol. 46 No. 4 pp. 2159-2171 (1992)
- [SKUD92b] H. Skudlik, M. Deicher, R. Keller, R. Magerle, W. Pfeiffer, P. Pross and E. Recknagel; *H passivation of shallow acceptors in Si studied by use of the perturbed  $\gamma - \gamma$  angular correlation technique*; Phys. Rev. B Vol. 46 No. 4 pp. 2172-2181 (1992)
- [SOUK76] M. Soukiassian, J. H. Albany, M. Vandevyver; *Electron irradiation of undoped n-type InAs*; International Conference on Radiation Effects in Semiconductors Inst. Phys. pp. 395-401 (1977)
- [STEF75] R. M. Steffen and K. Alder; *The Electromagnetic Interaction in Nuclear Spectroscopy* ,Ed., J.H. Hamilton pp. 505-733 (1975)
- [SWAN86] M. L. Swanson, Th. Wichert and A. F. Quennevill; *Detection of In-P and In-Sb atom pairs by perturbed angular correlation in silicon* Appl. Phys. Lett. 49(5), 265 (1986)
- [SZE81] S. M. Sze; *Physics of semiconductor devices*; John Wiley & Sons (1981)
- [THEW85] M. L. W. Thewalt E. C. Lightowers, J. I. Pankove; *Photoluminescence studies of the neutralization of acceptors in silicon by atomic hydrogen* Appl. Phys. Lett. 46(7), 689-691(1985)
- [THOM78] Ed. J. P. Thomas and A. Cachord; *Material Characterization using Ion beams*; Plenum Press, London and New York, pp. 33-63 (1978)
- [WAGN84] P. Wagner, C. Holm, E. Sirtl, R. Oeder and W. Zulehner; *Chalcogens as point defects in silicon*; Festkörperprobleme XXIV, pp. 191(1984)
- [WATK60] G. D. Watkins and J. W. Corbett; *Defects in Irradiated Silicon* ; Phys. Rev. B Vol. 121 No. 4 pp. 1001-1014 (1960)
- [WEGN85] D. Wegner; *Calculated perturbed angular correlations for  $^{111}\text{In}$  doped cubic single crystals*; Hyp. Int. Vol. 23 pp. 197 (1985)
- [WICH86] Th. Wichert, M. L. Swanson. and A. F. Quennevill; *Formation of In-As complexes in Silicon Observed by the Perturbed-Angular-Correlation Technique*; Phys. Rev. Vol. 57 No. 14, 1757-1760 (1986)
- [WICH89] Th. Wichert and M. L. Swanson; *Perturbed angular correlation studies of dopant atom interactions in silicon*; J. Appl. Phys. Vol. 66 pp. 3026 (1989)

- [WICH95] Th. Wichert; *Intrinsic and extrinsic defect in semiconductors studied by  $\gamma - \gamma$  angular correlation spectroscopy*; Appl. Phys. A61 pp. 207 (1995)
- [WILS73] R. G. Wilson and G. R. Brewer; “ *Ion Beam* ”; John Wiley Sons, New York (1973)
- [WITT92] W. Wtthuhn; *Dynamics and electronic transitions at impurity complexes in semiconductors*; Nuclear Instruments and Methods in Physics Research B63, pp.209-216 (1992)
- [YATE65] M. J. L. Yates; *Alpha-, Beta- and Gamma Spectroscopy*; Ed. K. Siegbahn pp. 1691 (1965)
- [YUTA00] Yutaka Wakayama, Gerhard Gerth, Peter Wener und Ulrich Gsele Leonid V. Sokolov; *Structural transition of Ge dots induced by sub-monolayer carbon on Ge wetting layer*; Appl. Phys. Lett. Vol. 77 No. 15 pp. 2328 (2000)
- [ZIEG85] J. F. Ziegler, J. B. Biersack, U. Littmark; *The stopping and range of ions in solids*; Pergamon Press, New York (1985)

# Acknowledgment

If it were not with the support of many people this work would not have come to the completion. I am very grateful for all in one way or another supported me during this time.

My sincere gratitude goes to the German Academic Exchange Service (DAAD) for the financial support I received for the whole duration of this work.

I would like to thank Priv. Doz. Dr. R. Vianden, my supervisor, for his many suggestions and constant support during this research. I am grateful to him not only for his hospitality but also the opportunities he provided me to attend schools and different conferences.

I thank Prof. Dr. M. Forker for willingly accept my request as Co-supervisor and show interest to this work. Besides, I thank him for many recommendation letters that he wrote me to the DAAD. I am so grateful to Prof. J. Bisplinghoff, who has kindly facilitated my contact to the Helmholtz Institut für Strahlen- und Kernphysik.

My deep gratitude also goes to all the people in the Mass-Separator facility for many implantations that made this work possible. I thank Priv. Doz. Dr. Eversheim for allowing me several implantations. I am so grateful to Siggie and Conny not only for the successful implantations but also for the friendship we had together.

Finally, I wish to thank Jörn and Monika for the introduction in the first phase of my work. I thank Ronan for solving problems related to computer and reading the first manuscript of this work. I am grateful to all members of the PAC group Katharina, Jose, Florian, Jakob, Patricia and Stefan for the wonderful friendship and happy moments we had together.

Bonn, Germany  
January 7, 2003

Genene Tessema

# Curriculum vitae

## Personal Data

---

Name: Genene Tessema Mola  
 Birth date : 05.10.1967  
 Birth place : Arsi, Ethiopia  
 Family Status : Married  
 Nationality : Ethiopia

## Schools attended

---

Sept. 1973 - July 1983 Chilalo Terara Elementary and Secondary School,  
 Assela, Ethiopia  
 Sept. 1983 - July 1985 Comprehensive High School, Assela  
 March 1985 School leaving certificate examination, Assela

## University education

---

Oct. 1985 - July 1989 **B. Sc. in Physics**  
 Department of Physics,  
 Addis Abeba University, Ethiopia  
 Oct. 1993 - July 1995 **M. Sc. in Physics**  
 Department of Physics,  
 Addis Abeba University and ISKP,  
 University of Bonn, Germany  
 April 1999 ERASMUS-SOCRATES School, Intensive program  
 on Condensed Matter Physics, Italy, Certificate  
 April 1999 - January 2003 **Ph.D. in Physics**  
 Helmholtz Institut für Strahlen-und Kernphysik,  
 University of Bonn, Germany  
 Supervisor: Priv. Doz. Dr. R. Vianden  
 Co-supervisor: Prof. Dr. M. Forker

## Employment

---

Augs. 1989 - Sept. 1993 Assistant Lecturer, Alemaya University, Ethiopia  
 Sept. 1995- 1998 Lecturer, Alemaya University, Ethiopia